

Invariant amplitudes, unpolarized cross sections, and polarization asymmetries in (anti)neutrino-nucleon elastic scattering

KAUSHIK BORAH¹, MINERBA BETANCOURT², RICHARD J. HILL^{1,2}, THOMAS JUNK², AND
OLEKSANDR TOMALAK³

¹*Department of Physics and Astronomy, University of Kentucky, Lexington, KY 40506, USA*

²*Fermilab, Batavia, IL 60510, USA*

³*Theoretical Division, Los Alamos National Laboratory, Los Alamos, NM 87545, USA*

March 8, 2024

Abstract

At leading order in weak and electromagnetic couplings, cross sections for (anti)neutrino-nucleon elastic scattering are determined by four nucleon form factors that depend on the momentum transfer Q^2 . Including radiative corrections in the Standard Model and potential new physics contributions beyond the Standard Model, eight invariant amplitudes are possible, depending on both Q^2 and the (anti)neutrino energy E_ν . We review the definition of these amplitudes and use them to compute both unpolarized and polarized observables including radiative corrections. We show that unpolarized accelerator neutrino cross-section measurements can probe new physics parameter space within the constraints inferred from precision beta decay measurements.

Contents

1	Introduction	3
2	Amplitude decomposition and unpolarized cross section	3
3	Single-spin asymmetries	5
4	Phenomenology	7
4.1	Beta decay constraints	8
4.2	Unpolarized observables	8
4.3	Polarization observables	9
5	Radiative corrections to unpolarized cross sections and single-spin asymmetries	10
6	Conclusions and Outlook	11
A	Cross section, asymmetry, and radiative corrections plots	13
A.1	Unpolarized cross sections	13
A.2	Polarization asymmetries, muon (anti)neutrino	18
A.3	Polarization asymmetries, tau (anti)neutrino	28
A.4	Radiative corrections	38
A.4.1	Radiative corrections to unpolarized cross sections	38
A.4.2	Radiative corrections to polarization asymmetries, muon (anti)neutrino	40
A.4.3	Radiative corrections to polarization asymmetries, tau (anti)neutrino	50
	References	60

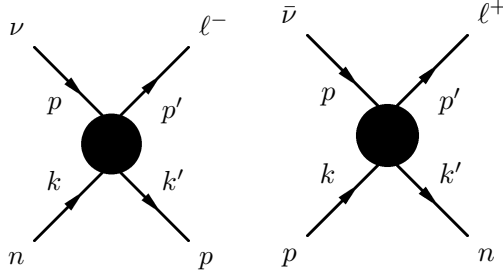


Figure 1: Kinematics of charged-current elastic scattering for neutrino (left) and antineutrino (right).

1 Introduction

Next-generation neutrino oscillation experiments DUNE [1, 2] and Hyper-K [3] aim to discover charge-parity (CP) violation in the lepton sector and conclusively establish the ordering of neutrino masses. To achieve these goals, it is essential to control muon disappearance and electron appearance signals at the percent level which requires both theoretical and experimental progress in our understanding of neutrino-nucleus interactions [4–6].

Vector form factors are known relatively well from electron scattering data [7–12], and the axial-vector form factor is the main source of uncertainty for neutrino interactions at the nucleon level. New experimental measurements [13] and lattice-QCD evaluations [14–30] of the axial-vector form factor have approached the precision of determinations from deuterium bubble-chamber data with (anti)neutrino beams [31–38] and from pion electroproduction [39–45]. Future experimental measurements can potentially yield sub-percent uncertainties [46]. Beyond unpolarized cross sections, a range of observables have been considered with polarization measurements using (anti)neutrino beams [47–82]. In a previous publication [79] by one of the authors, and in a Snowmass 2021 white paper [83], we performed a detailed study, within the Standard Model, of how to access nucleon axial-vector structure from single-spin asymmetries in elastic charged-current (anti)neutrino-nucleon scattering. In particular, asymmetry measurements could determine the nucleon pseudoscalar form factor without the conventional ansatz of partially conserved axial current (PCAC) with pion-pole dominance [39, 40, 84–98]. In order to interpret both unpolarized cross sections and polarization asymmetries with neutrino beams, and to understand the potential impact of new experimental data, we consider the general framework of invariant amplitudes for (anti)neutrino-nucleon elastic scattering. We compute both unpolarized and polarized observables including radiative corrections and compare predicted unpolarized cross sections and polarization asymmetries to constraints inferred from precision beta decay measurements.

The remainder of the paper is organized as follows. Section 2 introduces the invariant amplitude decomposition for charged-current elastic (anti)neutrino-nucleon scattering and presents the expression for the unpolarized cross section. Section 3 provides expressions for all possible single-spin asymmetries and discusses the forward and backward limits. In Section 4, we compare unpolarized cross sections and polarization asymmetries to constraints from precision beta decay measurements. We discuss the effects of radiative corrections on some observables of interest in Section 5. We present plots of cross sections, polarization asymmetries, and radiative corrections for illustrative (anti)neutrino energies in Appendix A.

2 Amplitude decomposition and unpolarized cross section

In the Standard Model, the matrix element of the charged-current elastic process with a massless charged lepton can be expressed as¹

$$\begin{aligned}
 T_{\nu n \rightarrow \ell^- p}^{m_\ell=0} &= \sqrt{2}G_F V_{ud} \bar{\ell}^- \gamma^\mu P_L \nu_\ell \bar{p} \left(\gamma_\mu (g_M + f_A \gamma_5) - (f_2 - 2f_{A3} \gamma_5) \frac{K_\mu}{M} \right) n, \\
 T_{\bar{\nu} p \rightarrow \ell^+ n}^{m_\ell=0} &= \sqrt{2}G_F V_{ud}^* \bar{\nu}_\ell \gamma^\mu P_L \ell^+ \bar{n} \left(\gamma_\mu (\bar{g}_M + \bar{f}_A \gamma_5) - (\bar{f}_2 + 2\bar{f}_{A3} \gamma_5) \frac{K_\mu}{M} \right) p,
 \end{aligned} \tag{1}$$

with the averaged nucleon momentum $K_\mu = (k_\mu + k'_\mu)/2$, and the averaged nucleon mass $M = (m_n + m_p)/2$. Following tree-level notations for the form factors, we define the electric and magnetic amplitudes g_E and g_M in

¹We use the shorthand notation $\bar{\ell}^-(\dots)\nu_\ell = \bar{u}^{(\ell)}(p')(\dots)u^{(\nu)}(p)$ and $\bar{\nu}_\ell(\dots)\ell^+ = \bar{v}^{(\nu)}(p)(\dots)v^{(\ell)}(p')$ for the usual Dirac spinors with momentum assignment in Fig. 1.

terms of the amplitudes f_1 and f_2 as

$$g_E = f_1 - \tau f_2, \quad g_M = f_1 + f_2. \quad (2)$$

Both the (anti)neutrino and the lepton are left-handed in the limit $m_\ell \rightarrow 0$ (we ignore the (anti)neutrino mass throughout, $m_{\nu_\ell} = 0$). A similar decomposition describes neutral-current (anti)neutrino-nucleon elastic scattering in terms of four amplitudes, at arbitrary m_ℓ . For nonvanishing lepton mass, the matrix element for charged currents contains four more invariant amplitudes²

$$\begin{aligned} T_{\nu_\ell n \rightarrow \ell^- p} &= T_{\nu_\ell n \rightarrow \ell^- p}^{m_\ell=0} + \sqrt{2}G_F V_{ud} \frac{m_\ell}{M} \left[\frac{f_T}{4} \bar{\ell}^- \sigma^{\mu\nu} P_L \nu_\ell \bar{p} \sigma_{\mu\nu} n - \bar{\ell}^- P_L \nu_\ell \bar{p} \left(f_3 + f_P \gamma_5 - \frac{f_R}{4} \frac{\not{P}}{M} \gamma_5 \right) n \right], \\ T_{\bar{\nu}_\ell p \rightarrow \ell^+ n} &= T_{\bar{\nu}_\ell p \rightarrow \ell^+ n}^{m_\ell=0} + \sqrt{2}G_F V_{ud}^* \frac{m_\ell}{M} \left[\frac{\bar{f}_T}{4} \bar{\nu}_\ell \sigma^{\mu\nu} P_R \ell^+ \bar{n} \sigma_{\mu\nu} p - \bar{\nu}_\ell P_R \ell^+ \bar{n} \left(\bar{f}_3 + \bar{f}_P \gamma_5 - \frac{\bar{f}_R}{4} \frac{\not{P}}{M} \gamma_5 \right) p \right], \end{aligned} \quad (3)$$

which enter all observables with a factor of the lepton mass m_ℓ . Here $P_\mu = (p_\mu + p'_\mu)/2$ denotes the averaged lepton momentum. Invariant amplitudes are functions of two kinematic variables: the crossing-symmetric variable $\nu = E_\nu/M - \tau - r_\ell^2$, with $r_\ell = m_\ell/(2M)$, $\tau = Q^2/(4M^2)$, and the squared momentum transfer $Q^2 = -(p - p')^2 = -(k - k')^2$. For the antineutrino case, the invariant amplitudes are given by $\bar{f}_i(\nu + i0, Q^2) = f_i(-\nu - i0, Q^2)^*$. At tree level, f_T and f_R vanish, and each of the remaining amplitudes are real-valued functions of the squared momentum transfer Q^2 only. In the limit of isospin invariance, the amplitudes f_{A3} and f_3 also vanish at tree level. QED radiative corrections contribute to all eight invariant amplitudes [100, 101]. The invariant amplitudes can receive corrections from new physics beyond the Standard Model. For example, the scalar interaction f_3 appears as a radiative correction in the minimally supersymmetric Standard Model (MSSM) [102, 103] or at tree level if R -parity is violated [104, 105].

Using the representation in Eqs. (1) and (3), the charged-current elastic cross section (without real radiation) in the laboratory frame is expressed in terms of invariant amplitudes as [84]³

$$\frac{d\sigma}{dQ^2}(E_\nu, Q^2) = \frac{G_F^2 |V_{ud}|^2 M^2}{2\pi E_\nu^2} \left[(\tau + r_\ell^2) A(\nu, Q^2) - \frac{\nu}{M^2} B(\nu, Q^2) + \frac{\nu^2}{M^4} \frac{C(\nu, Q^2)}{1 + \tau} \right]. \quad (4)$$

The quantities A , B , and C are given by⁴

$$\begin{aligned} A &= \tau |g_M|^2 - |g_E|^2 + (1 + \tau) |f_A|^2 - r_\ell^2 (|g_M|^2 + |f_A + 2f_P|^2 - 4(1 + \tau) (|f_P|^2 + |f_3|^2)) - 4\tau(1 + \tau) |f_{A3}|^2 \\ &\quad + \frac{r_\ell^2}{4} \left(\nu^2 + 1 + \tau - (1 + \tau + r_\ell^2)^2 \right) |f_R|^2 - r_\ell^2 (1 + 2r_\ell^2) |f_T|^2 - 2r_\ell^2 \Re \left[\left((g_E + 2g_M) - 2(1 + \tau) f_{A3} \right) f_T^* \right] \\ &\quad - \eta r_\ell^2 (1 + \tau + r_\ell^2) \Re \left[f_A f_R^* \right] - 2\eta r_\ell^4 \Re \left[f_P f_R^* \right], \end{aligned} \quad (5)$$

$$B = \Re \left[4\eta \tau f_A^* g_M - 4\eta r_\ell^2 (f_A - 2\tau f_P)^* f_{A3} + 4r_\ell^2 g_E f_3^* - 2\eta r_\ell^2 (3f_A - 2\tau (f_P - \eta f_3)) f_T^* - r_\ell^4 (f_T + 2f_{A3}) f_R^* \right], \quad (6)$$

$$C = \tau |g_M|^2 + |g_E|^2 + (1 + \tau) |f_A|^2 + 4\tau(1 + \tau) |f_{A3}|^2 + 2r_\ell^2 (1 + \tau) |f_T|^2 + \eta r_\ell^2 (1 + \tau) \Re \left[f_A f_R^* \right], \quad (7)$$

with $\eta = +1$ for neutrino scattering and $\eta = -1$ for antineutrino scattering.

In the following, we consider the limits of forward and backward charged lepton scattering, which correspond to the squared momentum transfers Q_-^2 and Q_+^2 , respectively, where

$$Q_\pm^2 = \frac{2ME_\nu^2}{M + 2E_\nu} - 4M^2 \frac{M + E_\nu}{M + 2E_\nu} r_\ell^2 \pm \frac{4M^2 E_\nu}{M + 2E_\nu} \sqrt{\left(\frac{E_\nu}{2M} - r_\ell^2 \right)^2 - r_\ell^2}. \quad (8)$$

In the forward limit, up to terms that are suppressed by the lepton mass, the unpolarized cross section can be expressed as

$$\frac{d\sigma}{dQ^2}(E_\nu, Q_-^2) = \frac{G_F^2 |V_{ud}|^2}{2\pi} (|g_E|^2 + |f_A|^2) + \mathcal{O}(m_\ell^2), \quad (9)$$

and in the backward limit, the cross section can be expressed as

$$\frac{d\sigma}{dQ^2}(E_\nu, Q_+^2) = \frac{G_F^2 |V_{ud}|^2}{\pi} \frac{|(M + E_\nu) f_A - \eta E_\nu g_M|^2}{(M + 2E_\nu)^2} + \mathcal{O}(m_\ell^2). \quad (10)$$

²The form factors from Ref. [84] contribute to our amplitudes as $f_1 = F_1^V$, $f_2 = \xi F_2^V$, $f_A = F_A$, $f_3 = F_3^V$, $f_P = F_P$, $f_{A3} = F_A^3$. At low energies, the invariant amplitudes reduce to local four-fermion couplings; conventionally normalized scalar and tensor interactions are [99] $C_S \approx -\frac{m_\ell}{M} f_3$ and $C_T \approx \frac{m_\ell}{2M} f_T$.

³We neglect the relative difference in nucleon masses, $(m_n - m_p)/(m_n + m_p)$, and electroweak power corrections suppressed by the W -boson mass M_W , i.e., the corrections of order Q^2/M_W^2 ; these effects contribute at the permille level.

⁴The sign in front of f_{A3} in B differs from Ref. [84] for antineutrino scattering, as noted in Refs. [50, 106, 107].

3 Single-spin asymmetries

Single-spin asymmetries could provide new constraints on physics beyond the Standard Model, cf. Figs. 3 and 4 below. In this Section, we provide expressions for single-spin asymmetries in charged-current elastic (anti)neutrino-nucleon scattering, in terms of the invariant amplitudes defined above, and study limits of forward and backward scattering. The single-spin asymmetry is defined as the difference between the cross section $\sigma(S)$ with a definite spin four-vector S of one initial- or final-state particle and the cross section with an opposite spin direction $\sigma(-S)$, divided by the sum of these cross sections:

$$\text{T, R, L} = \frac{d\sigma(S) - d\sigma(-S)}{d\sigma(S) + d\sigma(-S)}, \quad (11)$$

where T, R, and L denote target, recoil, and lepton asymmetries, respectively. We describe these observables in more detail below. It is convenient to express the asymmetries in a manner similar to that for the unpolarized cross section (4), in terms of new structure-dependent functions that depend on the particle whose spin we are considering:

$$\text{T, R, L} = \frac{(\tau + r_\ell^2) A^{\text{T,R,L}}(\nu, Q^2) - \nu B^{\text{T,R,L}}(\nu, Q^2) + \frac{\nu^2}{1+\tau} C^{\text{T,R,L}}(\nu, Q^2)}{(\tau + r_\ell^2) A(\nu, Q^2) - \nu B(\nu, Q^2) + \frac{\nu^2}{1+\tau} C(\nu, Q^2)}. \quad (12)$$

The target single-spin asymmetry T with a target spin four-vector $S^{\mu 5}$ is expressed in terms of the invariant amplitudes of Eqs. (1) and (3) with the following structure-dependent functions:

$$\begin{aligned} A^{\text{T}} = & \Re \left[(f_A - \eta g_E) g_M^*(k' \cdot S) - 2\eta g_M g_E^*(p' \cdot S) + 2r_\ell^2 \left(\frac{\eta g_E - f_A + 2\tau f_P}{\tau + r_\ell^2} ((k' \cdot S) + (p' \cdot S)) - f_P(k' \cdot S) \right) g_M^* \right. \\ & + 4 \frac{1+\tau}{\tau + r_\ell^2} (\tau f_{A3} - r_\ell^2 f_3) f_A^*((k' \cdot S) + (p' \cdot S)) + 2(r_\ell^2 f_3 - (1+\tau) f_{A3}) f_A^*(k' \cdot S) - 2\eta f_{A3} g_E^*(k' \cdot S) \\ & + \eta r_\ell^2 \left(\frac{2(g_E - 2\eta f_A + r_\ell^2 f_T) - r_\ell^2 f_R}{\tau + r_\ell^2} ((k' \cdot S) + (p' \cdot S)) - \left(2f_{A3} + \frac{f_R}{2} \right) (k' \cdot S) \right) f_T^* - \eta r_\ell^2 (1+\tau) f_3 f_R^*(p' \cdot S) \\ & \left. - r_\ell^2 \left(\frac{\tau - r_\ell^2}{\tau + r_\ell^2} (k' \cdot S) + \frac{2\tau(p' \cdot S)}{\tau + r_\ell^2} \right) (\eta g_M + f_A - 2f_P) f_T^* - \eta r_\ell^2 \left((1+\tau) f_3 + \frac{r_\ell^2 g_M}{\tau + r_\ell^2} \right) f_R^*((k' \cdot S) + (p' \cdot S)) \right] \\ & + \frac{\rho_\perp}{\tau + r_\ell^2} \Im \left[2r_\ell^2 (g_M f_3^* - f_A f_P^*) + \eta f_A g_E^* + 2\tau f_{A3} g_M^* + r_\ell^2 (\eta f_A + g_M - 2f_3 - 2f_{A3}) f_T^* \right] \\ & + \eta r_\ell^2 \Re \left[(4\eta f_P + r_\ell^2 f_R) f_3^* - \frac{1}{2} g_M f_R^* \right] (k' \cdot S) + \rho_\perp \eta r_\ell^2 \Im \left[\left(f_P - \frac{1}{2} \frac{f_A}{\tau + r_\ell^2} \right) f_R^* \right], \quad (13) \end{aligned}$$

$$\begin{aligned} B^{\text{T}} = & \Re \left[(\eta |f_A|^2 - g_E f_A^* + \eta \tau f_2 g_M^*) (k' \cdot S) - 2f_A g_E^*(p' \cdot S) - r_\ell^2 (f_2 f_A^* - 2f_1 f_P^*) (k' \cdot S) \right. \\ & - 2r_\ell^2 ((f_A - 2\eta f_{A3}) f_3^* + \eta f_{A3} g_M^*) (k' \cdot S) + 2\tau (\eta g_M + f_A) (f_{A3})^* (k' \cdot S) + 4\eta \tau f_{A3} g_M^*(p' \cdot S) - \frac{\eta r_\ell^4}{2} f_R f_T^*(k' \cdot S) \\ & - \eta r_\ell^2 \left[(g_M + f_2 + \eta f_A - 2f_3) f_T^*(k' \cdot S) + \frac{1}{2} g_E f_R^*((k' \cdot S) + 2(p' \cdot S)) + \left[(\tau + r_\ell^2) f_3 + \frac{r_\ell^2}{2} f_2 \right] f_R^*(k' \cdot S) \right] \\ & \left. + \eta r_\ell^2 \left(\frac{\tau}{2} f_R + f_T \right) f_T^*((k' \cdot S) + 2(p' \cdot S)) \right] - \rho_\perp \Im \left[-2\eta f_{A3} f_A^* + \frac{g_E g_M^*}{1+\tau} - \frac{r_\ell^2}{2} (f_T + 2f_{A3}) f_R^* \right], \quad (14) \end{aligned}$$

$$C^{\text{T}} = \Re \left[(g_M - g_E) f_A^* + 2\eta (g_E + \tau g_M) (f_{A3})^* + \frac{\eta r_\ell^2}{2} (1+\tau) (f_2 + f_T) f_R^* \right] (k' \cdot S), \quad (15)$$

where $\rho_\perp = M^{-3} \varepsilon^{\mu\nu\lambda\rho} p_\mu p'_\nu k_\lambda S_\rho$, $\eta = +1$ corresponds to neutrino scattering $\nu_\ell n \rightarrow \ell^- p$, and $\eta = -1$ corresponds to antineutrino scattering $\bar{\nu}_\ell p \rightarrow \ell^+ n$, with implied overline ($f_i \rightarrow \bar{f}_i$) for antineutrinos. It is worthwhile highlighting some special cases. To evaluate T_t , the asymmetry in which the target polarization is transverse to the beam direction with the spin vector in the scattering plane, we substitute $(k' \cdot S) = -(p' \cdot S) = (2M/E_\nu) \sqrt{\tau\nu^2 - (1+\tau)(\tau + r_\ell^2)^2}$ and $\rho_\perp = 0$. To evaluate T_\parallel , the asymmetry in which the target polarization is along the beam direction, we substitute $(k' \cdot S) = -2[\tau + (M/E_\nu)(\tau + r_\ell^2)]$, $(p' \cdot S) = -(k' \cdot S) - E_\nu/M$, and $\rho_\perp = 0$. To evaluate T_\perp , the asymmetry in which the target polarization is transverse to the scattering plane,

⁵We follow the same definitions, notations, and conventions as Ref. [79]. In particular, all spin four-vectors are normalized as $S^2 = -1/M^2$.

we substitute $\rho_{\perp} = 2\sqrt{\tau\nu^2 - (1+\tau)(\tau+r_{\ell}^2)^2}$, $(k' \cdot S) = 0$, and $(p' \cdot S) = 0$. For non-orthogonal spin direction, ρ_{\perp} is multiplied with $\cos\phi_{\perp}$, where ϕ_{\perp} is the angle between the spin vector and the vector $\vec{n} = \vec{p} \times \vec{p}' / |\vec{p} \times \vec{p}'|$ that is orthogonal to the scattering plane. The transverse target single-spin asymmetries T_t and T_{\perp} vanish at forward and backward angles. The longitudinal single-spin asymmetry is positive at forward scattering when the squared momentum transfer is Q_-^2 . Up to lepton-mass-suppressed terms, the asymmetry T_l reaches a maximum in absolute value at backward angles, when the squared momentum transfer is Q_+^2 . For these kinematic boundaries, the longitudinal target single-spin asymmetry is given by

$$T_l(Q_-^2) = -\frac{2\Re[g_E f_A^*]}{|g_E|^2 + |f_A|^2} + \mathcal{O}(m_{\ell}^2), \quad T_l(Q_+^2) = \eta + \mathcal{O}(m_{\ell}^2). \quad (16)$$

The structure-dependent parameters for the recoil single-spin asymmetry R, with a recoil spin four-vector S^{μ} , are expressed in terms of the invariant amplitudes of Eqs. (1) and (3) as

$$\begin{aligned} A^R &= \Re\left[(f_A - \eta g_E) g_M^* (k \cdot S) - 2\eta g_M g_E^* (p \cdot S) + 2r_{\ell}^2 \left(\frac{\eta g_E + f_A - 2\tau f_P}{\tau + r_{\ell}^2} (p \cdot S) - f_P (k \cdot S) \right) g_M^* + 2\eta f_{A3} g_E^* (k \cdot S) \right. \\ &\quad - 4\frac{1+\tau}{\tau+r_{\ell}^2} (\tau f_{A3} + r_{\ell}^2 f_3) f_A^* ((k \cdot S) + (p \cdot S)) + 2 \left((1+\tau) \frac{\tau - r_{\ell}^2}{\tau + r_{\ell}^2} f_{A3} + r_{\ell}^2 \frac{\tau + 2 - r_{\ell}^2}{\tau + r_{\ell}^2} f_3 \right) f_A^* (k \cdot S) \\ &\quad + \eta r_{\ell}^2 \left(\frac{2(g_E + 2\eta f_A + r_{\ell}^2 f_T)}{\tau + r_{\ell}^2} (p \cdot S) + \left(2f_{A3} - \frac{f_R}{2} \right) (k \cdot S) - \left((k \cdot S) + \frac{2\tau(p \cdot S)}{\tau + r_{\ell}^2} \right) (g_M - \eta f_A + 2\eta f_P) \right) f_T^* \\ &\quad \left. - r_{\ell}^2 \left[(4f_P + \eta r_{\ell}^2 f_R) f_3^* + \frac{\eta}{2} g_M f_R^* \right] (k \cdot S) + \frac{\eta r_{\ell}^4 (g_M + f_T)}{\tau + r_{\ell}^2} f_R^* (p \cdot S) - \eta r_{\ell}^2 (1+\tau) f_3 f_R^* ((k \cdot S) + 2(p \cdot S)) \right] \\ &\quad + \frac{\rho_{\perp}}{\tau + r_{\ell}^2} \Im[2r_{\ell}^2 (f_A f_P^* + g_M f_3^*) + \eta f_A g_E^* - 2\tau f_{A3} g_M^* + r_{\ell}^2 (\eta f_A + 2f_{A3} - (g_M + 2f_3)) f_T^*] \\ &\quad - \rho_{\perp} \eta r_{\ell}^2 \Im \left[\left(f_P - \frac{1}{2} \frac{f_A}{\tau + r_{\ell}^2} \right) f_R^* \right], \end{aligned} \quad (17)$$

$$\begin{aligned} B^R &= \Re\left[(\eta |f_A|^2 - g_E f_A^* + \eta \tau f_2 g_M^*) (k \cdot S) - 2f_A g_E^* (p \cdot S) + r_{\ell}^2 (f_2 f_A^* - 2f_1 f_P^*) (k \cdot S) \right. \\ &\quad - 2\eta r_{\ell}^2 ((\eta f_A + 2f_{A3}) f_3^* + f_{A3} g_M^*) (k \cdot S) - 2\tau (\eta g_M + f_A) (f_{A3})^* (k \cdot S) - 4\eta \tau f_{A3} g_M^* (p \cdot S) \\ &\quad - \eta r_{\ell}^2 \left[(g_M + f_2 - \eta f_A + 2f_3) f_T^* (k \cdot S) + \frac{1}{2} g_E f_R^* ((k \cdot S) + 2(p \cdot S)) + \left[(\tau + r_{\ell}^2) f_3 - \frac{r_{\ell}^2}{2} f_2 \right] f_R^* (k \cdot S) \right. \\ &\quad \left. - \frac{r_{\ell}^2}{2} (k \cdot S) f_R f_T^* - \left(\frac{\tau}{2} f_R - f_T \right) f_T^* ((k \cdot S) + 2(p \cdot S)) \right] - \rho_{\perp} \Im \left[2\eta f_{A3} f_A^* + \frac{g_E g_M^*}{1+\tau} + \frac{r_{\ell}^2}{2} (f_T + 2f_{A3}) f_R^* \right], \end{aligned} \quad (18)$$

$$C^R = \Re \left[(g_M - g_E) f_A^* - 2\eta (g_E + \tau g_M) (f_{A3})^* + \frac{\eta r_{\ell}^2}{2} (1+\tau) (f_2 + f_T) f_R^* \right] (k \cdot S). \quad (19)$$

To evaluate R_t , the recoil nucleon spin asymmetry with the spin vector in the scattering plane and perpendicular to the recoiling nucleon's momentum, we substitute $(k \cdot S) = 0$, $(p \cdot S) = -\sqrt{\tau\nu^2 - (1+\tau)(\tau+r_{\ell}^2)^2} / \sqrt{\tau(1+\tau)}$, and $\rho_{\perp} = 0$. To evaluate R_l , the recoil nucleon spin asymmetry with the spin vector in the scattering plane and parallel to the recoiling nucleon's momentum, we substitute $(k \cdot S) = 2\sqrt{\tau(1+\tau)}$, $(p \cdot S) = (\tau\nu - (1+\tau)(\tau+r_{\ell}^2)) / \sqrt{\tau(1+\tau)}$, and $\rho_{\perp} = 0$. To evaluate R_{\perp} , the asymmetry in which the recoil polarization is transverse to the scattering plane, we substitute $\rho_{\perp} = 2\sqrt{\tau\nu^2 - (1+\tau)(\tau+r_{\ell}^2)^2}$, $(k \cdot S) = 0$, and $(p \cdot S) = 0$. The transverse recoil single-spin asymmetries R_t and R_{\perp} vanish at forward and backward angles. The longitudinal single-spin asymmetry is positive at forward scattering when the squared momentum transfer is Q_-^2 . Up to lepton-mass-suppressed terms, the asymmetry R_l reaches a maximum in absolute value at backward angles, when the squared momentum transfer is Q_+^2 . For these kinematic boundaries, the longitudinal target single-spin asymmetry is given by

$$R_l(Q_-^2) = -\frac{2\Re[g_E f_A^*]}{|g_E|^2 + |f_A|^2} + \mathcal{O}(m_{\ell}^2), \quad R_l(Q_+^2) = -\eta + \mathcal{O}(m_{\ell}^2). \quad (20)$$

The structure-dependent factors for the lepton single-spin asymmetry L, with a recoil spin four-vector S^{μ} , are expressed in terms of the invariant amplitudes of Eqs. (1) and (3) as

$$(\tau + r_{\ell}^2) A^L = \Re[-\eta A (p \cdot r_{\ell} S) + 2(\tau + r_{\ell}^2) (f_A g_M^* - (f_A - 2\tau f_P) (f_{A3})^* + \eta g_E f_3^*) (p + 2k \cdot r_{\ell} S)$$

$$\begin{aligned}
& -2\eta r_\ell^2 (|g_M|^2 + |f_A + 2f_P|^2 - 4(1 + \tau)(|f_P|^2 + |f_3|^2) + 2g_M f_T^*) (p \cdot r_\ell S) \\
& + (\tau + r_\ell^2) \left((f_A - 2r_\ell^2 (f_P - \eta f_3)) f_T^* + \left(\frac{\tau + r_\ell^2}{2} \eta g_M - r_\ell^2 f_{A3} - \eta \frac{r_\ell^2}{2} f_T \right) f_R^* \right) (p + 2k \cdot r_\ell S) \\
& - r_\ell^2 \left(2(1 + \tau + r_\ell^2) f_A + 4r_\ell^2 f_P + \eta \frac{(\tau + r_\ell^2)^2 + \tau + 2r_\ell^2}{2} f_R \right) f_R^* (p \cdot r_\ell S) - 2\eta r_\ell^2 |f_T|^2 (p \cdot r_\ell S) \\
& + \eta r_\ell \rho_\perp \Im \left[2g_E f_3^* - 2f_{A3} f_A^* - 4\tau f_P (f_{A3})^* + (f_A + 2r_\ell^2 (f_P - \eta f_3)) f_T^* \right] \\
& + \eta r_\ell \rho_\perp \Im \left[\frac{\tau + r_\ell^2}{2} g_M f_R^* - \frac{r_\ell^2}{2} (f_T + 2f_{A3}) f_R^* \right], \tag{21}
\end{aligned}$$

$$\begin{aligned}
B^L &= \Re[-2f_A g_M^* (p \cdot r_\ell S) + \frac{\eta C}{1 + \tau} (p + 2k \cdot r_\ell S) + (2\eta g_E f_3^* - 2(f_A - 2\tau f_P) (f_{A3})^* - r_\ell^2 f_{A3} f_R^*) (p \cdot r_\ell S) \\
& + ((f_A + 2r_\ell^2 (f_P - \eta f_3)) (p \cdot r_\ell S) + \eta (\tau - r_\ell^2) (f_2 + 2f_{A3}) (p + 2k \cdot r_\ell S)) f_T^* - \eta \frac{r_\ell^2}{2} f_T f_R^* (p \cdot r_\ell S) \\
& + \eta \left(\frac{\tau - r_\ell^2}{2} f_A f_R^* - 4r_\ell^2 |f_T|^2 \right) (p + 2k \cdot r_\ell S) + \eta \frac{\tau - r_\ell^2}{2} g_M f_R^* (p \cdot r_\ell S) \\
& + r_\ell \rho_\perp \Im [(f_2 + 2f_{A3}) f_T^* + \frac{\eta}{2} f_A f_R^*], \tag{22}
\end{aligned}$$

$$C^L = \eta(1 + \tau) \Re[(f_2 + 2f_{A3}) f_T^* + \frac{1}{2} (\eta f_A + r_\ell^2 f_R) f_R^*] (p \cdot r_\ell S). \tag{23}$$

To evaluate L_t , the lepton spin asymmetry with the spin vector in the scattering plane and perpendicular to the lepton momentum, we substitute $(k \cdot r_\ell S) = 0$, $(p \cdot r_\ell S) = 2r\sqrt{\tau\nu^2 - (1 + \tau)(\tau + r_\ell^2)^2}/\sqrt{(\nu + r_\ell^2 - \tau)^2 - 4r_\ell^2}$, and $\rho_\perp = 0$. To evaluate L_1 , the lepton spin asymmetry with the spin vector in the scattering plane and parallel to the lepton momentum, we substitute $2(k \cdot r_\ell S) = \sqrt{(\nu + r_\ell^2 - \tau)^2 - 4r_\ell^2}$, $(p \cdot r_\ell S) = -((r_\ell^2 - \tau)\nu + (\tau + r_\ell^2)^2)/\sqrt{(\nu + r_\ell^2 - \tau)^2 - 4r_\ell^2}$, and $\rho_\perp = 0$. To evaluate L_\perp , the asymmetry in which the lepton polarization is transverse to the scattering plane, we substitute $\rho_\perp = 2\sqrt{\tau\nu^2 - (1 + \tau)(\tau + r_\ell^2)^2}$, $(k \cdot r_\ell S) = 0$, and $(p \cdot r_\ell S) = 0$. The transverse lepton single-spin asymmetries L_t and L_\perp vanish at forward and backward angles. Up to lepton-mass-suppressed terms, the longitudinal single-spin asymmetry reaches its extremum reflecting the chiral nature of the weak interaction, i.e., $L_1 = -\eta + \mathcal{O}(m_\ell^2)$.

For all asymmetries (target, recoil, and lepton), only imaginary parts of the structure amplitudes contribute to the asymmetries when the spin vector is transverse to the scattering plane. These asymmetries vanish at tree level in the Standard Model.

4 Phenomenology

It is interesting to consider the potential for accelerator neutrino cross section measurements to constrain new physics beyond the Standard Model. In this Section, we consider possible short-distance interactions that could give rise to non-standard contributions to the invariant amplitudes appearing in Eqs. (1) and (3). As a benchmark for comparison, we plot observables including the region allowed by constraints on such contact interactions inferred from precision beta decays. In making this comparison, we assume the Standard Model scaling of the amplitudes with lepton mass given in Eqs. (1) and (3), i.e., assume m_ℓ -independent BSM contributions to f_i . This scaling naturally appears when the BSM contributions can be identified with modifications to the tree-level electroweak form factors associated with quark currents. For example, f_3 and f_{A3} are identified with second-class form factors [84, 108, 109]. This scaling with lepton mass can also be motivated by the assumption of ‘‘minimal flavor violation’’ [110]. It is also interesting to consider the constraints of accelerator (anti)neutrinos, with muon flavor (anti)neutrinos, independent of such assumptions, which we describe in our accompanying paper [111]. In this case, the parameter space is essentially unconstrained by beta decay since the charged muon mass is kinematically inaccessible to nuclear beta decays.

For the benchmark Standard Model prediction in numerical illustrations, we employ the vector form factors from Ref. [112] and the axial-vector form factor from Ref. [36]. For the pseudoscalar form factor, we use a standard ansatz (partially conserved axial-vector current and the assumption of pion pole dominance): $F_P(Q^2) = 2M^2 F_A(Q^2)/(m_\pi^2 + Q^2)$, with the charged pion mass m_π .

Table 1: Beta decay constraints on the real and imaginary parts of amplitudes at $Q^2 = 0$.

parameter	value	reference
$\Re f_3(0)$	0.0 ± 1.8	[113]
$\Im f_3(0)$	13 ± 54	[99]
$\Re f_T(0)$	-9.3 ± 10.3	[99]
$\Im f_T(0)$	-1.9 ± 15.4	[99]
$\Re f_{A3}(0)$	0 ± 0.075	[109]

4.1 Beta decay constraints

Neglecting the isospin-breaking corrections, the amplitudes f_T , f_3 , and f_{A3} vanish at tree level in the Standard Model. Focusing on these interactions, we consider the substitution

$$f_i(\nu, Q^2) = \frac{\Re f_i(0) + i\Im f_i(0)}{\left(1 + \frac{Q^2}{\Lambda^2}\right)^2}. \quad (24)$$

For simplicity, we have neglected (anti)neutrino energy dependence and have assumed the dipole form for Q^2 dependence [109, 114, 115] with the parameter $\Lambda \approx 1$ GeV describing a typical hadronic form-factor scale. The amplitudes g_M , f_2 , and f_A appear at tree level in the Standard Model and are unsuppressed by the lepton mass; they are thus well-constrained by (electronic) beta decay measurements and we do not consider new physics constraints on them here. The amplitude f_P is suppressed by the lepton mass but receives a large and uncertain (induced pseudoscalar) tree-level contribution, and we do not consider new physics constraints on it. The amplitudes f_T and f_3 are suppressed by the lepton mass and relatively poorly constrained by beta decay; these amplitudes will be our focus. We also consider the amplitude f_{A3} , which is unsuppressed by the lepton mass but recoil-suppressed in low-energy beta decays. Finally, we mention f_R , which is suppressed by both the lepton mass and recoil and is essentially unconstrained by beta decay.

Numerous constraints have been placed on the normalization of elastic (anti)neutrino-nucleon interactions at low energies [73, 99, 114–134]. The best low-energy constraint for the real part of the scalar amplitude f_3 comes from precise measurements of beta decay rates: $\Re f_3(0)/f_1(0) = 0.0 \pm 1.8$ [113] (see also Refs. [103, 109, 127, 131]). The imaginary part is constrained by the triple-correlation coefficient in neutron decay:⁶ $\Im f_3(0) = 13 \pm 54$ [99] (see also Ref. [105]). For the tensor amplitude f_T , we take constraints from the fit to beta decay data in Ref. [99] (see also Refs. [99, 128, 133, 135–147]): $\Re f_T(0) = -9.3 \pm 10.3$, $\Im f_T(0) = -1.9 \pm 15.4$. For the amplitude f_{A3} , which vanishes at tree level, we take the compilation of the experimental data from Ref. [109]: $|\Re f_{A3}(0)| < 0.075$. In Table 1, we collect the beta decay constraints on $\Re f_i$ and $\Im f_i$ that we use for the plots to follow.

4.2 Unpolarized observables

Figure 2 presents allowed regions for the muon-flavor charged-current elastic neutrino-neutron unpolarized cross section, for an illustrative 3 GeV neutrino energy. The cross section is evaluated with an additional amplitude of Eq. (24) and is displayed as a ratio to the benchmark Standard Model cross section. We compare the uncertainties from the vector and axial-vector form factors to the envelope of possible values of the unpolarized cross section obtained by including one additional amplitude within the errors from Table 1. The effects of $\Re f_3$ and $\Re f_{A3}$ are within the current uncertainties on the cross sections. However, the plots indicate that constraints on $\Re f_T$, $\Im f_T$, and $\Im f_3$ can be significantly improved using accelerator neutrino cross-section data [111]. We present additional plots in Figs. 6-9 of Appendix A.1 for several beam energies between 300 MeV and 3 GeV, for both neutrinos and antineutrinos.

Although precise experimental data on tau (anti)neutrino cross sections is currently lacking for GeV energies [148–151], in anticipation of future data we repeat our study of unpolarized cross sections for tau (anti)neutrinos with energies above the tau production threshold. Results are displayed in Figs. 10-13 of Appendix A.1. As expected from the charged lepton mass dependence in Eq. (3), cross sections with tau flavor are even more sensitive to the amplitudes f_3 and f_T than cross sections with muon flavor, including sensitivity to values of $\Re f_3$ that are allowed by beta decay constraints.

⁶The triple correlation is with respect to the neutron polarization, electron momentum, and electron spin, cf. Eq. (1) of Ref. [105].

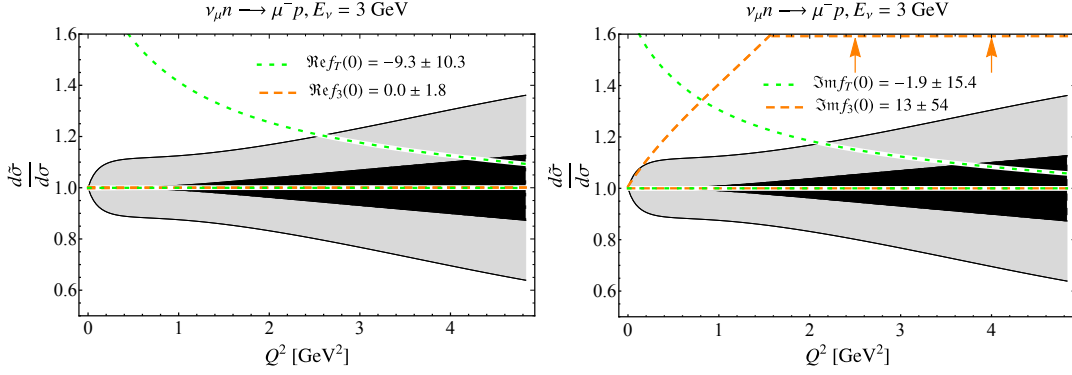


Figure 2: Ratio of unpolarized muon neutrino cross section to the tree-level result as a function of the squared momentum transfer Q^2 at fixed muon neutrino energy $E_\nu = 3$ GeV. The dark black and light gray bands correspond to vector and axial-vector uncertainty, respectively. Orange dashed and green dotted lines represent allowed regions for f_3 and f_T , respectively, as described in the text. The left and right plots show results for one extra real-valued amplitude and one extra imaginary-valued amplitude, respectively.

4.3 Polarization observables

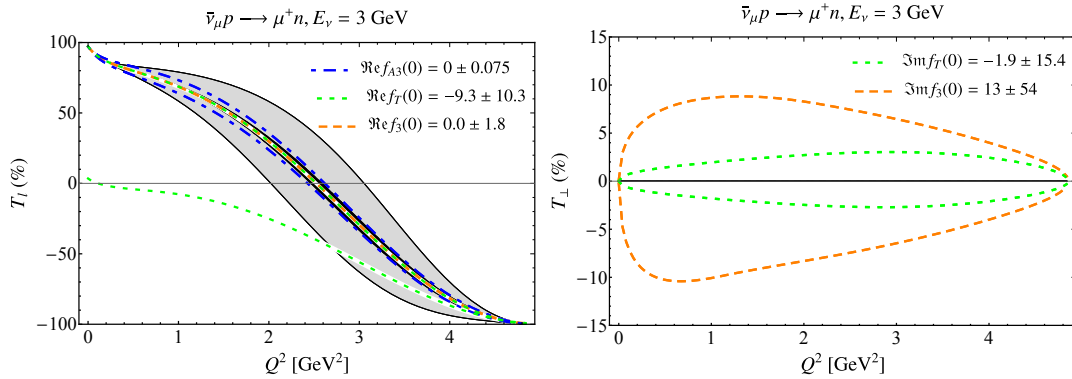


Figure 3: Polarization observables T_l with one extra real-valued amplitude (left) and T_\perp with one extra imaginary-valued amplitude (right) compared to the tree-level result at fixed muon antineutrino energies $E_\nu = 3$ GeV. The dark black and light gray bands correspond to vector and axial-vector uncertainties, respectively. Orange dashed, green dotted, and blue dashed-dotted lines represent allowed regions for f_3 , f_T , and f_{A3} , respectively, as described in the text.

We note that the contribution of the scalar amplitude f_3 and the tensor amplitude f_T to the (anti)neutrino-nucleon elastic unpolarized charged-current cross sections is always suppressed by the lepton mass, which causes relatively small effects in the scattering of electron and muon (anti)neutrinos. Consequently, it is interesting to study the contributions of these amplitudes to spin-dependent observables, where mass suppression is not necessarily present. In Fig. 3 as an illustrative example, we consider the asymmetry predicted for an illustrative 3 GeV muon antineutrino beam on a polarized proton target, including the effect of possible new physics encoded in the amplitudes in Eq. (24). Figures 14-31 of Appendix A.2 present the complete set of polarization-transfer observables $T_t, T_l, T_\perp, R_t, R_l, R_\perp, L_t, L_l, L_\perp$ for the scattering of muon (anti)neutrinos with energies between 300 MeV and 3 GeV. In each case, we present the envelope of possible asymmetries after varying the amplitudes $\Re f_3$, $\Re f_{A3}$, $\Re f_T$, $\Im f_3$, and $\Im f_T$ within the constraints of Table 1. The transverse nucleon spin asymmetries T_t and R_t both for neutrinos and antineutrinos, as well as the longitudinal asymmetries T_l and R_l , are sensitive to new parameter space for the tensor coupling $\Re f_T$, and also exhibit sensitivity to $\Re f_{A3}$ at neutrino energies above ~ 1 GeV. The asymmetry R_l both for neutrinos and antineutrinos and the target asymmetry T_l for antineutrinos provide sensitivity above current uncertainties on vector and axial-vector form factors to the amplitude $\Re f_T$ only. The target nucleon asymmetry T_l in neutrino scattering is sensitive also to the amplitude $\Re f_3$ near the muon production threshold, cf. Fig. 16. The lepton-spin asymmetries L_t and L_l are sensitive to the amplitudes $\Re f_T$ and $\Re f_3$ both

in the scattering of neutrinos and antineutrinos. The transverse polarization asymmetries T_\perp , R_\perp , L_\perp receive small Standard Model contributions but potentially large contributions from $\Im m f_T$ and $\Im m f_3$ and are thus sensitive to these quantities.

We repeat our study for tau flavor polarization asymmetries. As an illustration, Fig. 4 considers the lepton asymmetries that can be determined by measuring the polarization of the final-state tau lepton. For neutrinos with $E_\nu = 5$ GeV, the results demonstrate that asymmetries differ significantly from Standard Model predictions in large regions of parameter space that are allowed by beta decay constraints. Figures 32-44 of Appendix A.3 present results for all single-spin asymmetries over a range of (anti)neutrino beam energies between 5 GeV and 15 GeV, above the tau production threshold. For tau neutrinos, all polarization observables with a reference spin in the scattering plane are sensitive to the amplitudes $\Re e f_T$ and $\Re e f_3$. Contrary to the unpolarized cross section, the transverse spin asymmetries T_t and R_t in both neutrino and antineutrino scattering are also sensitive to $\Re e f_{A3}$. The transverse polarization asymmetries $T_\perp, R_\perp, L_\perp$, with spin direction orthogonal to the scattering plane, are sensitive to $\Im m f_T$ and $\Im m f_3$, in both neutrino and antineutrino scattering.

5 Radiative corrections to unpolarized cross sections and single-spin asymmetries

In this Section, we study the effects of radiative corrections on the unpolarized cross sections and polarization observables considered above. We take virtual contributions to the amplitudes in Eqs. (1) and (3) from the recent calculation of Refs. [100, 101]. For the muon and tau charged-current events considered in this paper, we include the radiation of one real photon with energy below $\Delta E = 10$ MeV and label this cross section as next-to-leading order (NLO).

In Fig. 5, we compare the effect of radiative corrections to the theoretical cross-section uncertainties that are obtained by propagating errors from the vector and axial-vector nucleon form factors, cf. Fig. 2. Over most of the kinematic range, the effect is larger than the current vector form factor uncertainty [112] but smaller than the current axial-vector form factor uncertainty [36]. The effects of radiative corrections are at or below the current level of experimental uncertainties but will become increasingly important with more precise data. These corrections are also critical for the determination of flavor ratios [100]. In Appendix A.4, we present results over a range of energies, for unpolarized cross sections of both neutrinos and antineutrinos, cf. Figs. 50-53. Results are displayed as a ratio of the cross sections evaluated with radiative corrections to the benchmark tree-level cross section, for the illustrative energies considered in Appendix A.1. The results reproduce those from Refs. [100, 101] for the corresponding kinematics and muon (anti)neutrino flavor. At very low squared momentum transfers, radiative corrections for muon (anti)neutrino flavor typically exceed the tree-level cross-section uncertainty, determined mainly by the axial-vector charge according to Figs. 5, 50, and 51. The corrections are positive at hundreds of MeV incoming (anti)neutrino energies and become negative for energies above 500 MeV. For tau (anti)neutrino scattering, cf. Figs. 52 and 53, the radiative corrections are well below uncertainties from the axial-vector form factor and reach vector form-factor uncertainties only at lowest squared momentum transfers.

For the first time, we investigate the effects of radiative corrections on the polarization asymmetries in neutrino scattering $T_t, T_l, R_t, R_l, L_t, L_l$ for muon and tau flavors. We present these observables in Figs. 58-89 of Appendix A.4. Radiative corrections to these asymmetries are below the uncertainties from the axial-vector form factor but have the same order of magnitude as vector form-factor errors. Besides the motivated model for the real part of amplitudes in

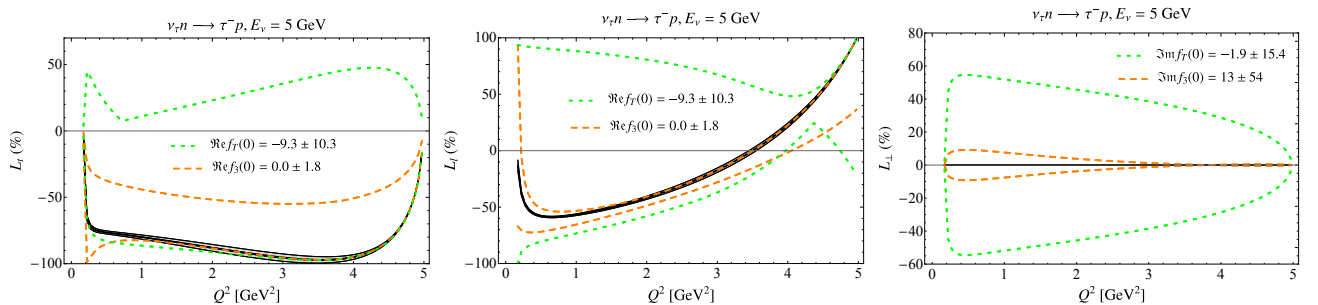


Figure 4: Polarization observables L_t , L_l with one extra real-valued amplitude, and L_\perp with one extra imaginary-valued amplitude, compared to the tree-level result at fixed tau neutrino energy $E_\nu = 5$ GeV.

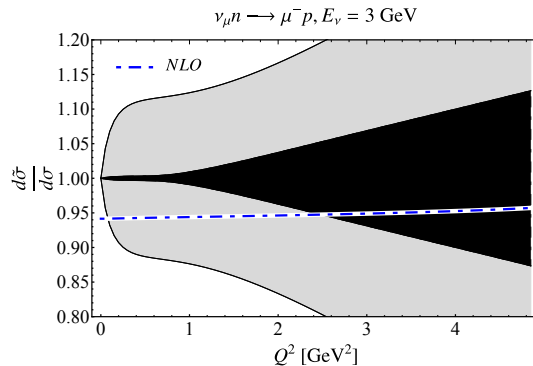


Figure 5: Radiative corrections to unpolarized cross section in Fig. 2. The blue dashed-dotted line represents the radiatively-corrected result.

Refs. [100, 101], we consider also imaginary parts of all invariant amplitudes in the same model as an estimate of the order-of-magnitude for possible contributions from imaginary parts. The asymmetries with a spin vector transverse to the scattering plane vanish at tree level and are generated by the imaginary parts of invariant amplitudes. Both for muon and tau flavor, the transverse spin asymmetries T_{\perp}, R_{\perp} are typically at permille level. The asymmetry L_{\perp} is below permille and can reach $\sim 0.1\%$ at some kinematics.

6 Conclusions and Outlook

In this paper, we present the general decomposition of (anti)neutrino-nucleon charged-current elastic scattering amplitudes. We provide expressions for the unpolarized cross section and single-spin asymmetries in terms of these amplitudes and investigate both the forward and the backward limits for these observables. We provide numerical results for all observables for relevant fixed (anti)neutrino energies as a function of the squared momentum transfer considering the uncertainty of tree-level nucleon form factors and also accounting for radiative corrections. QED contributions to muon (anti)neutrino-nucleon charged-current elastic scattering cross sections are of the order of the theoretical uncertainty, while the radiative corrections to the scattering of tau (anti)neutrinos are much smaller than the theoretical error from current knowledge of the nucleon form factors. The radiative corrections to the single-spin asymmetries largely cancel between the numerator and denominator resulting in negligible effects within the uncertainties of tree-level predictions.

Assuming the dipole form for the Q^2 dependence and ν independence for possible new physics contributions to the invariant amplitudes, and Standard Model scaling with the lepton mass, we examine the parameter space allowed by beta decay constraints on unpolarized cross sections and polarization transfer observables. Surprisingly, we find that the available constraints on both the real and the imaginary parts of the tensor interaction coefficient, as well as constraints on the imaginary part of the scalar coefficient, can be significantly improved with current data on the unpolarized antineutrino-hydrogen and neutrino-deuterium scattering cross sections. We present an analysis of the recent antineutrino-hydrogen measurement by the MINERvA Collaboration in an accompanying publication [111]. Relatively imprecise first measurements of single-spin asymmetries with (anti)neutrino beams would be sensitive to new parameter space for both the real and the imaginary parts of the scalar and tensor couplings.

Acknowledgments

We thank Susan Gardner, Kevin McFarland, and Ryan Plestid for useful discussions. This work is supported by the US Department of Energy through the Los Alamos National Laboratory and by LANL's Laboratory Directed Research and Development (LDRD/PRD) program under projects 20210968PRD4, 20210190ER, and 20240127ER. Los Alamos National Laboratory is operated by Triad National Security, LLC, for the National Nuclear Security Administration of U.S. Department of Energy (Contract No. 89233218CNA000001). This work was supported by the U.S. Department of Energy, Office of Science, Office of High Energy Physics, under Award DE-SC0019095. R.J.H. acknowledges support from a Fermilab Intensity Frontier Fellowship. K.B. acknowledges support from the Visiting Scholars Award Program of the Universities Research Association and the Fermilab Neutrino Physics

Center Fellowship Program. Fermilab is operated by Fermi Research Alliance, LLC under Contract No. DE-AC02-07CH11359 with the United States Department of Energy. FeynCalc [152, 153], LoopTools [154], and Mathematica [155] were extremely useful in this work.

A Cross section, asymmetry, and radiative corrections plots

In this Appendix, we collect illustrative plots showing Standard Model uncertainties and constraints on new physics extrapolated from beta decay measurements. Section A.1 considers unpolarized cross sections for muon flavor and tau flavor (anti)neutrinos. Sections A.2 and A.3 consider polarization asymmetries for muon and tau flavor (anti)neutrinos, respectively. Section A.4 shows the impact of radiative corrections on each of the above observables.

A.1 Unpolarized cross sections

In this Section, we consider the unpolarized cross section with one extra real- or imaginary-valued amplitude, $f_i(\nu, Q^2) = [\Re f_i(0) + i\Im f_i(0)] / \left(1 + \frac{Q^2}{\Lambda^2}\right)^2$, for illustrative muon (tau) neutrino and antineutrino energies $E_\nu = 300$ MeV, 600 MeV, 1 GeV, and 3 GeV ($E_\nu = 5$ GeV, 7 GeV, 10 GeV, and 15 GeV), and $\Lambda = 1$ GeV. We vary the amplitude normalizations within the ranges from Table 1, and compare to the uncertainty from vector and axial-vector form factors from Sec. 4. The effect from the extra amplitude $\Re f_{A3}(0)$ from Table 1 cannot be distinguished from zero on plots with the unpolarized cross section.

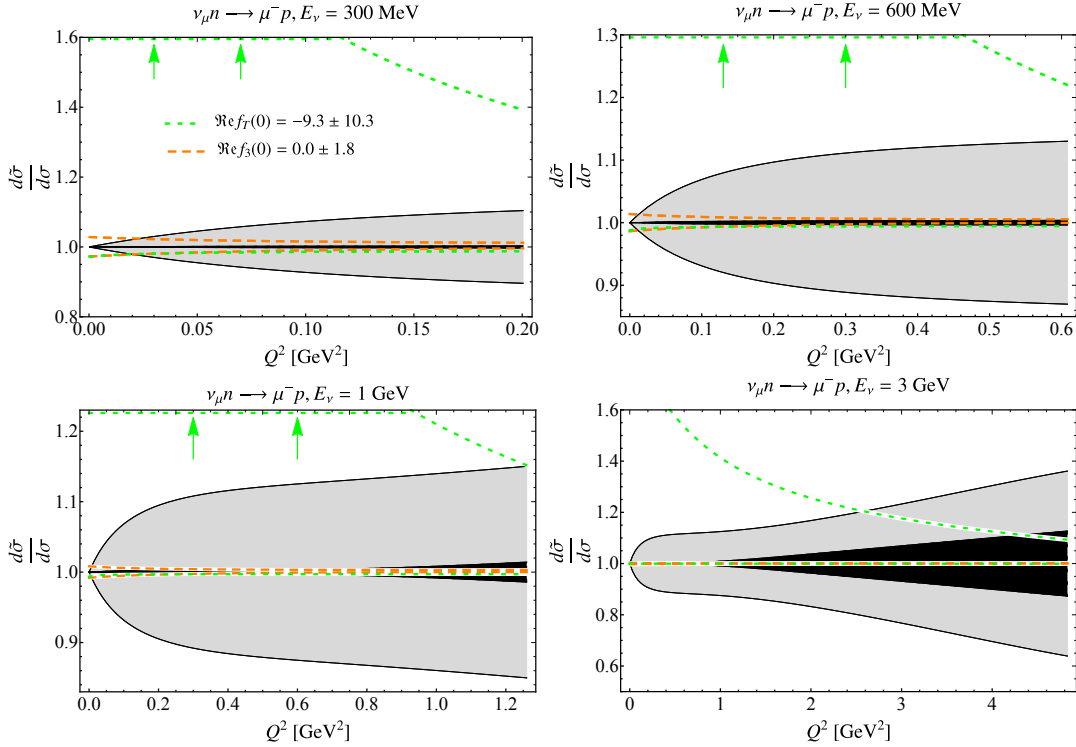


Figure 6: Ratio of unpolarized muon neutrino cross section with one extra real-valued amplitude to the tree-level result as a function of the squared momentum transfer Q^2 at fixed muon neutrino energies $E_\nu = 300$ MeV, 600 MeV, 1 GeV, and 3 GeV. The dark black and light gray bands correspond to vector and axial-vector uncertainty, respectively. Orange dashed and green dotted lines represent allowed regions for f_3 and f_T , respectively, as described in the text.

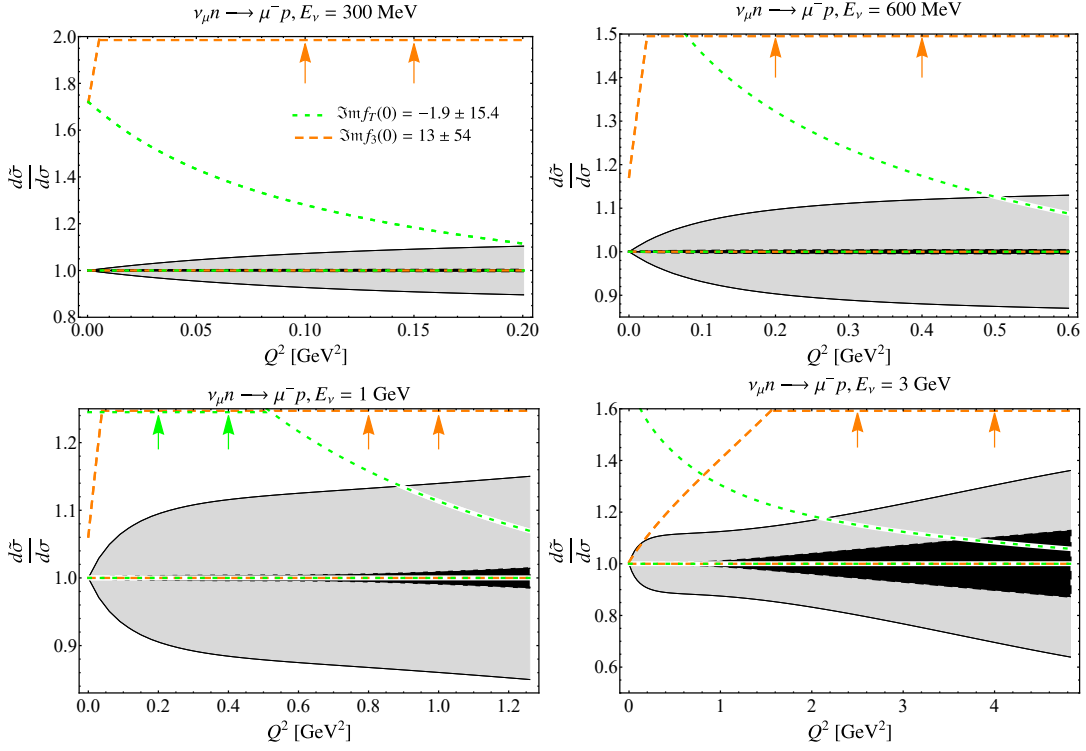


Figure 7: Same as Fig. 6, but for imaginary amplitudes.

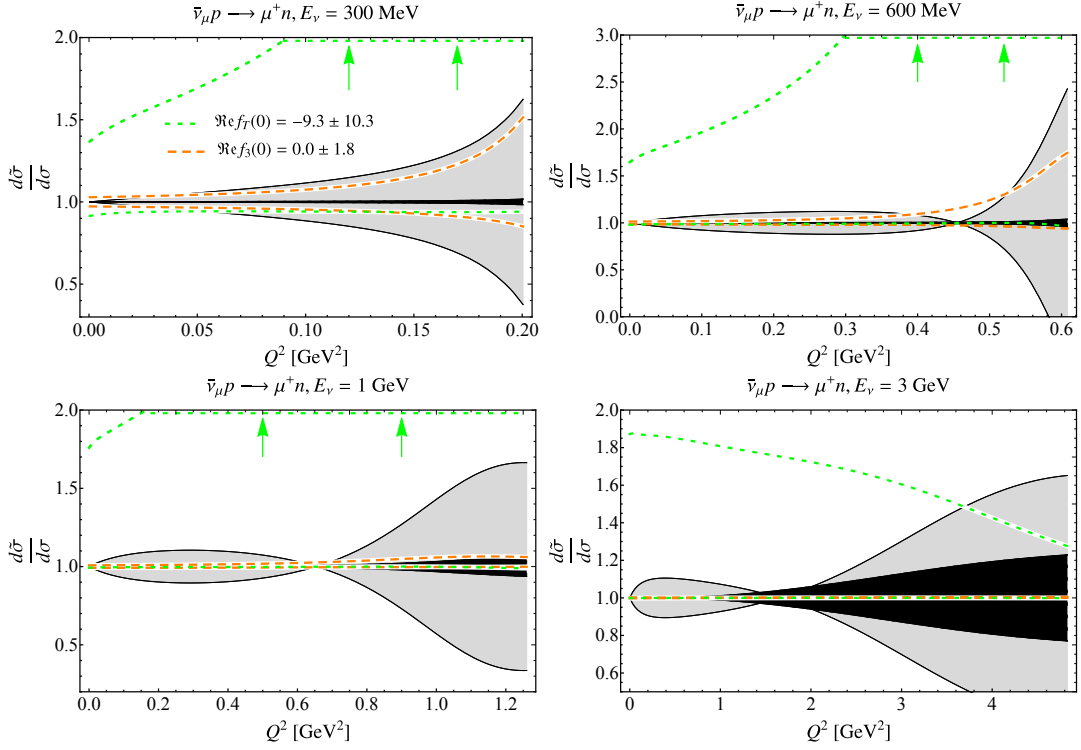


Figure 8: Same as Fig. 6 but for antineutrinos.

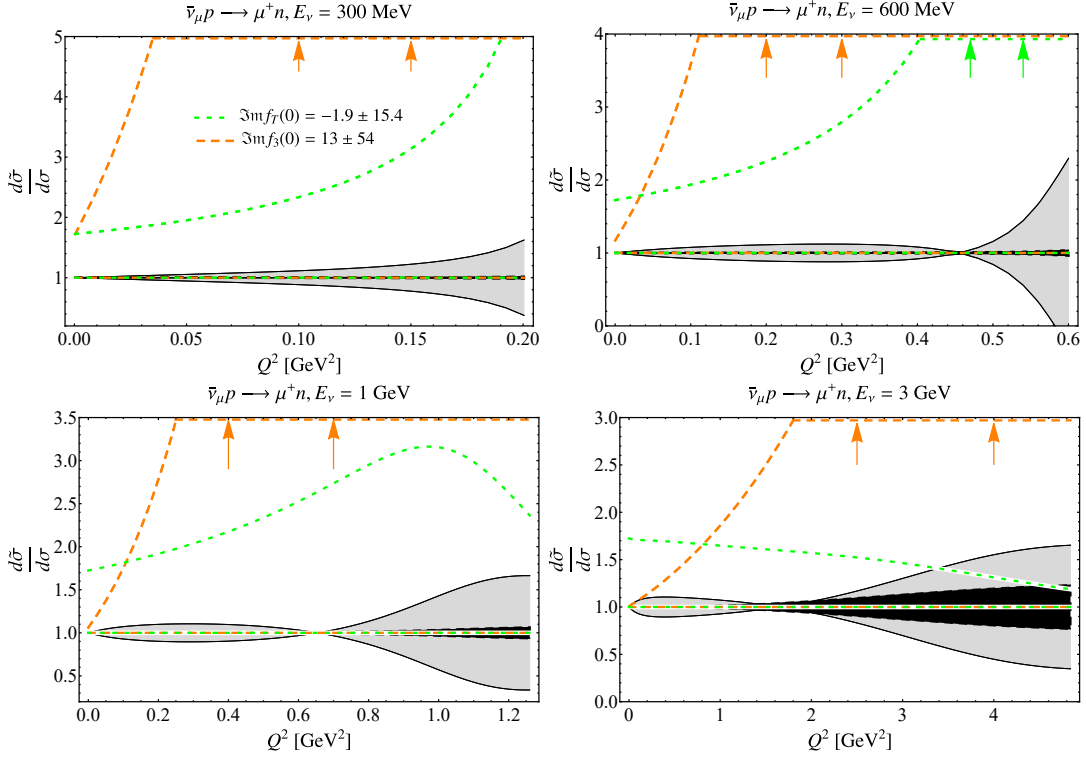


Figure 9: Same as Fig. 7 but for antineutrinos.

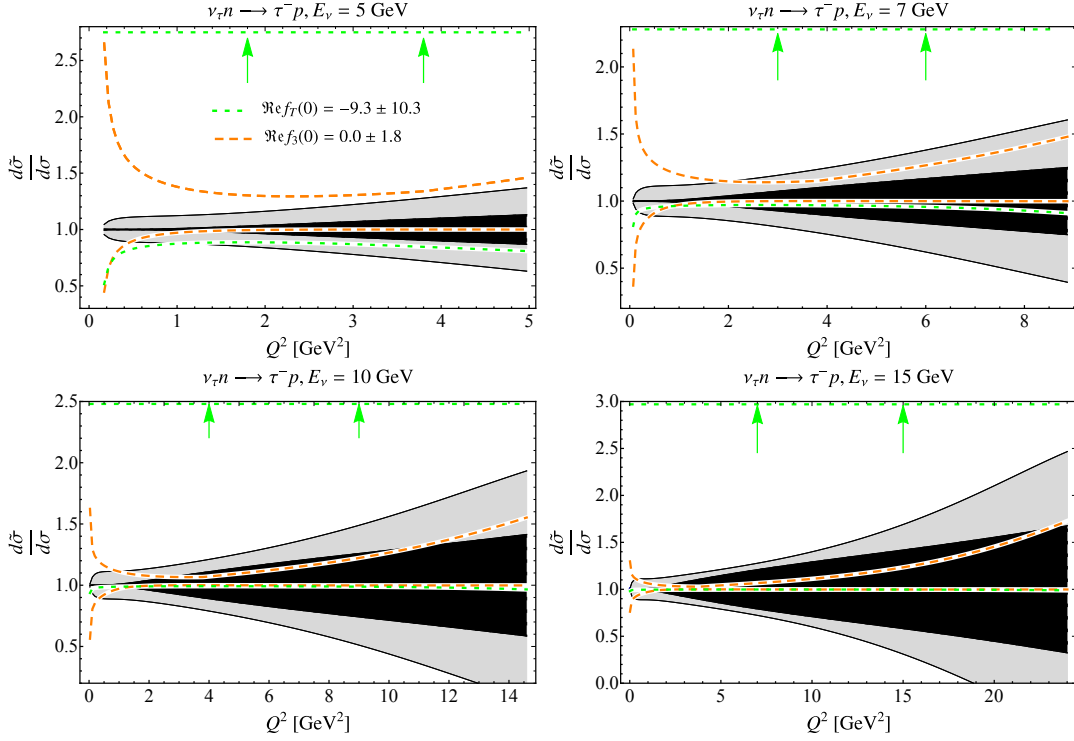


Figure 10: Same as Fig. 6 but for real amplitudes in the scattering of tau neutrinos at fixed beam energies $E_\nu = 5 \text{ GeV}, 7 \text{ GeV}, 10 \text{ GeV},$ and 15 GeV .

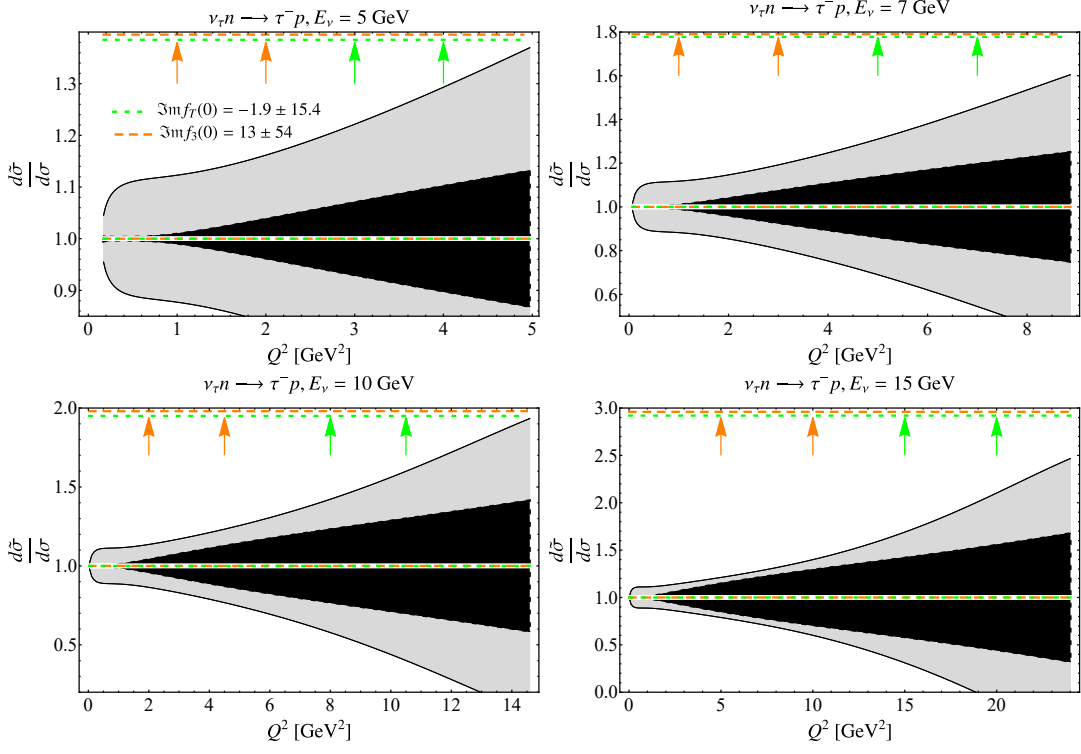


Figure 11: Same as Fig. 10 but for imaginary amplitudes.

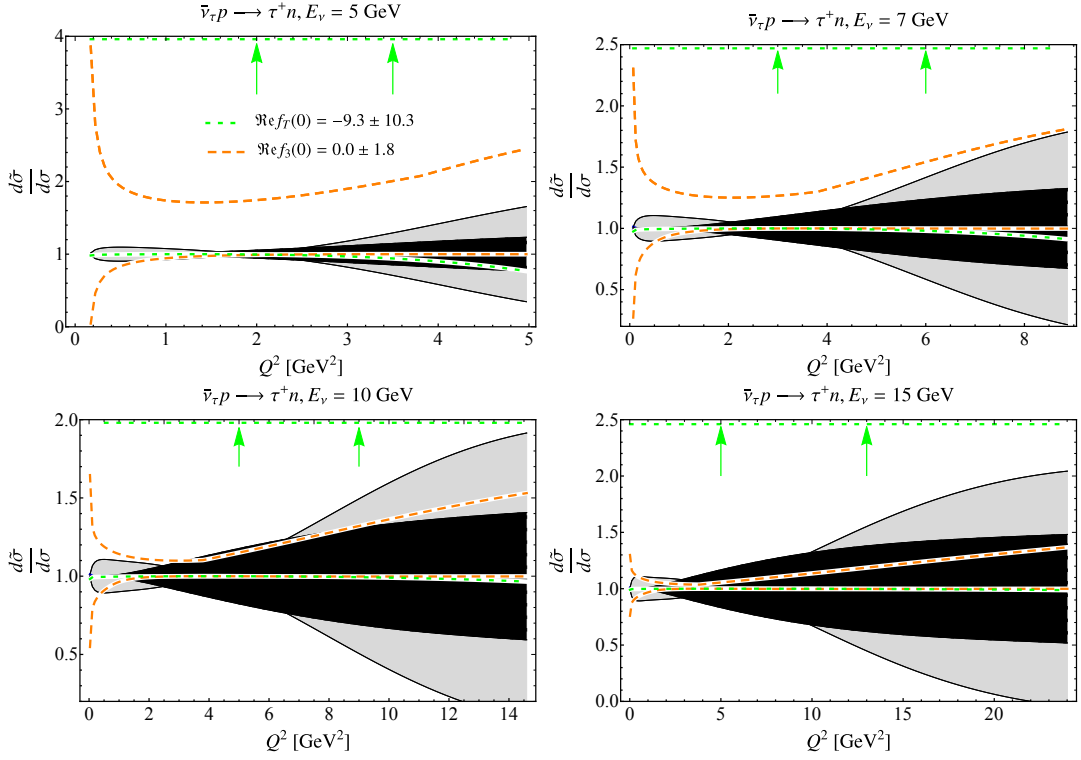


Figure 12: Same as Fig. 10 but for antineutrinos.

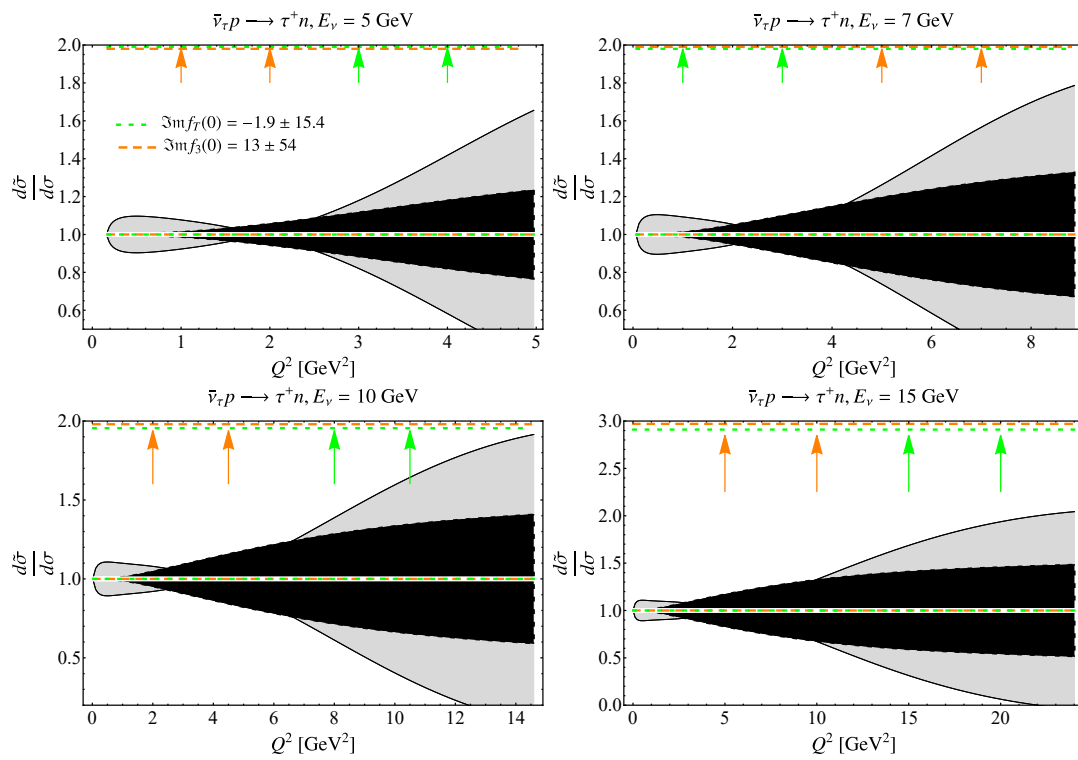


Figure 13: Same as Fig. 11 but for antineutrinos.

A.2 Polarization asymmetries, muon (anti)neutrino

In this Section, we present all independent single-spin asymmetries for muon neutrinos and antineutrinos, with one extra real- or imaginary-valued amplitude $f_i(\nu, Q^2) = [\Re f_i(0) + i\Im f_i(0)] / \left(1 + \frac{Q^2}{\Lambda^2}\right)^2$, for illustrative neutrino energies $E_\nu = 300$ MeV, 600 MeV, 1 GeV, and 3 GeV, and $\Lambda = 1$ GeV. We vary the amplitude normalizations within the ranges from Table 1, and compare to the uncertainty from vector and axial-vector form factors from Sec. 4.

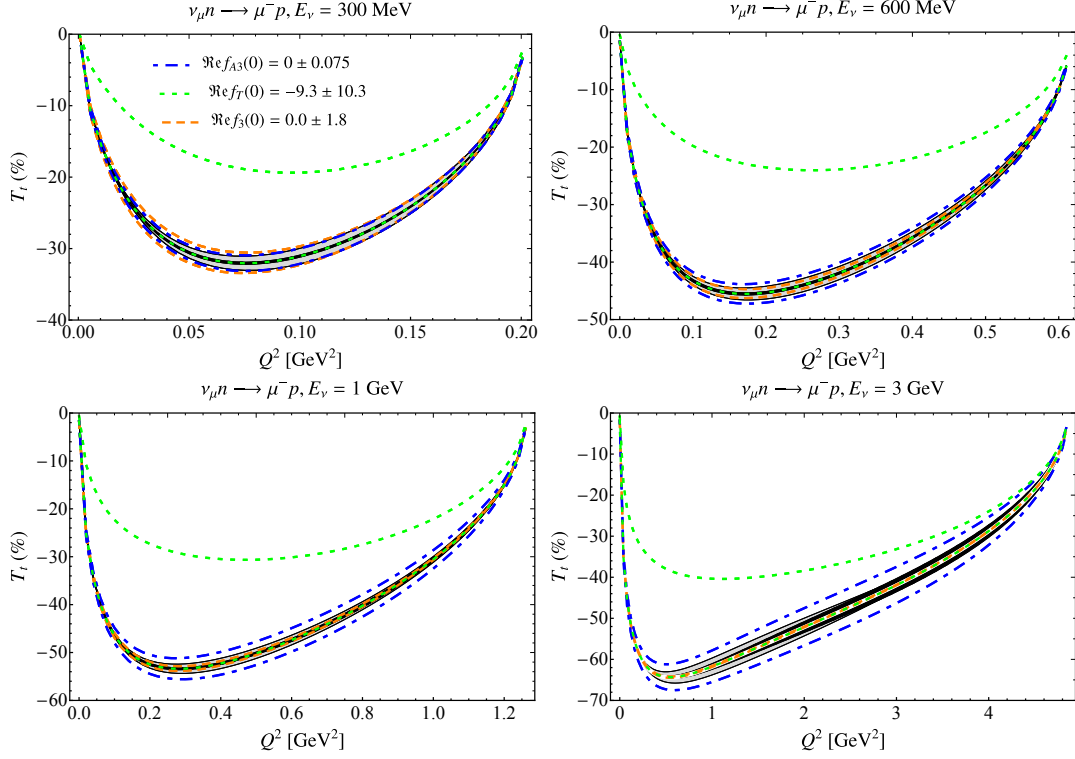


Figure 14: Transverse polarization observable, T_t , with one extra real-valued amplitude, compared to the tree-level result at fixed muon neutrino energies $E_\nu = 300$ MeV, 600 MeV, 1 GeV, and 3 GeV. The dark black and light gray bands correspond to vector and axial-vector uncertainty, respectively. Orange dashed, green dotted, and blue dashed-dotted lines represent allowed regions for f_3 , f_T , and f_{A3} , respectively, as described in the text.

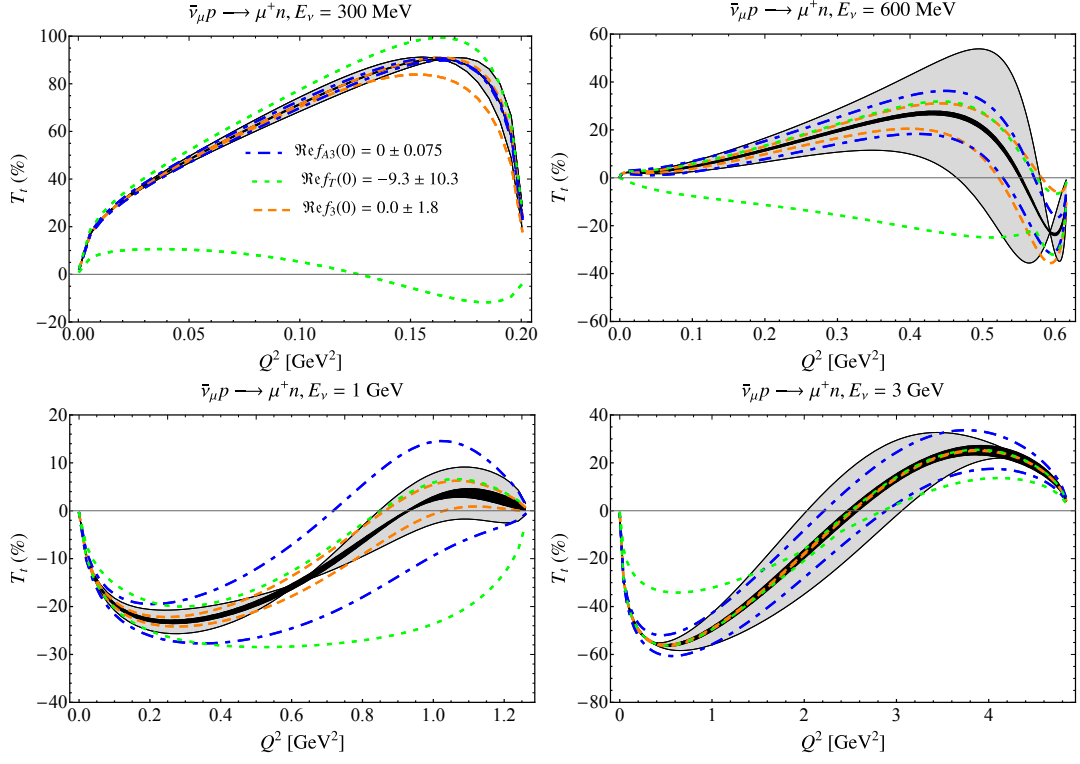


Figure 15: Same as Fig. 14 but for antineutrinos.

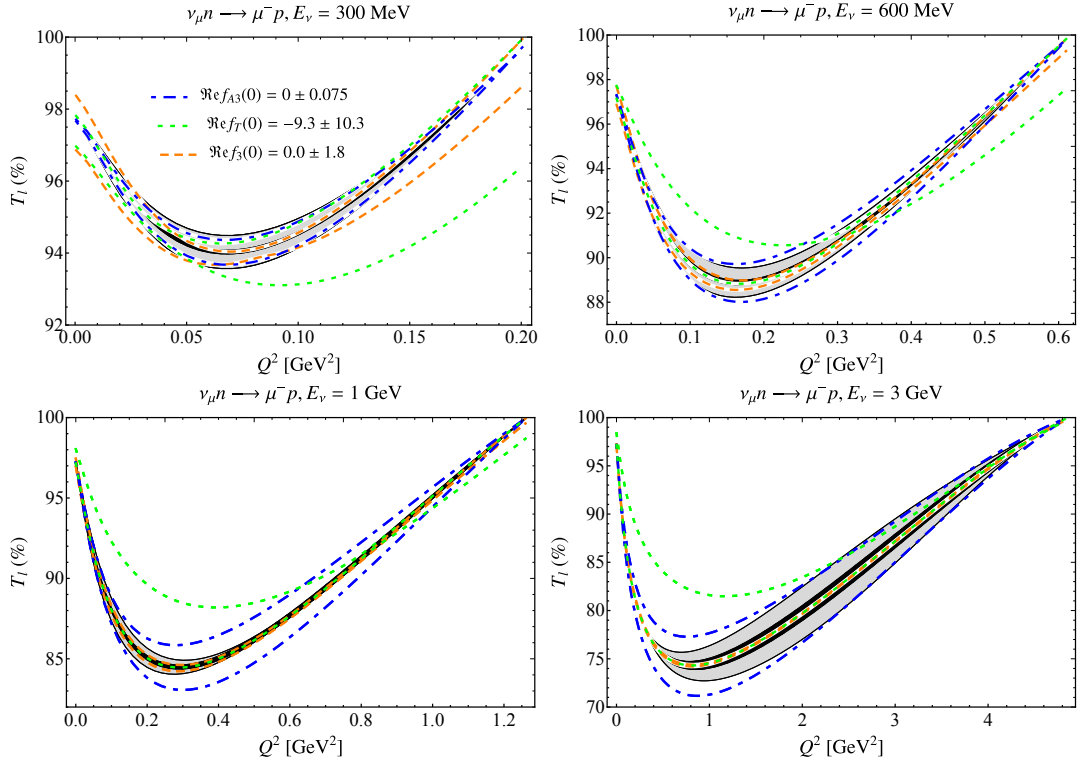


Figure 16: Same as Fig. 14 but for the longitudinal polarization observable T_l .

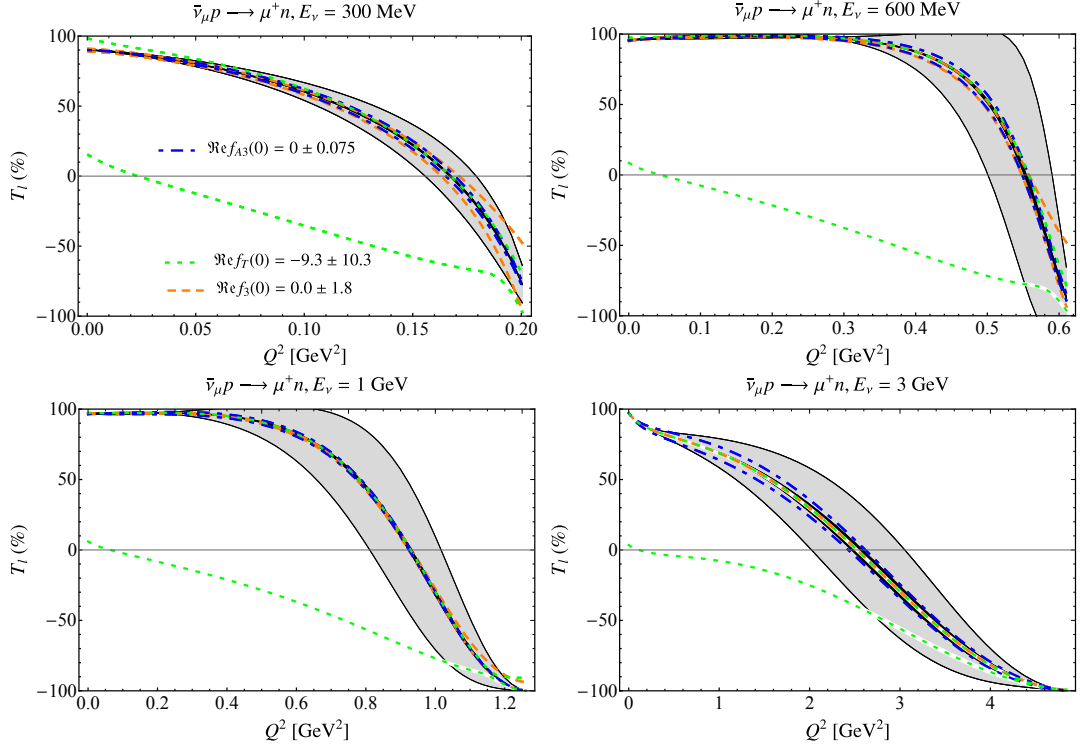


Figure 17: Same as Fig. 15 but for the longitudinal polarization observable T_L .

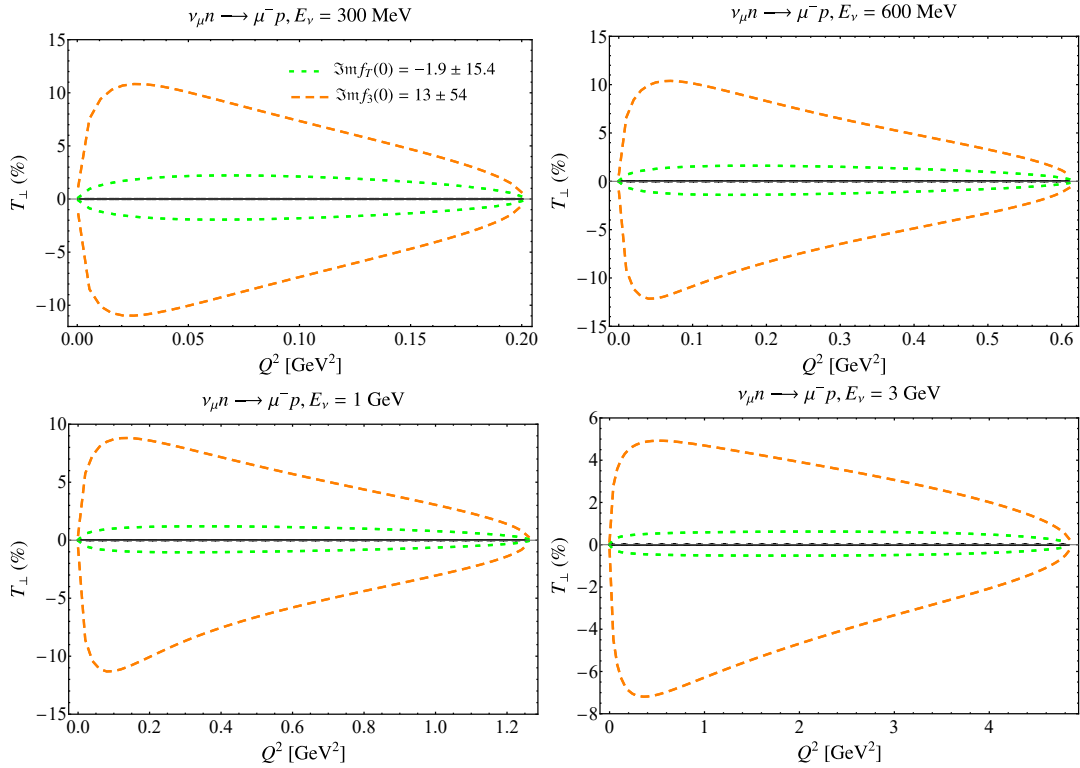


Figure 18: Same as Fig. 14 but for the transverse polarization observable T_\perp and imaginary amplitudes.

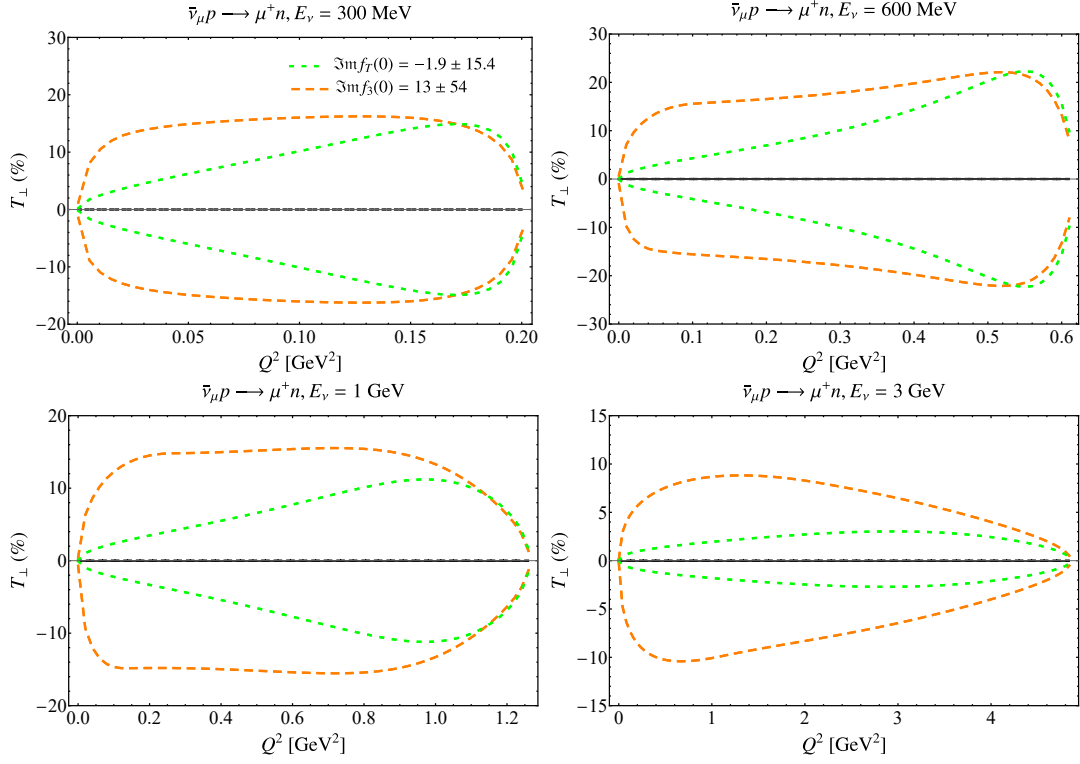


Figure 19: Same as Fig. 15 but for the transverse polarization observable T_{\perp} and imaginary amplitudes.

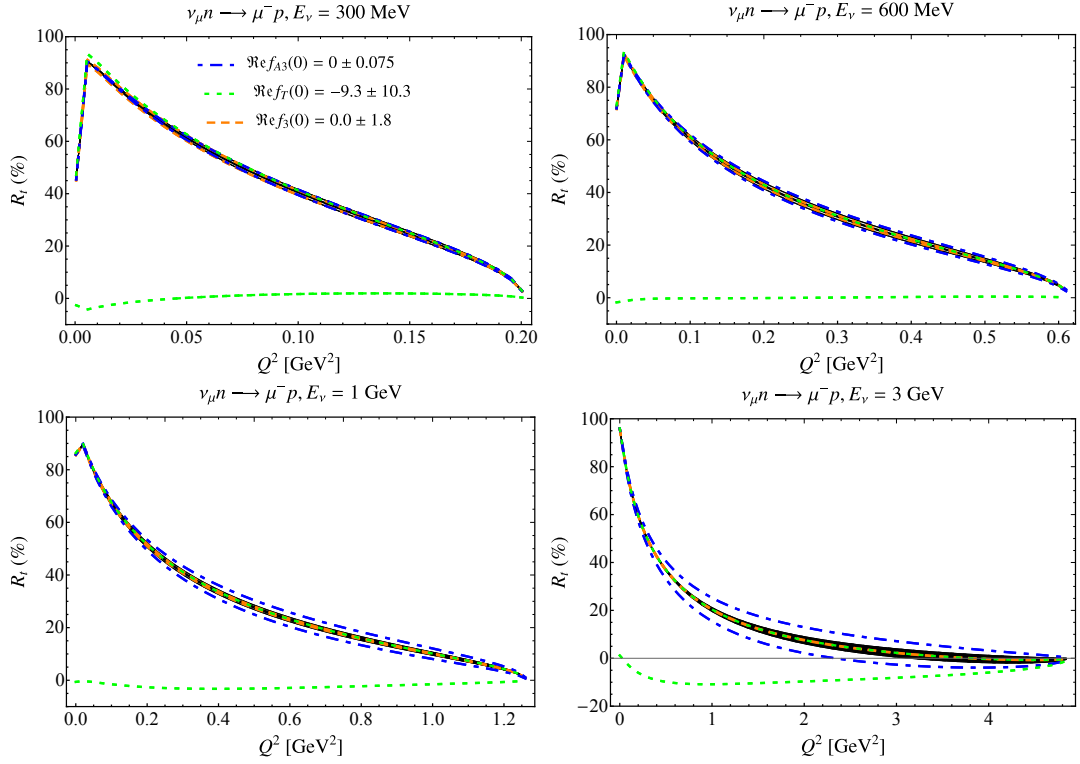


Figure 20: Same as Fig. 14 but for the transverse polarization observable R_t .

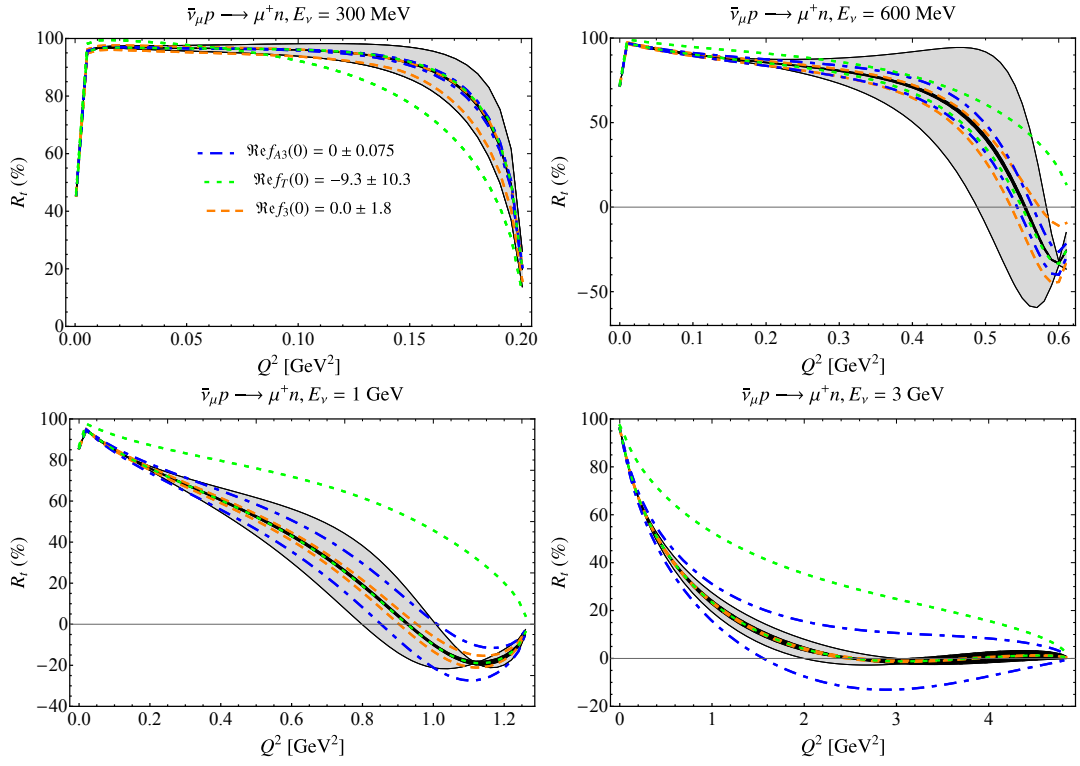


Figure 21: Same as Fig. 15 but for the transverse polarization observable R_t .

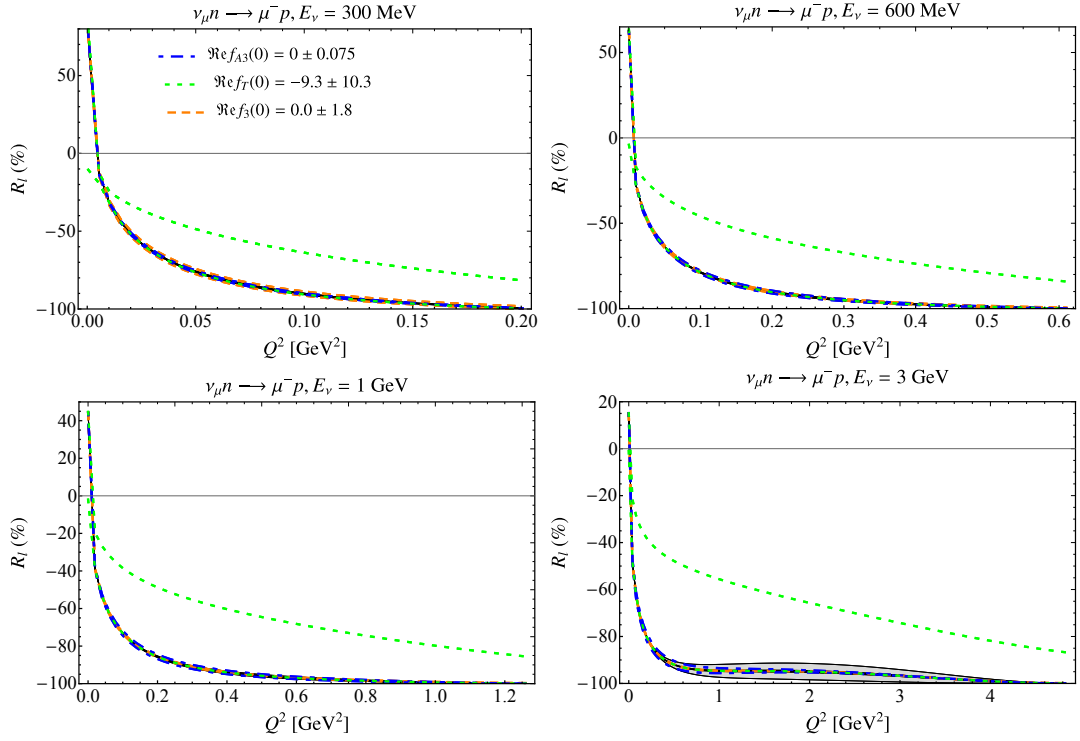


Figure 22: Same as Fig. 14 but for the longitudinal polarization observable R_l .

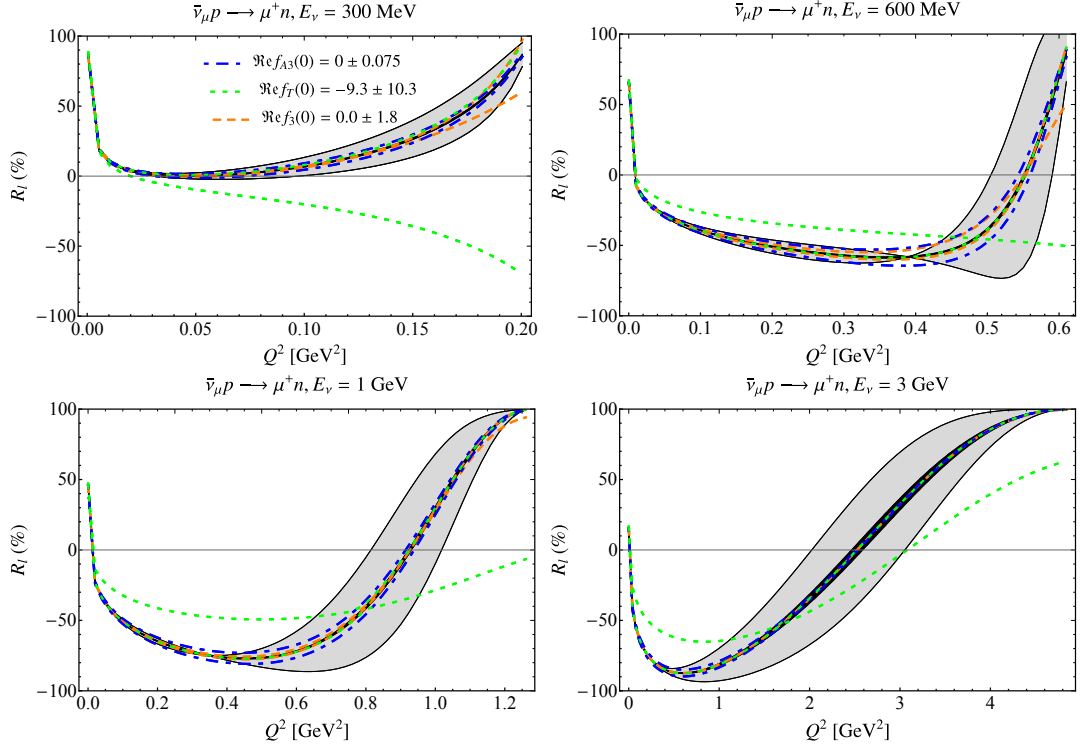


Figure 23: Same as Fig. 15 but for the longitudinal polarization observable R_l .

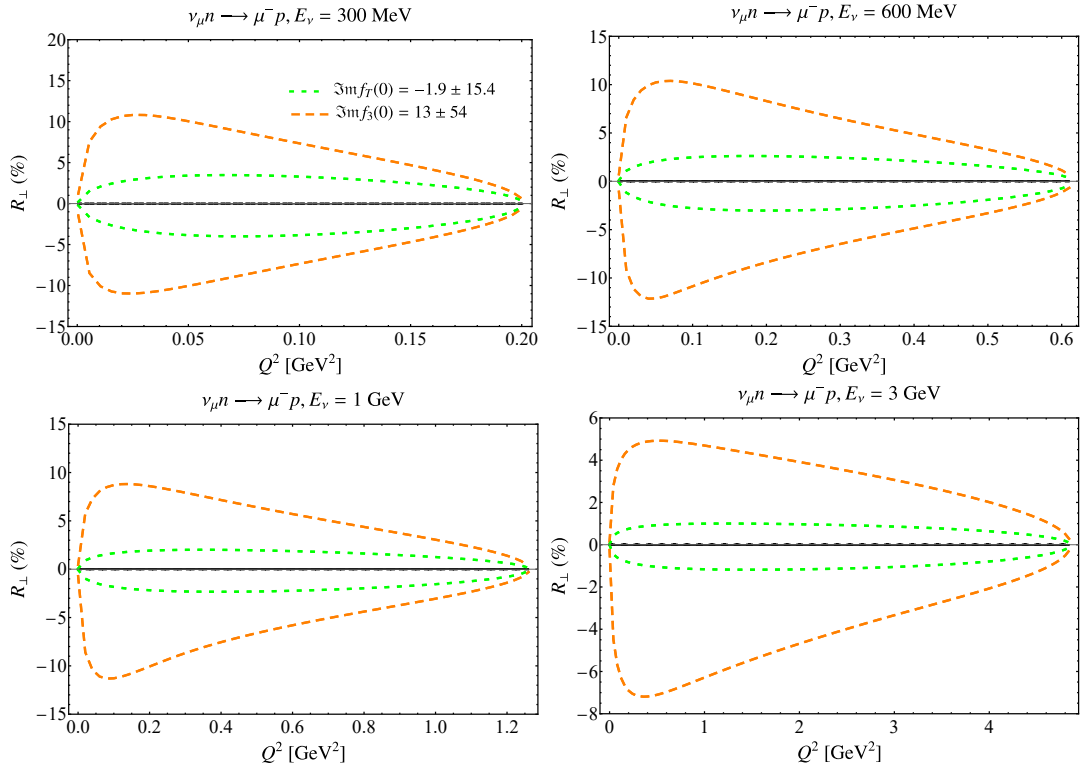


Figure 24: Same as Fig. 14 but for the transverse polarization observable R_\perp and imaginary amplitudes.

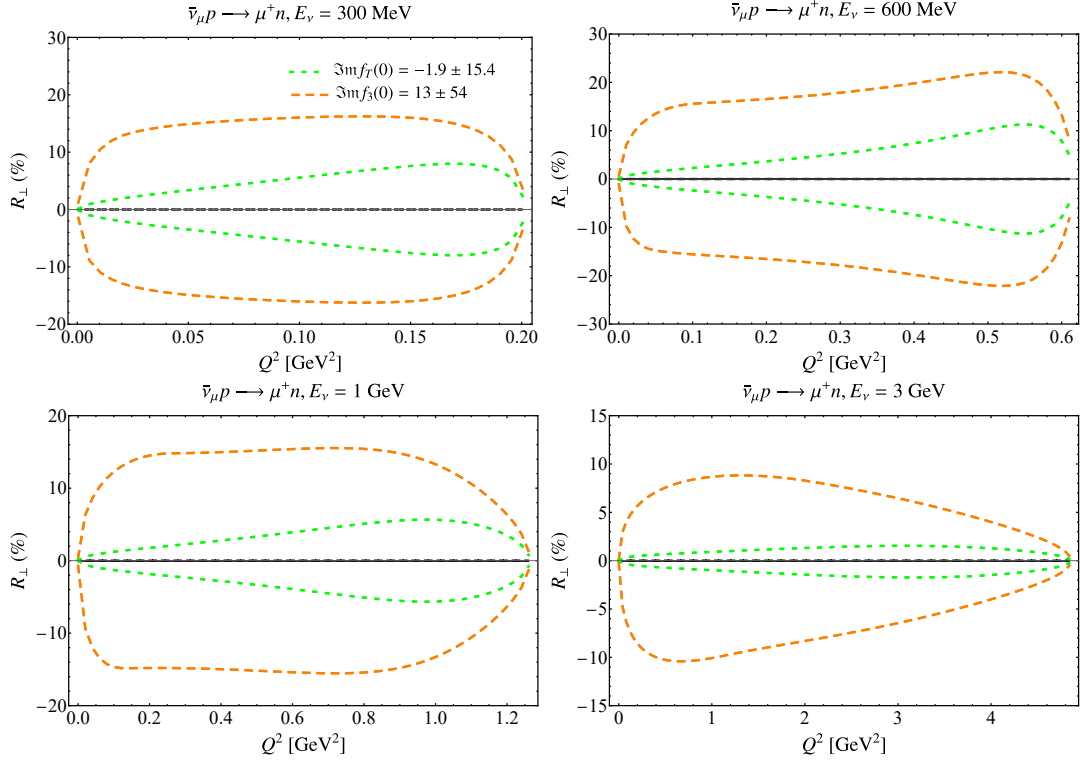


Figure 25: Same as Fig. 15 but for the transverse polarization observable R_{\perp} and imaginary amplitudes.

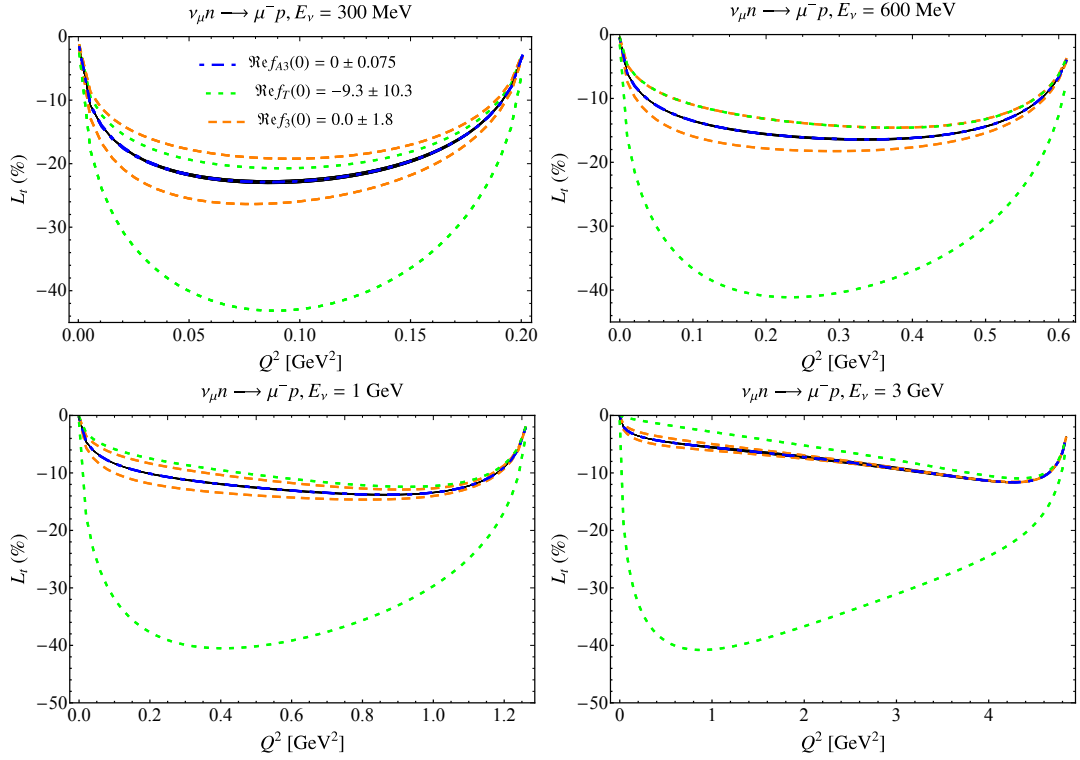


Figure 26: Same as Fig. 14 but for the transverse polarization observable L_t .

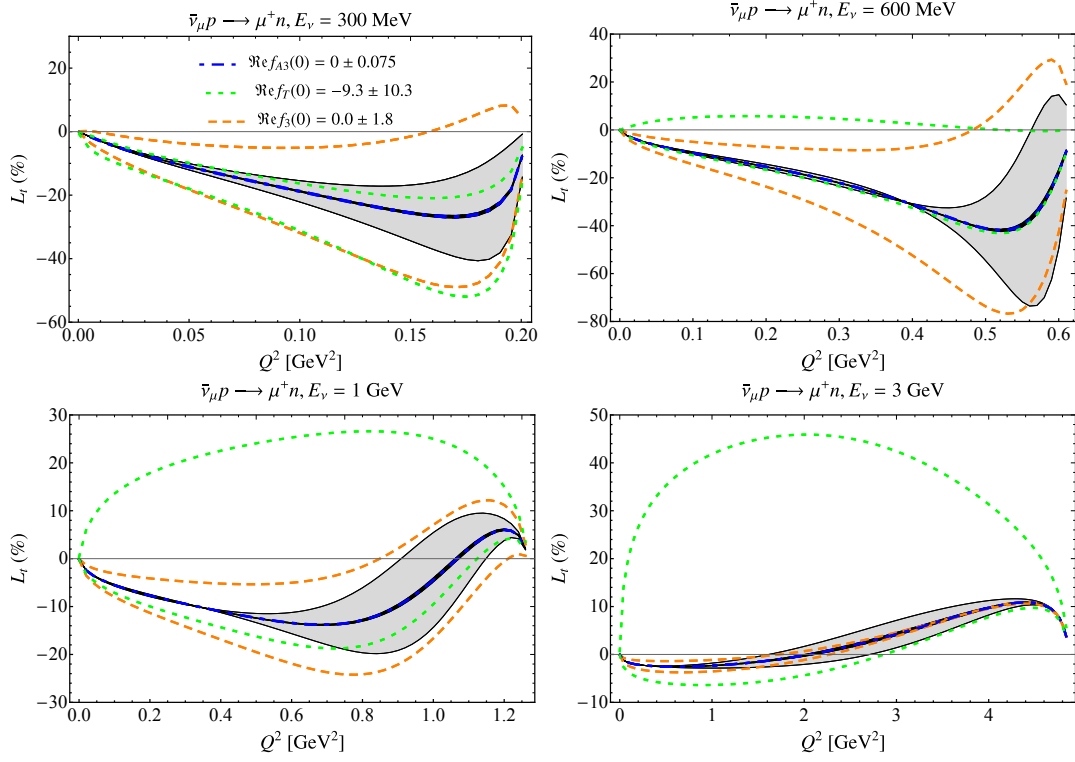


Figure 27: Same as Fig. 15 but for the transverse polarization observable L_t .

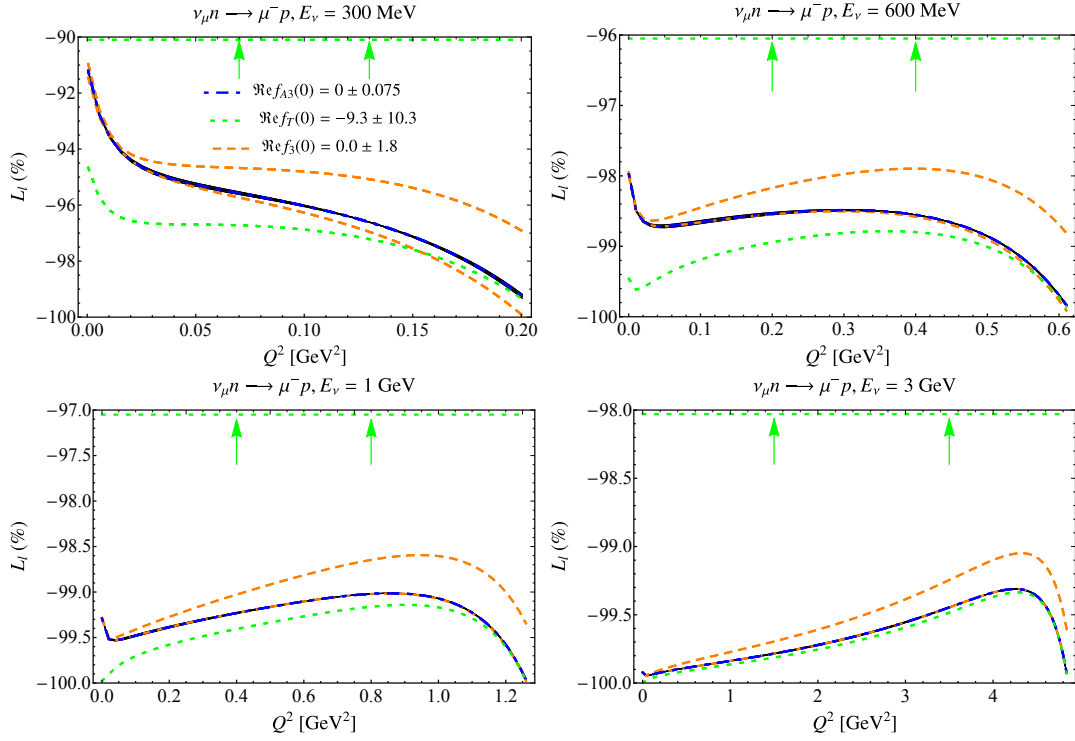


Figure 28: Same as Fig. 14 but for the longitudinal polarization observable L_l .

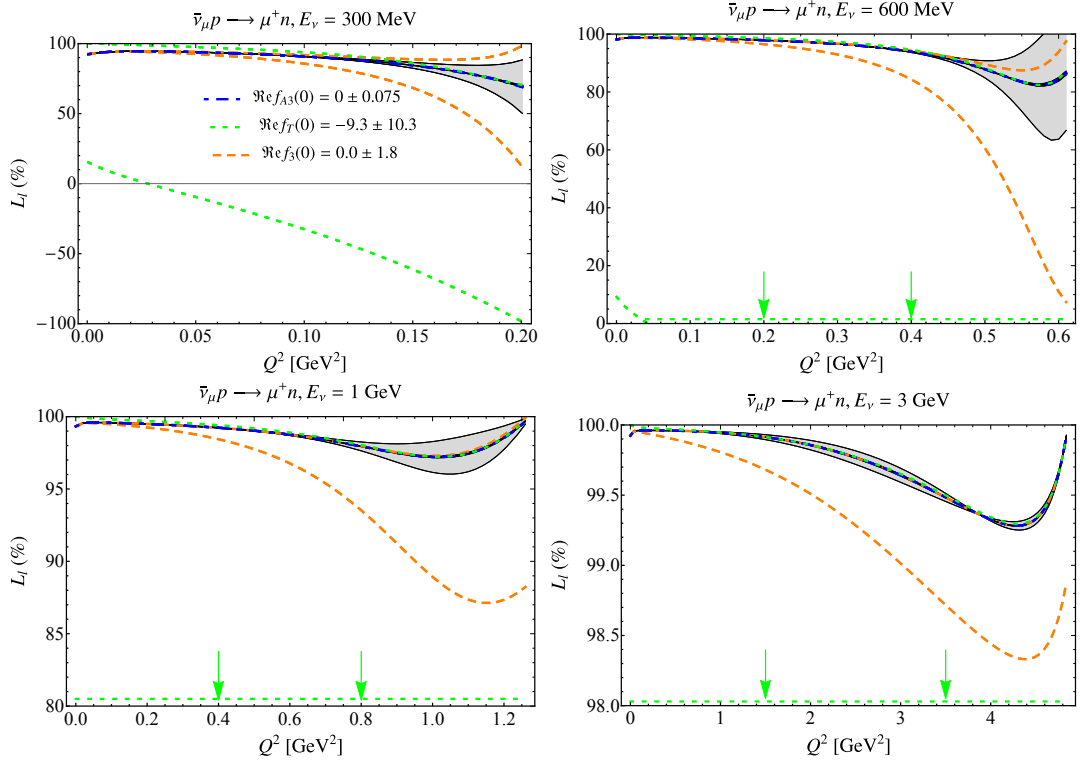


Figure 29: Same as Fig. 15 but for the longitudinal polarization observable L_L .

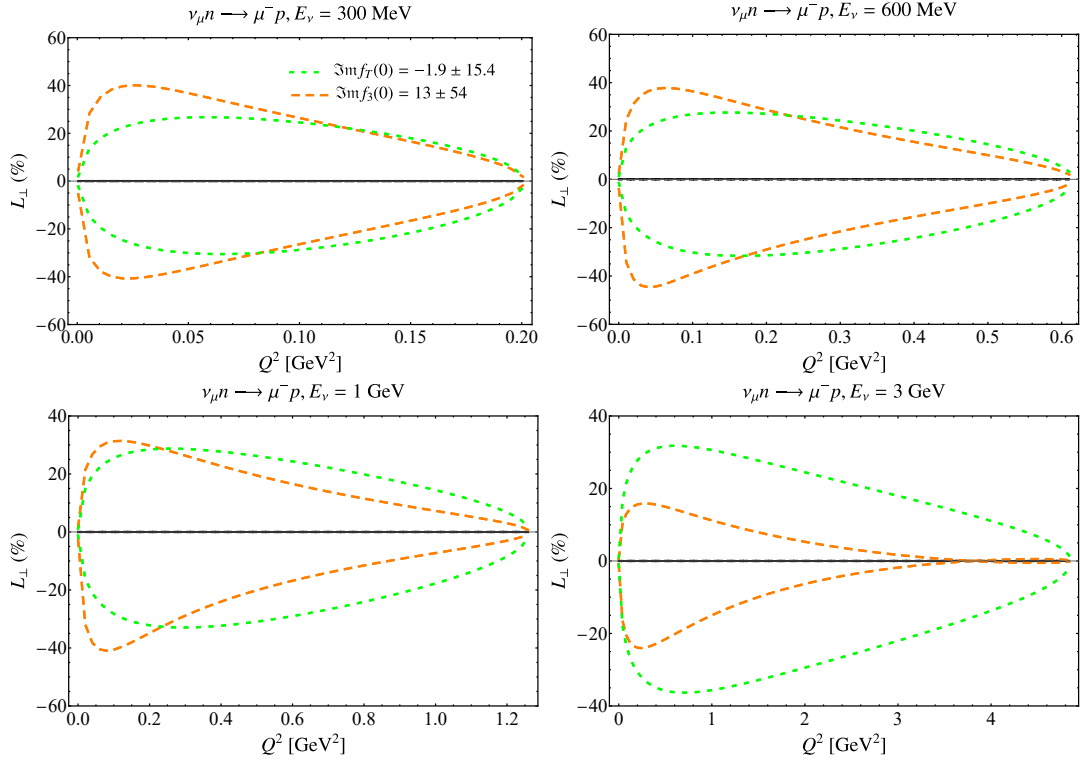


Figure 30: Same as Fig. 14 but for the transverse polarization observable L_\perp and imaginary amplitudes.

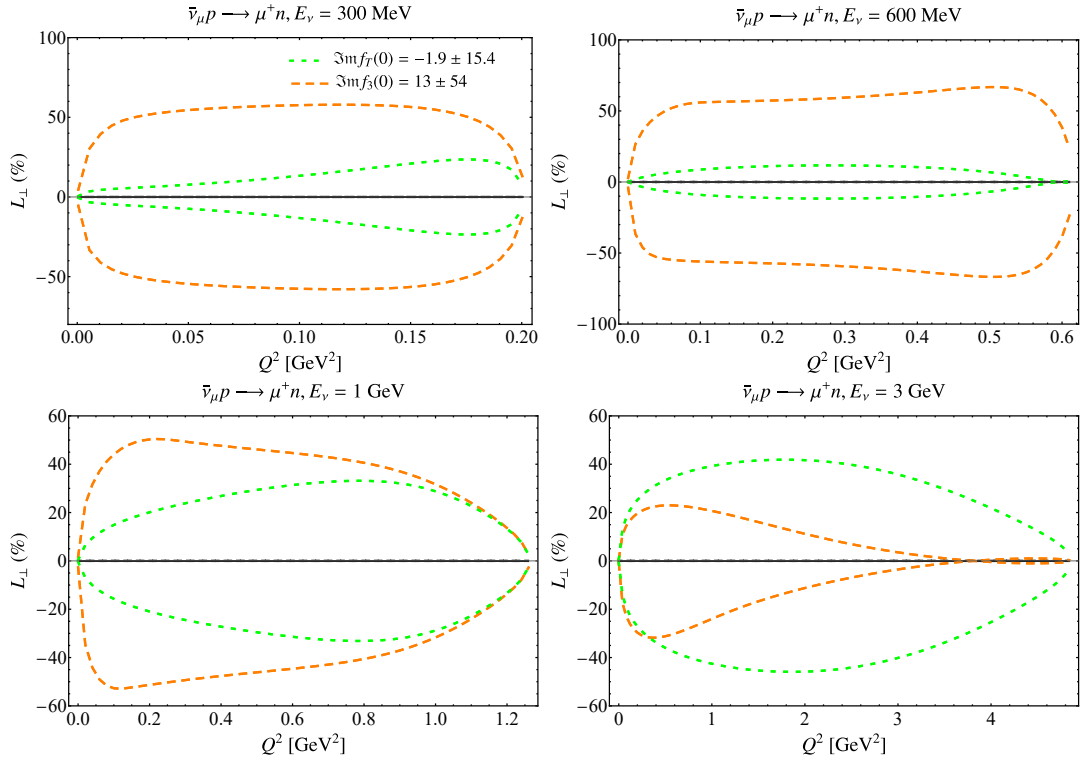


Figure 31: Same as Fig. 15 but for the transverse polarization observable L_{\perp} and imaginary amplitudes.

A.3 Polarization asymmetries, tau (anti)neutrino

In this Section, we present all independent single-spin asymmetries for tau neutrinos and antineutrinos, with one extra real- or imaginary-valued amplitude $f_i(\nu, Q^2) = [\Re f_i(0) + i\Im f_i(0)] / \left(1 + \frac{Q^2}{\Lambda^2}\right)^2$, for illustrative neutrino energies $E_\nu = 5$ GeV, 7 GeV, 10 GeV, and 15 GeV, and $\Lambda = 1$ GeV. We vary the amplitude normalizations within the ranges from Table 1, and compare to the uncertainty from vector and axial-vector form factors from Sec. 4.

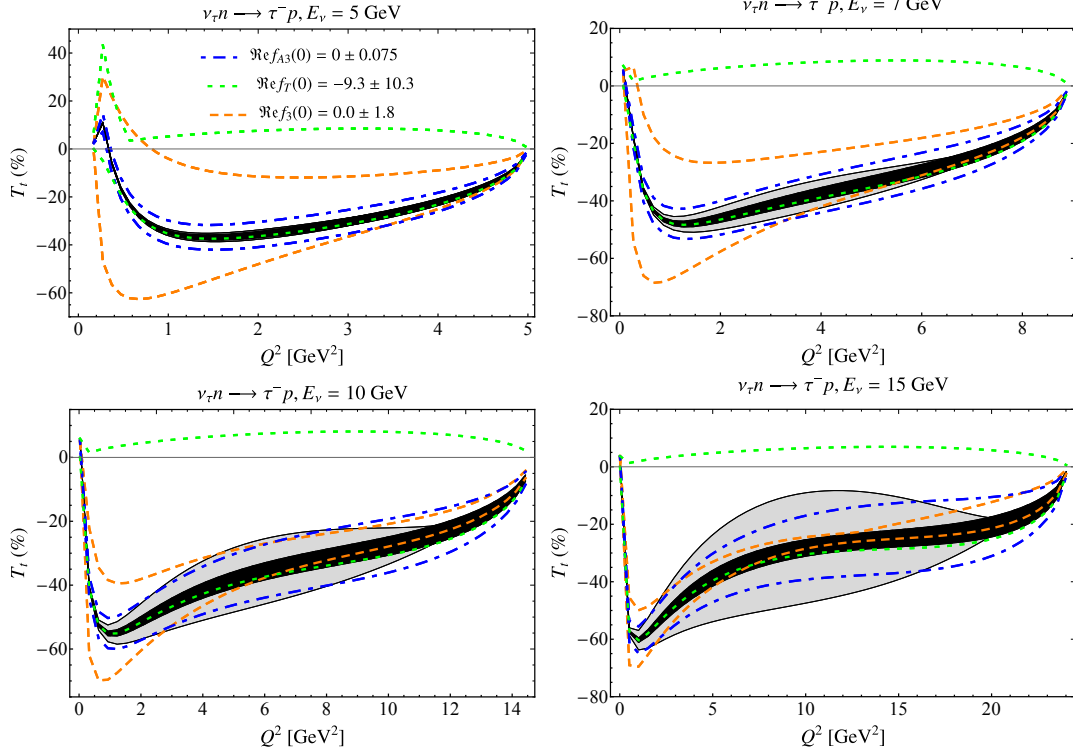


Figure 32: Transverse polarization observable, T_t , with one extra real-valued amplitude, compared to the tree-level result at fixed tau neutrino energies $E_\nu = 5$ GeV, 7 GeV, 10 GeV, and 15 GeV. The dark black and light gray bands correspond to vector and axial-vector uncertainty, respectively. Orange dashed, green dotted, and blue dashed-dotted lines represent allowed regions for f_3 , f_T , and f_{A3} , respectively, as described in the text.

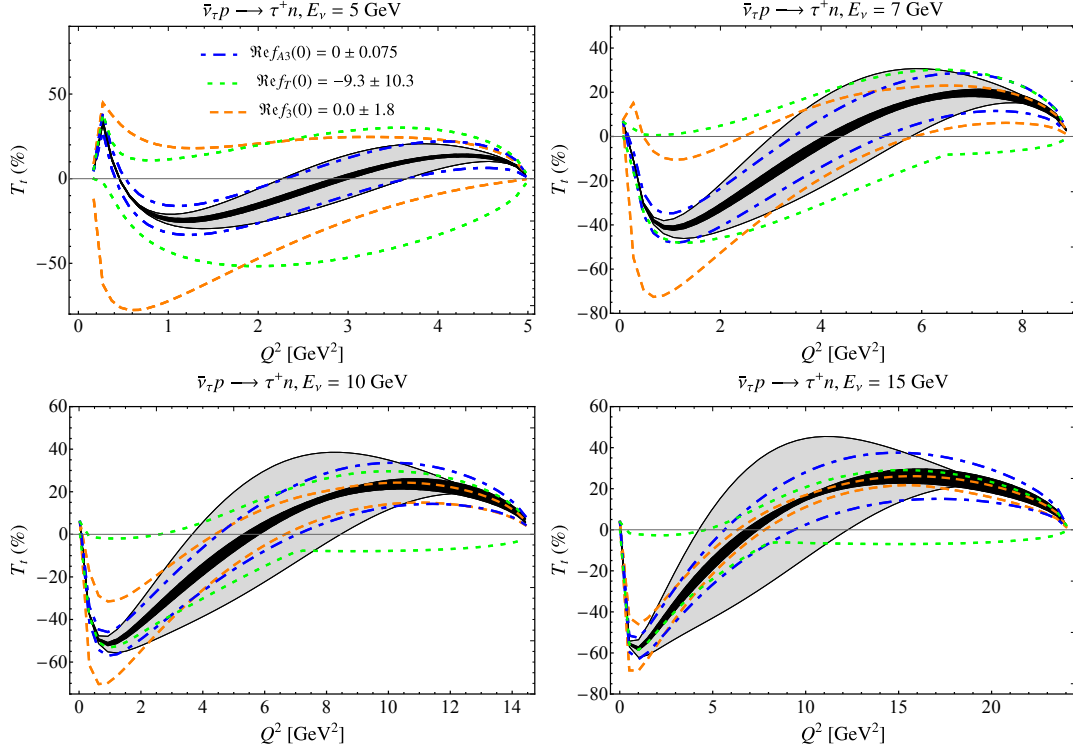


Figure 33: Same as Fig. 32 but for antineutrinos.

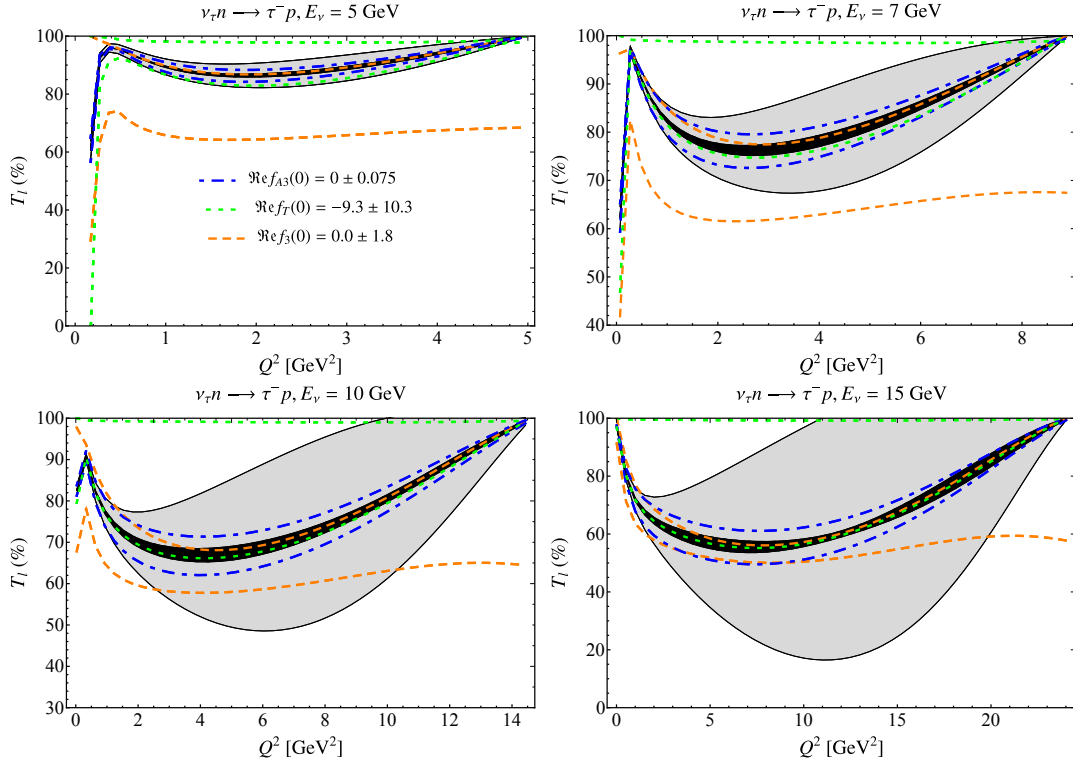


Figure 34: Same as Fig. 32 but for the longitudinal polarization observable T_L .

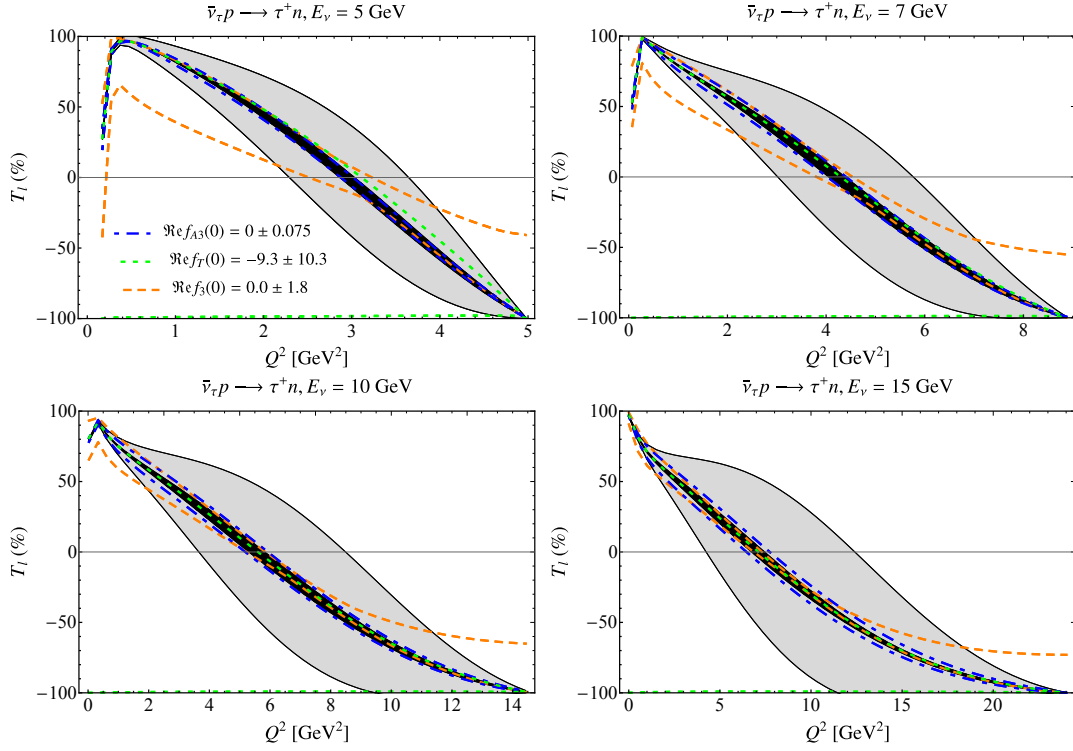


Figure 35: Same as Fig. 33 but for the longitudinal polarization observable T_L .

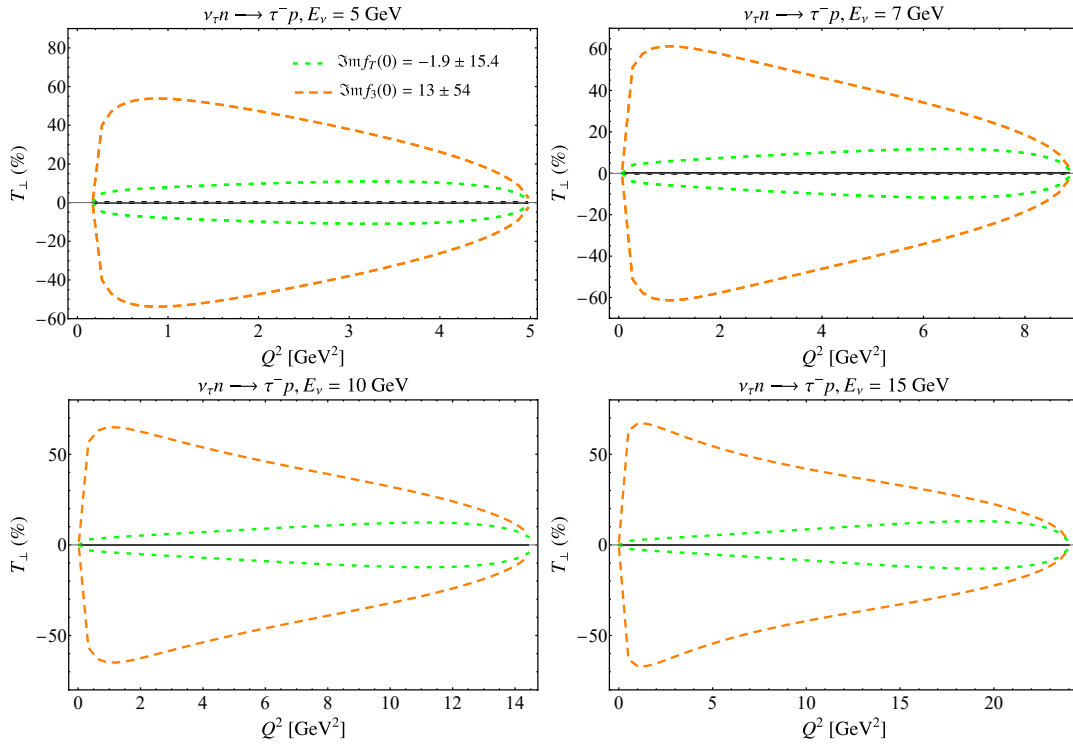


Figure 36: Same as Fig. 32 but for the transverse polarization observable T_\perp and imaginary amplitudes.

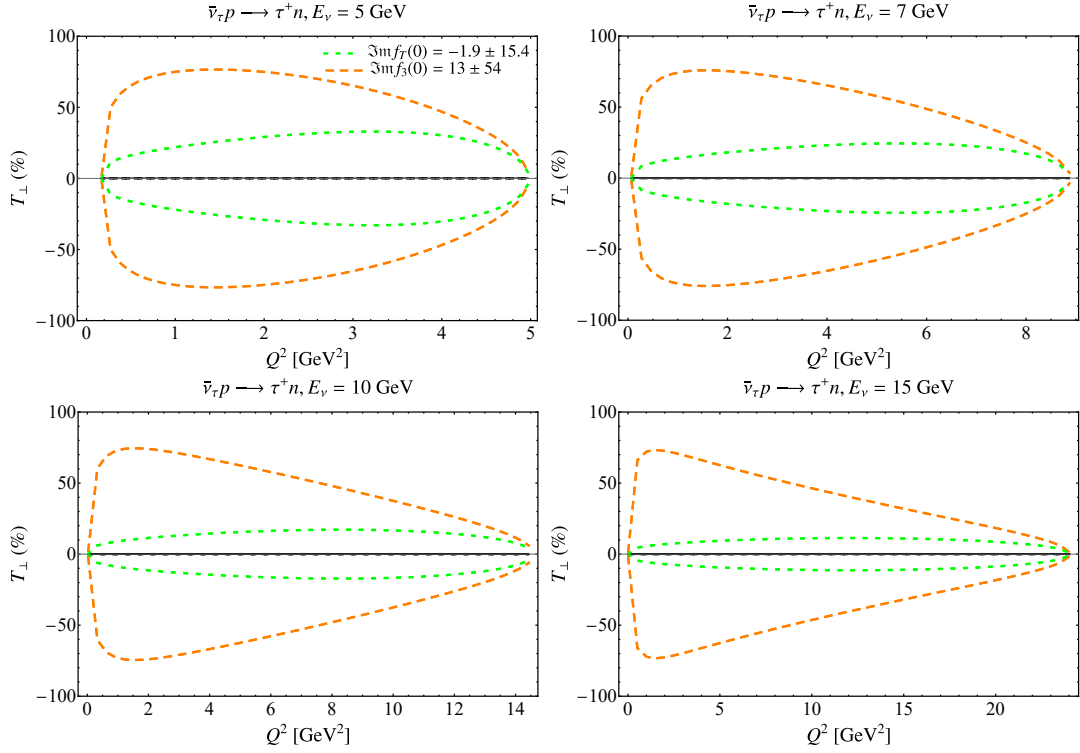


Figure 37: Same as Fig. 33 but for the transverse polarization observable T_{\perp} and imaginary amplitudes.

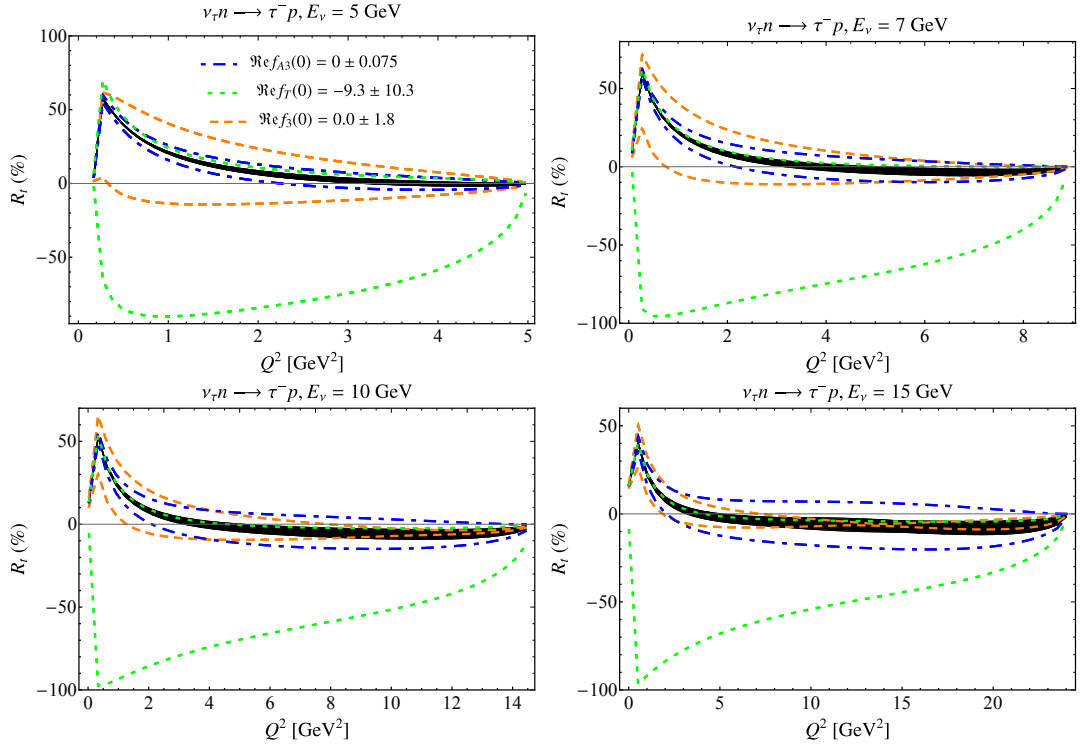


Figure 38: Same as Fig. 32 but for the transverse polarization observable R_t .

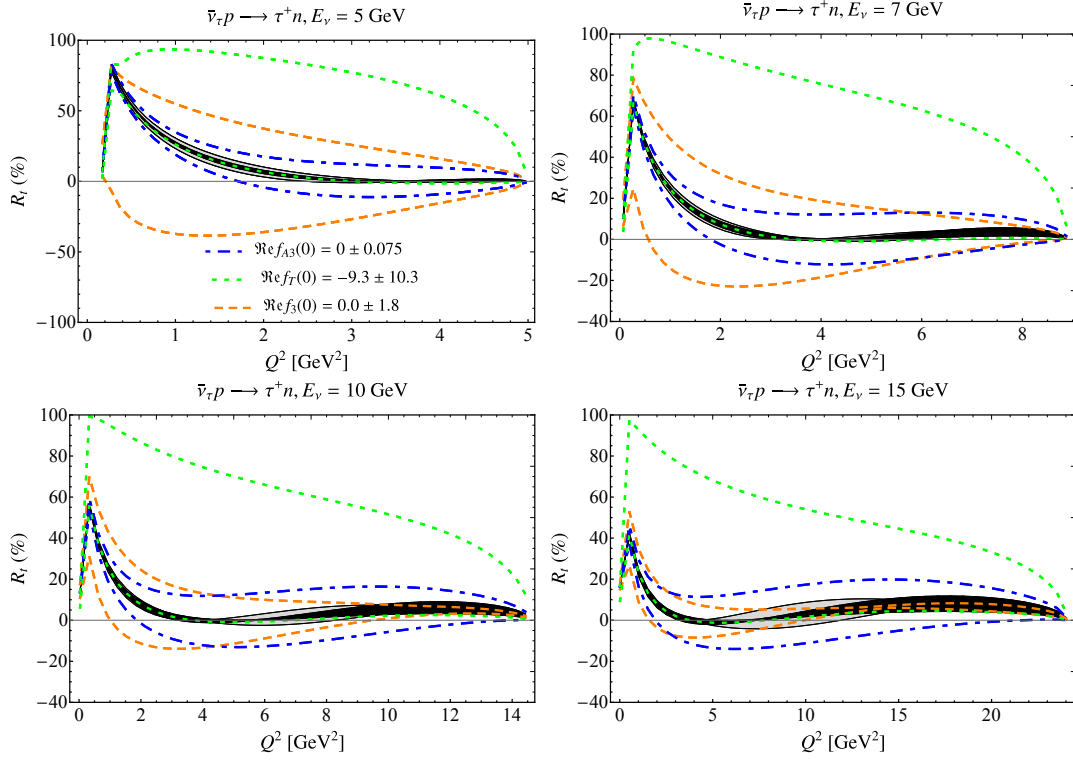


Figure 39: Same as Fig. 33 but for the transverse polarization observable R_t .

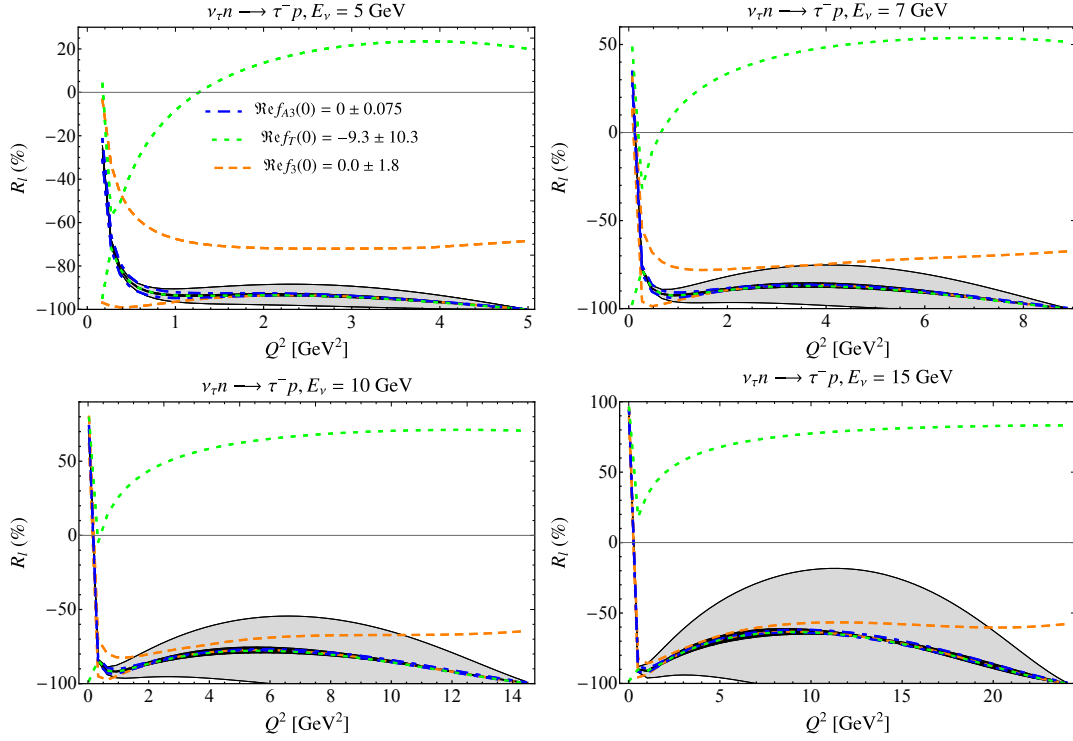


Figure 40: Same as Fig. 32 but for the longitudinal polarization observable R_l .

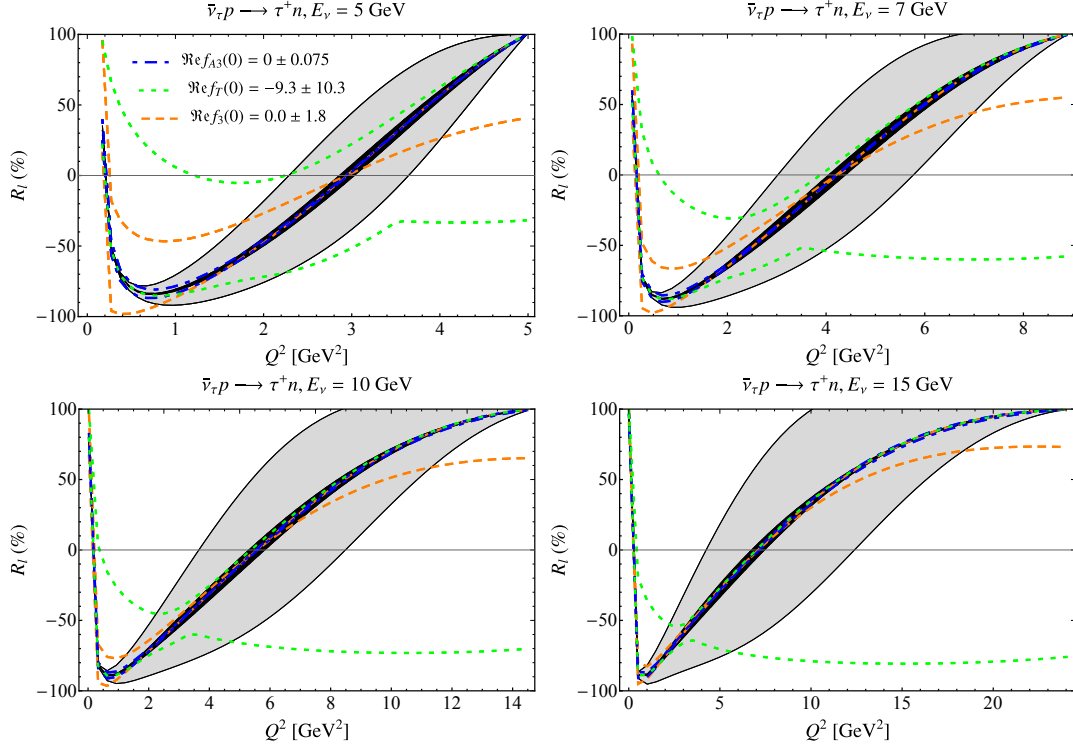


Figure 41: Same as Fig. 33 but for the longitudinal polarization observable R_l .

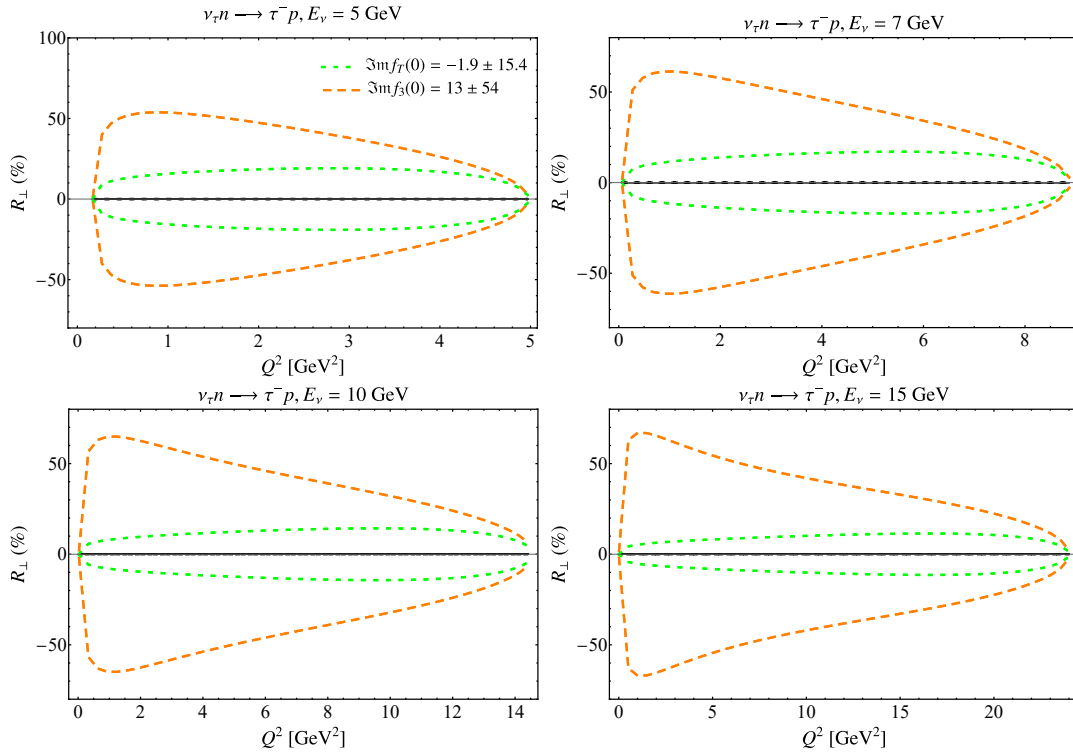


Figure 42: Same as Fig. 32 but for the transverse polarization observable R_\perp and imaginary amplitudes.

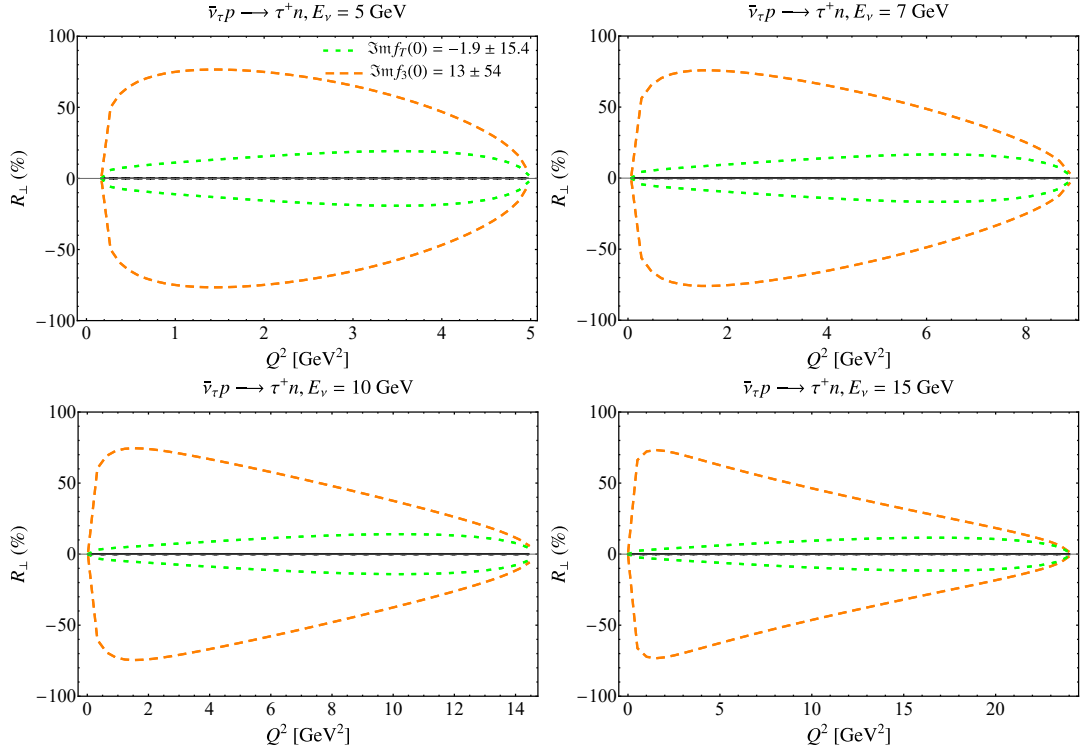


Figure 43: Same as Fig. 33 but for the transverse polarization observable R_{\perp} and imaginary amplitudes.

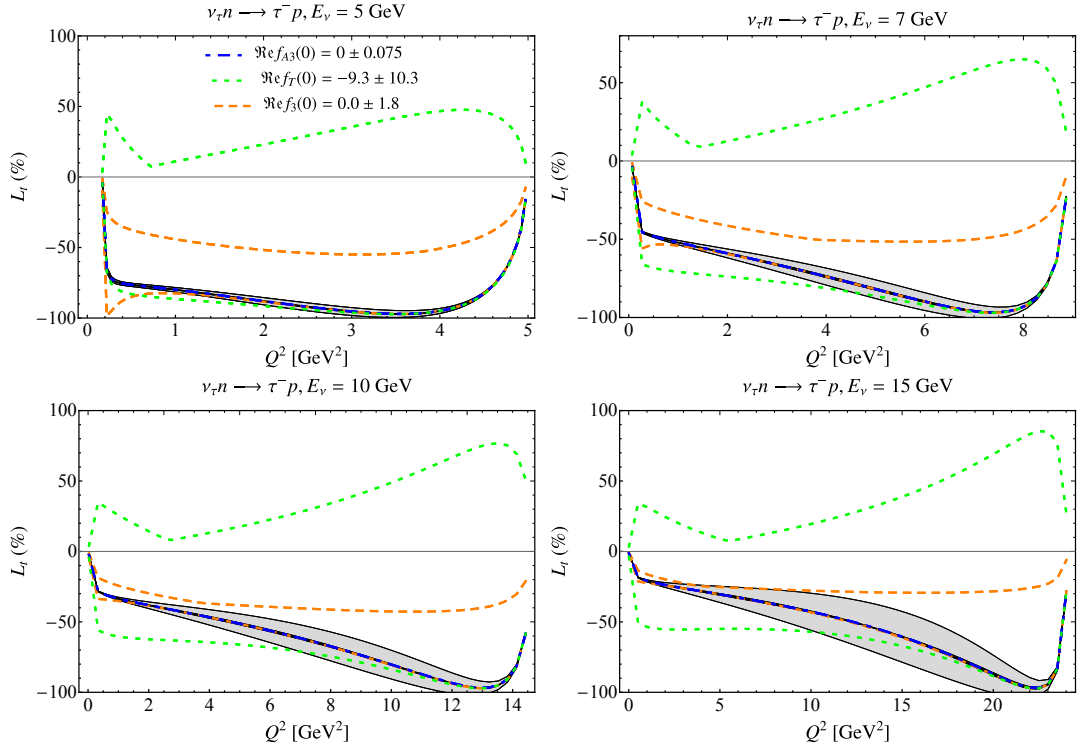


Figure 44: Same as Fig. 32 but for the transverse polarization observable L_t .

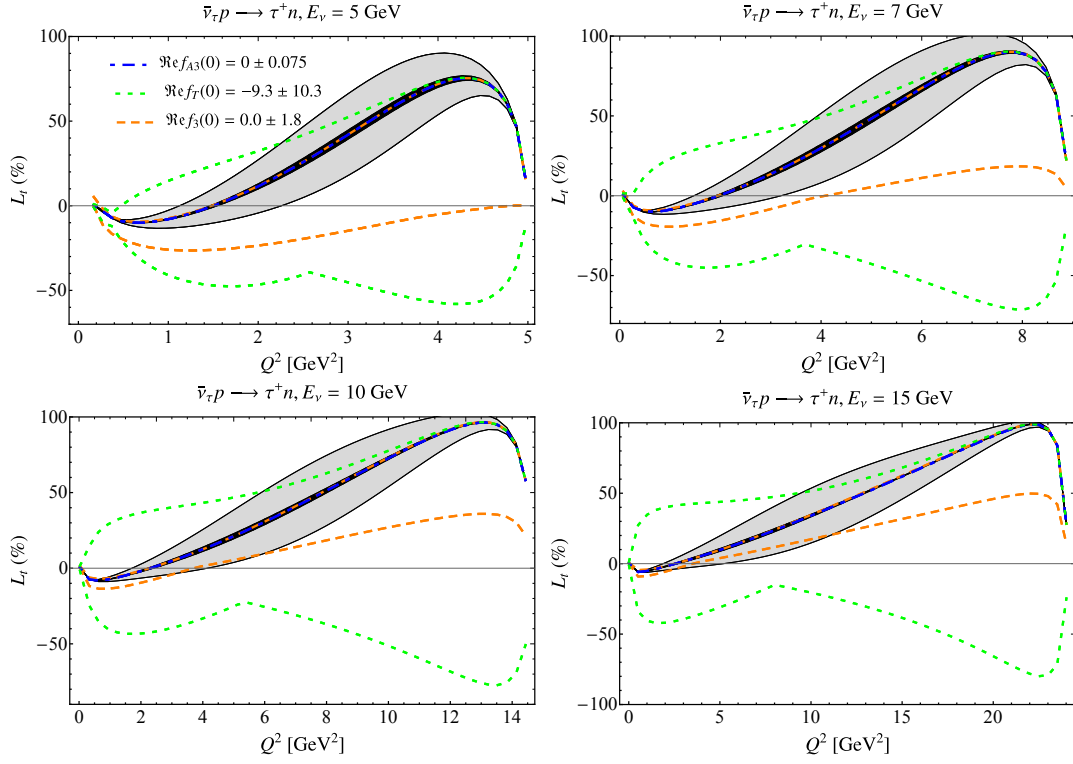


Figure 45: Same as Fig. 32 but for the transverse polarization observable L_t .

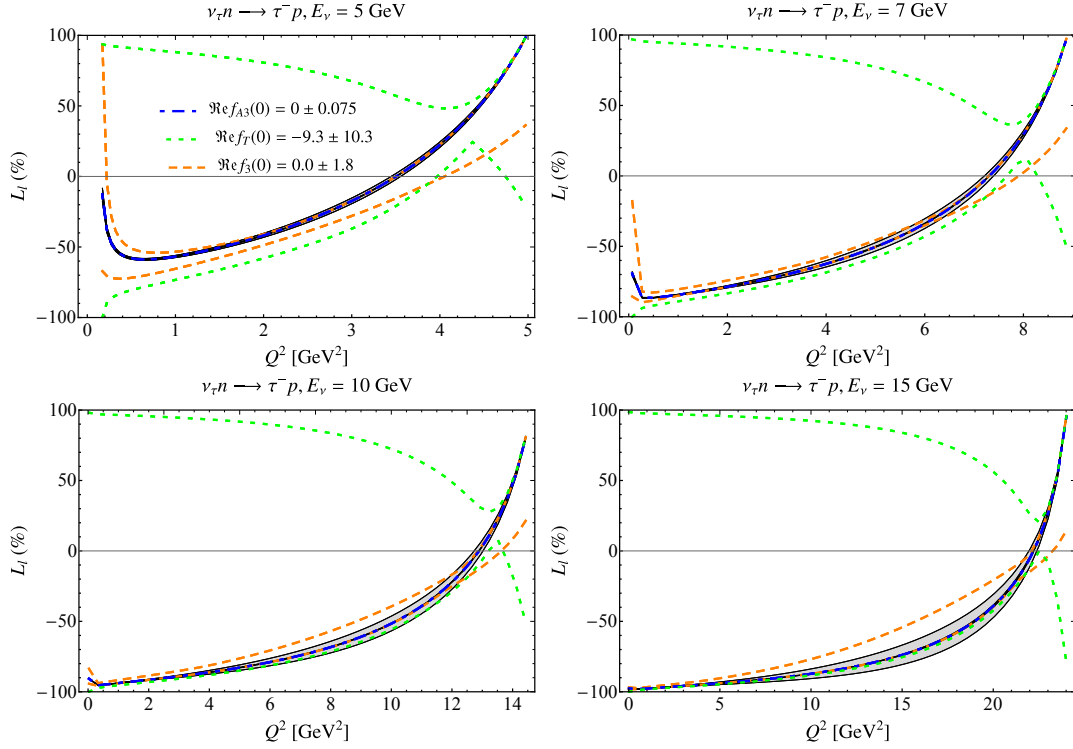


Figure 46: Same as Fig. 32 but for the longitudinal polarization observable L_l .

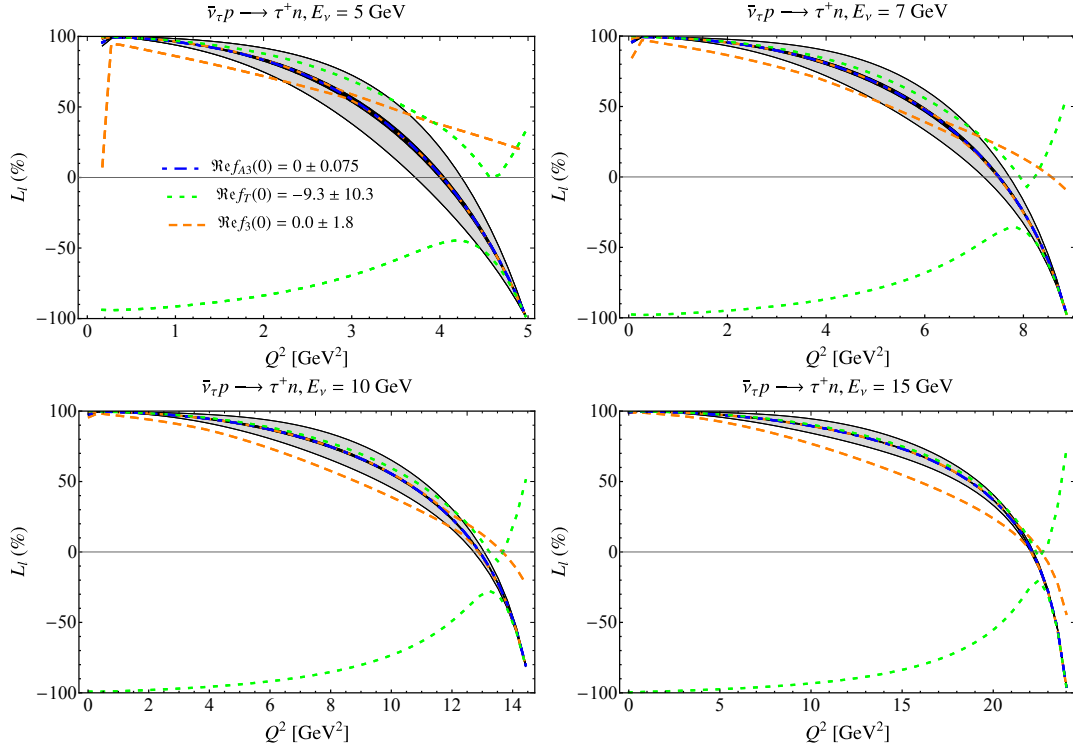


Figure 47: Same as Fig. 33 but for the longitudinal polarization observable L_l .

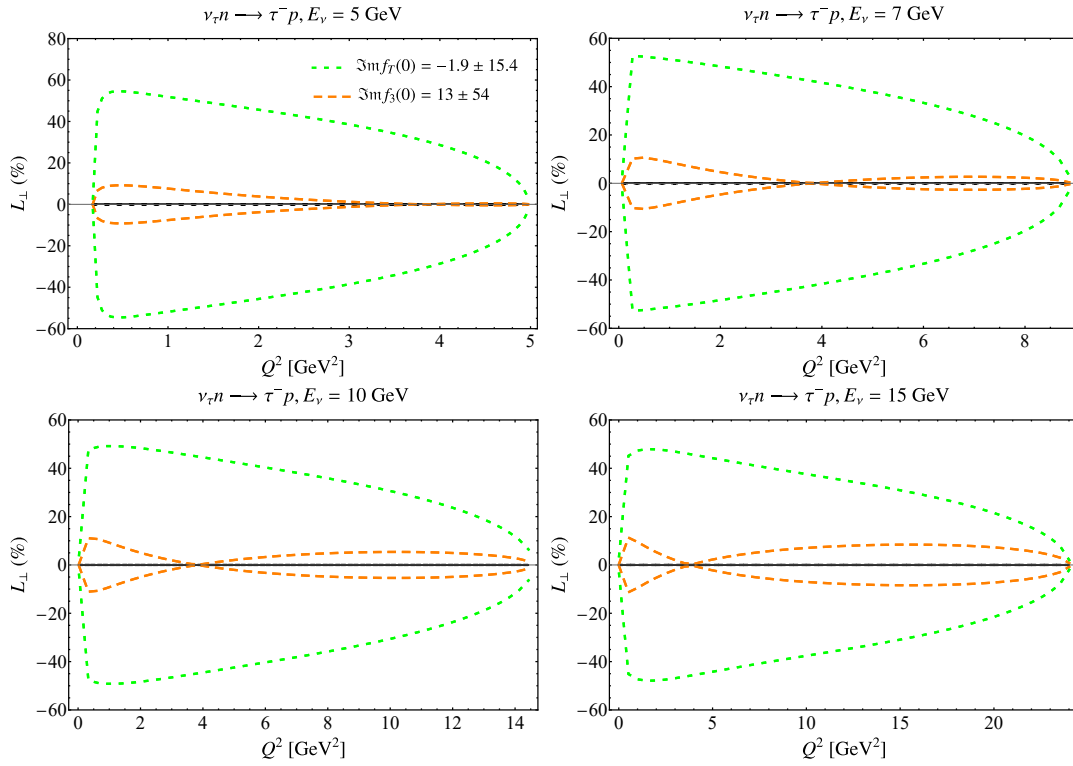


Figure 48: Same as Fig. 32 but for the transverse polarization observable L_\perp and imaginary amplitudes.

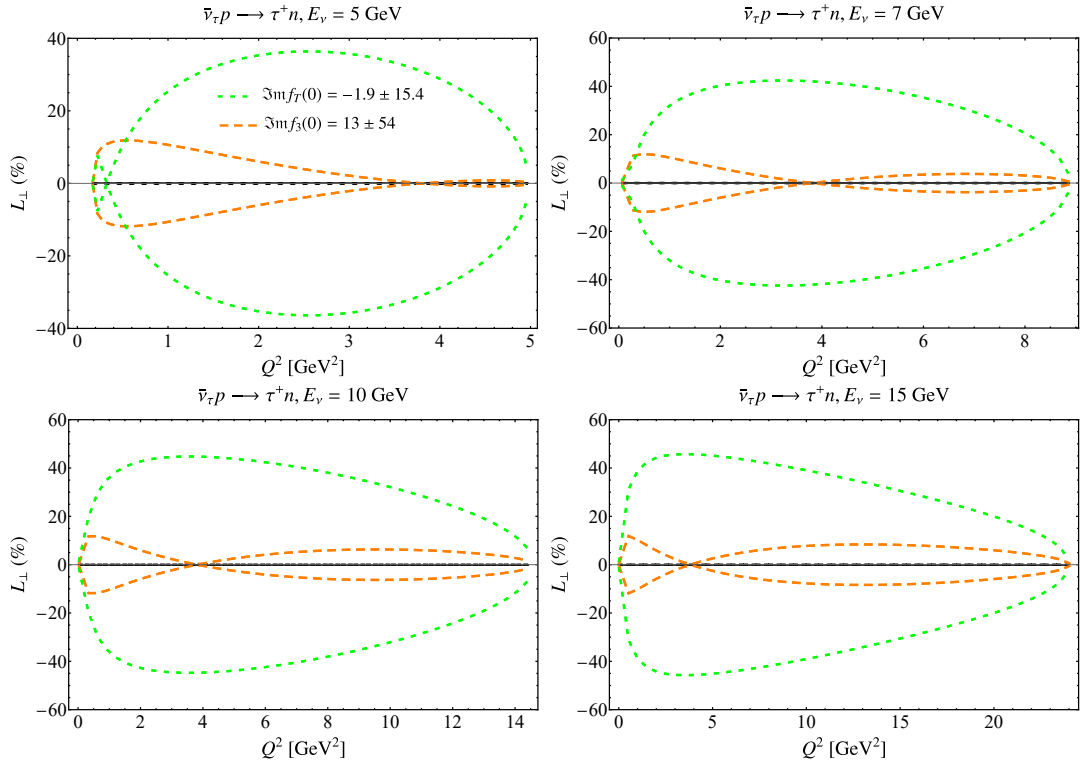


Figure 49: Same as Fig. 33 but for the transverse polarization observable L_{\perp} and imaginary amplitudes.

A.4 Radiative corrections

In this Section, we consider radiative corrections to the observables illustrated in Secs. A.1, A.2, and A.3.

A.4.1 Radiative corrections to unpolarized cross sections

In this Section, we present unpolarized cross sections including radiative corrections as described in Sec. 5. We consider muon (tau) neutrino and antineutrino energies $E_\nu = 300$ MeV, 600 MeV, 1 GeV, and 3 GeV ($E_\nu = 5$ GeV, 7 GeV, 10 GeV, and 15 GeV), and compare to the uncertainty from vector and axial-vector form factors from Sec. 4.

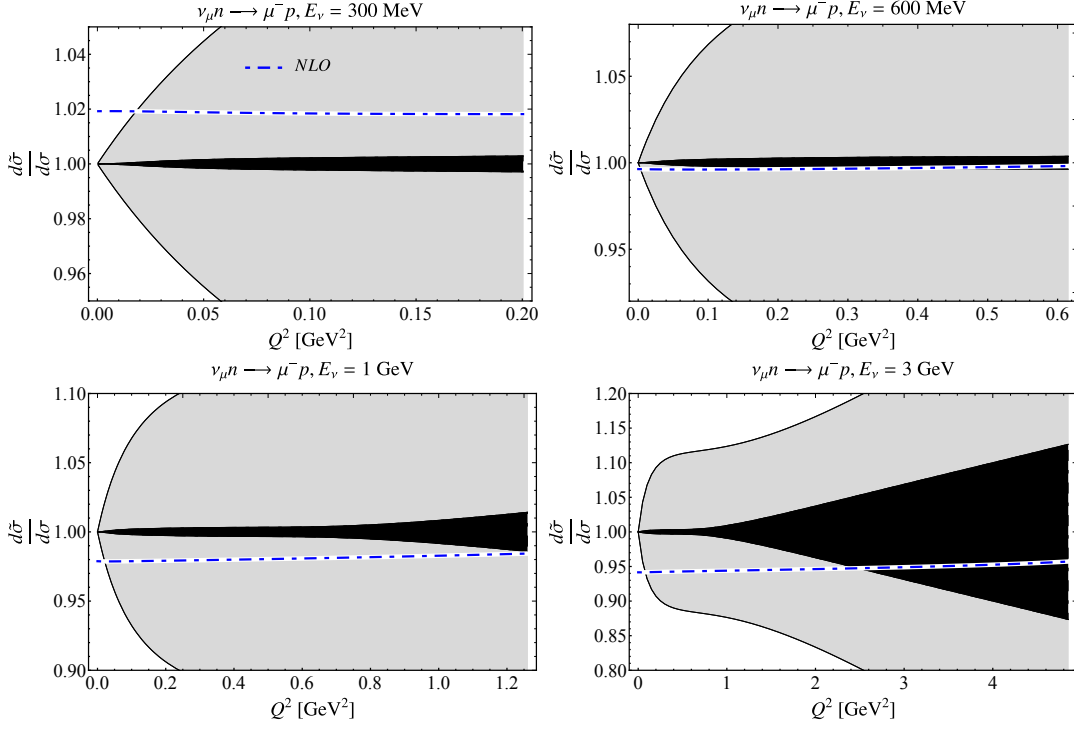


Figure 50: Ratio of the unpolarized cross section including radiative corrections to the tree-level result as a function of the squared momentum transfer Q^2 at fixed muon neutrino energies $E_\nu = 300$ MeV, 600 MeV, 1 GeV, and 3 GeV is illustrated. The radiatively-corrected cross section, which includes virtual contributions and one real photon of energy below 10 MeV, is shown by the blue dashed-dotted line. The dark black and light gray bands correspond to vector and axial-vector form factor uncertainty.

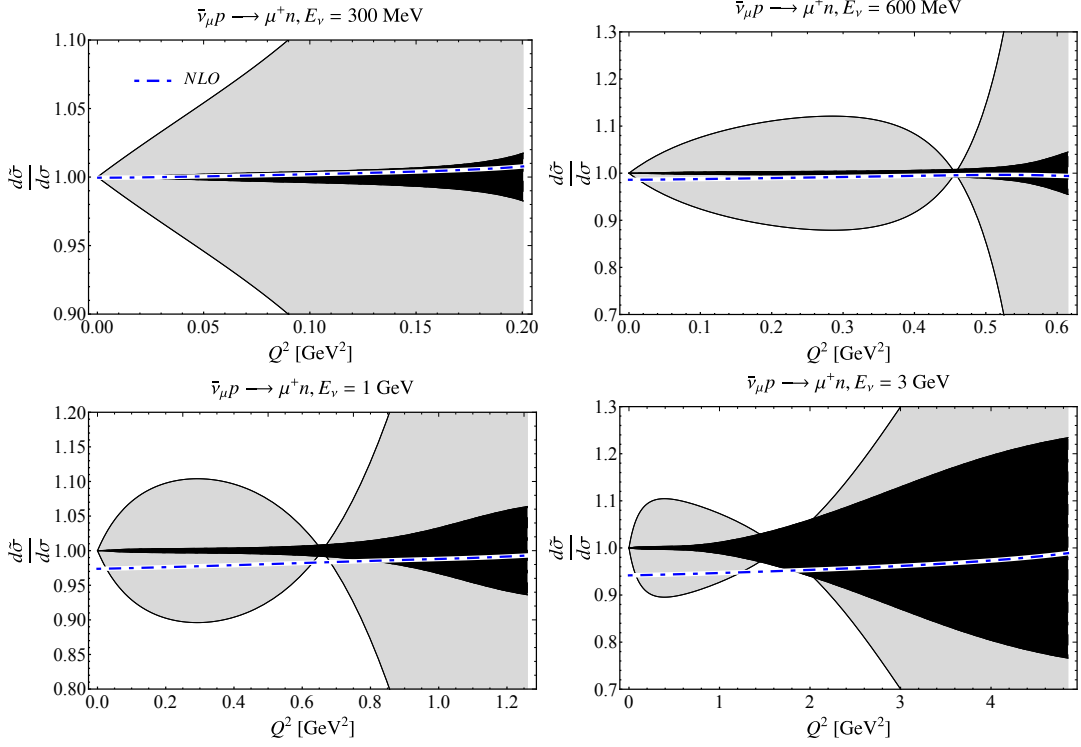


Figure 51: Same as Fig. 50 but for antineutrinos.

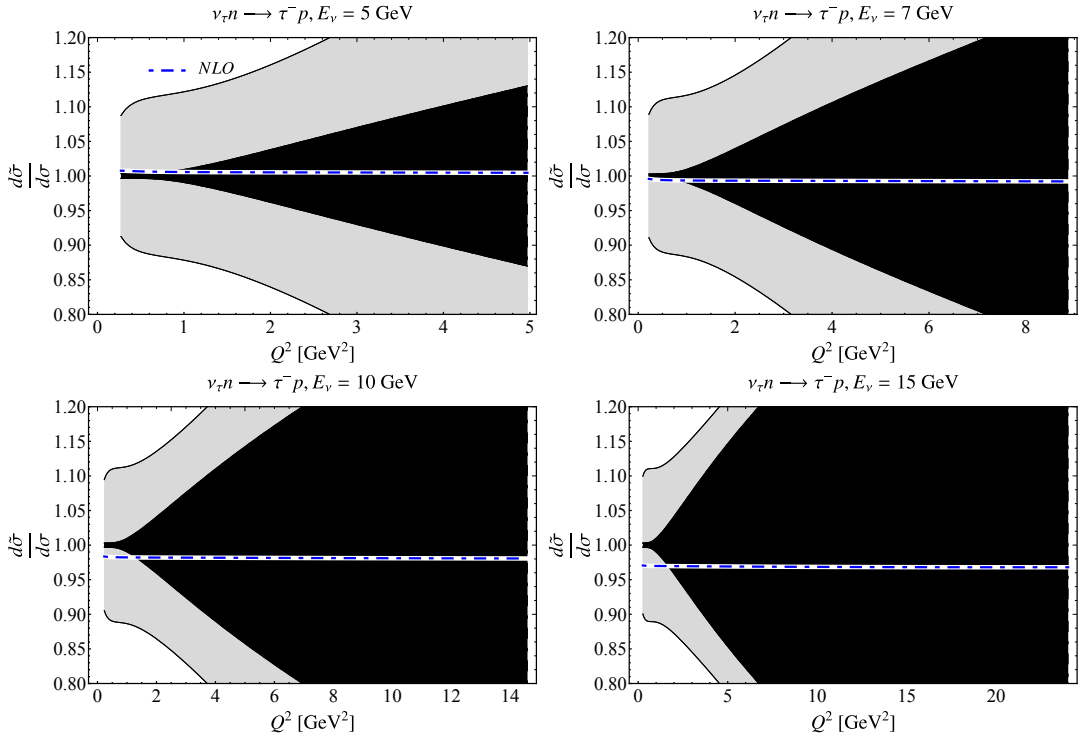


Figure 52: Same as Fig. 50 but for tau neutrinos at fixed beam energies $E_\nu = 5$ GeV, 7 GeV, 10 GeV, and 15 GeV.

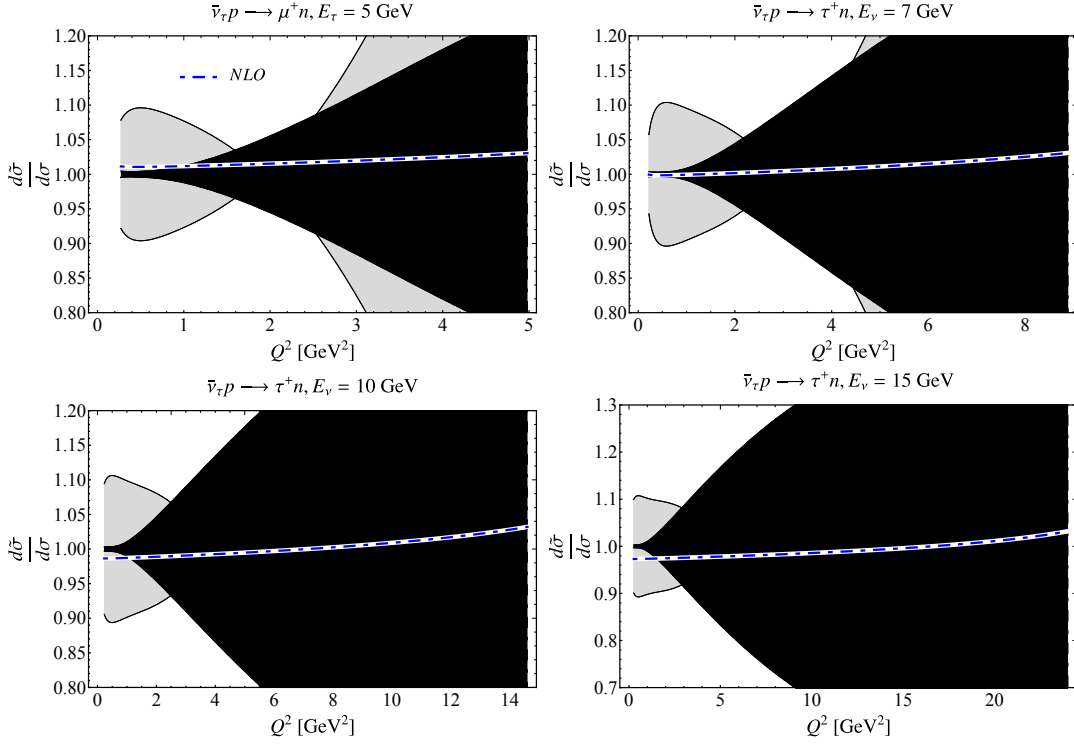


Figure 53: Same as Fig. 52 but for antineutrinos.

A.4.2 Radiative corrections to polarization asymmetries, muon (anti)neutrino

In this Section, we present single-spin asymmetries for muon neutrinos and antineutrinos, including radiative corrections as described in Sec. 5. We consider neutrino energies $E_\nu = 300$ MeV, 600 MeV, 1 GeV, and 3 GeV, and compare to the uncertainty from vector and axial-vector form factors from Sec. 4.

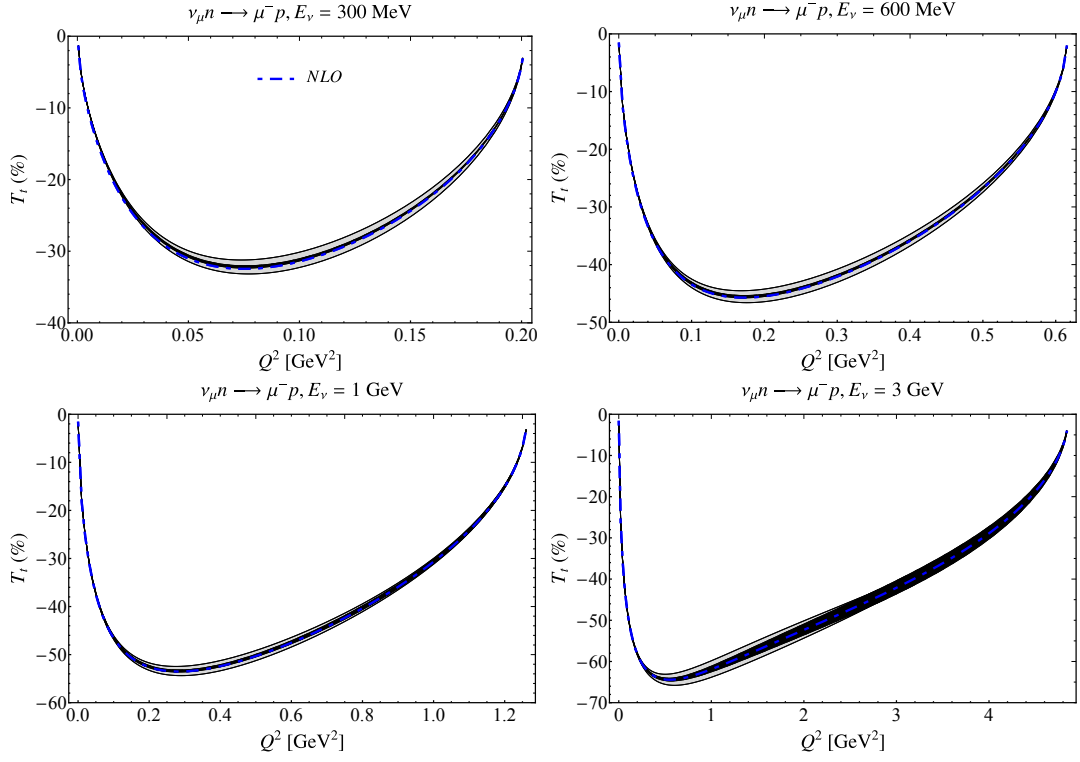


Figure 54: Radiative correction to the transverse polarization observable T_t , at fixed muon neutrino energies $E_\nu = 300$ MeV, 600 MeV, 1 GeV, and 3 GeV is illustrated. Radiatively-corrected observable, which includes virtual contributions and one real photon of energy below 10 MeV, is shown by the blue dashed-dotted line. The dark black and light gray bands correspond to vector and axial-vector form factor uncertainty.

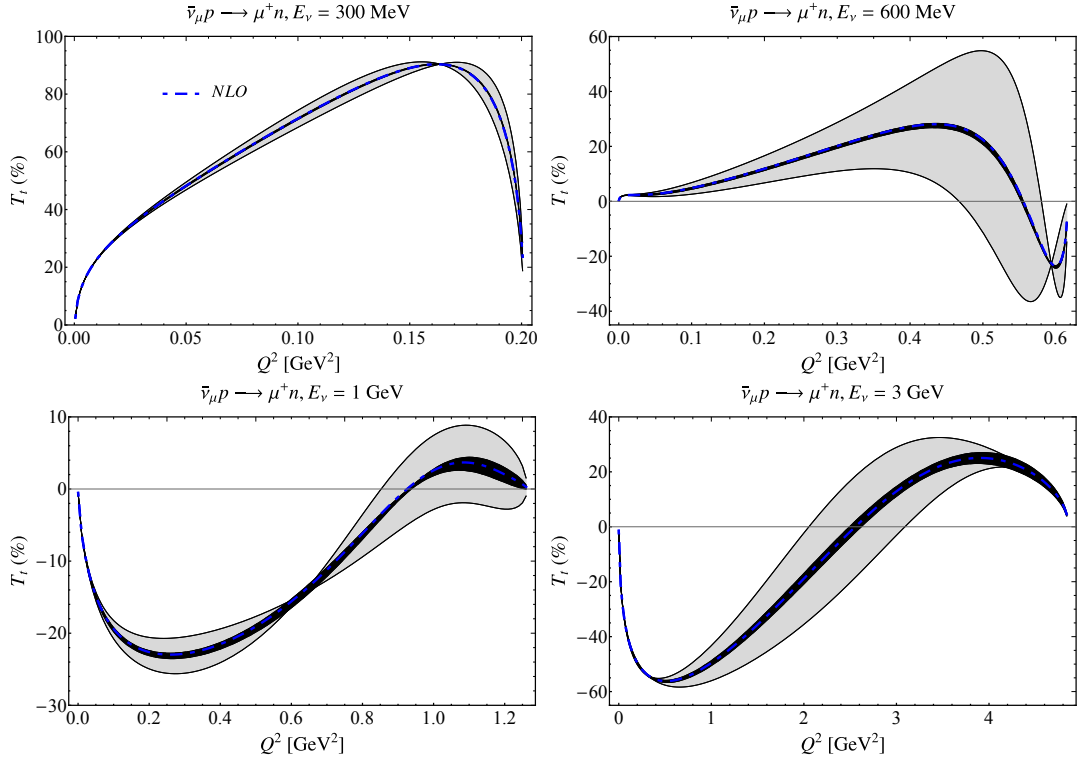


Figure 55: Same as Fig. 54 but for antineutrinos.

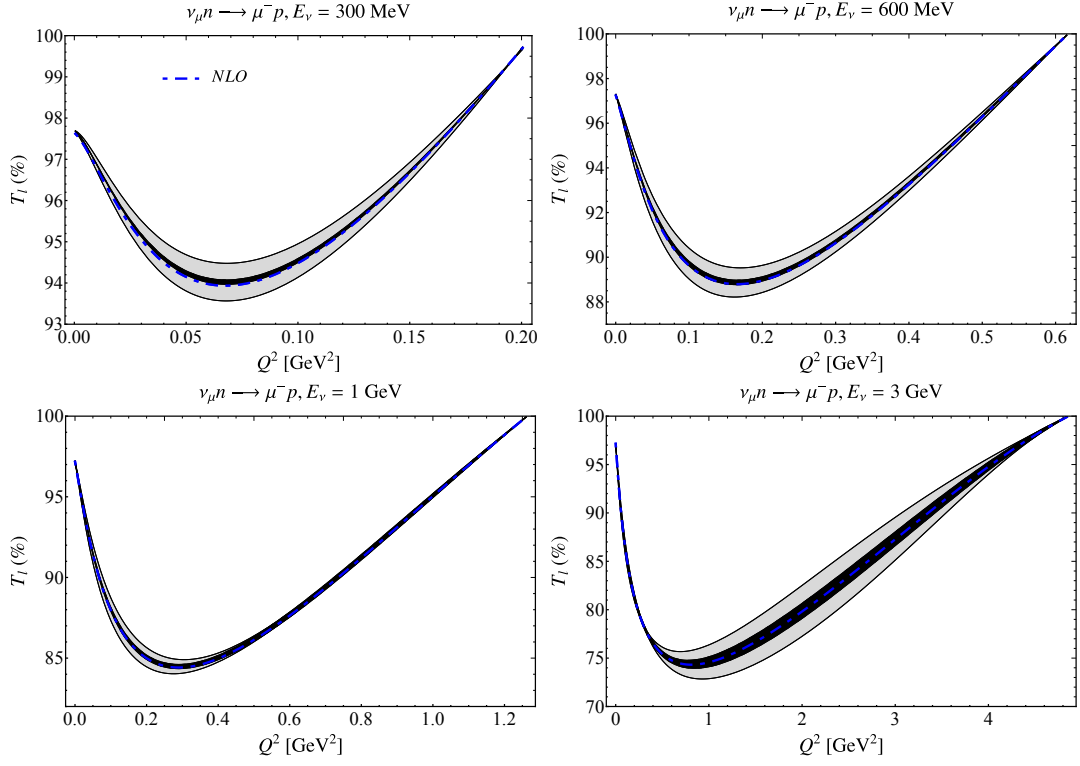


Figure 56: Same as Fig. 54 but for the longitudinal polarization observable T_l .

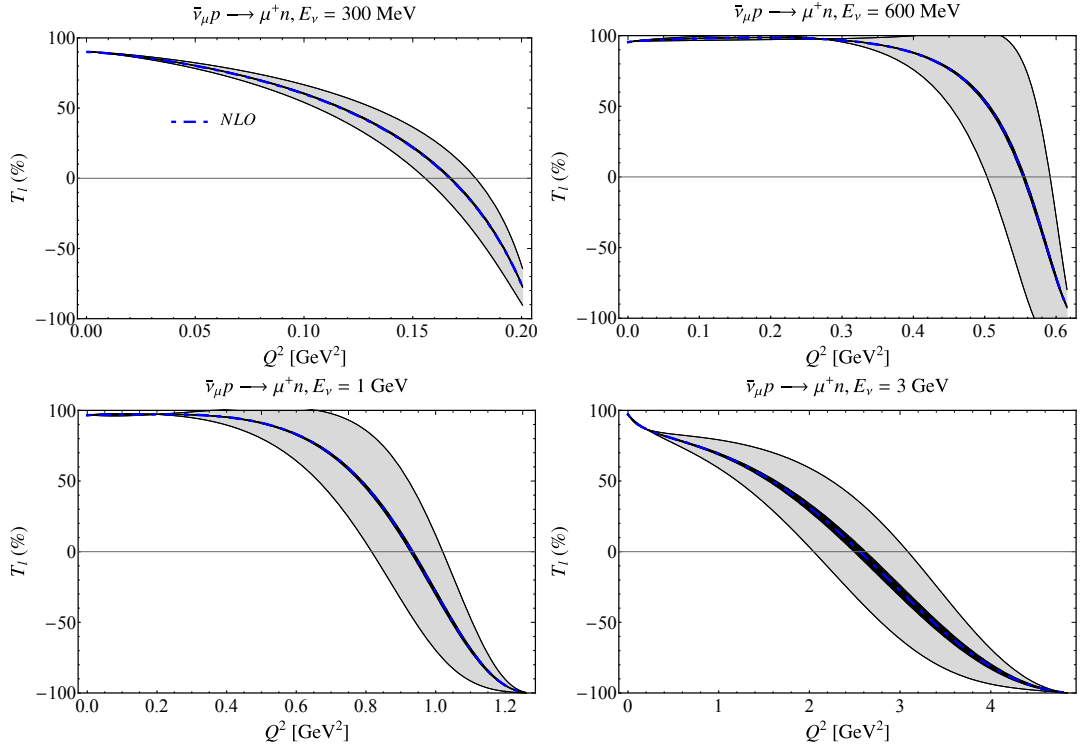


Figure 57: Same as Fig. 55 but for the longitudinal polarization observable T_l .

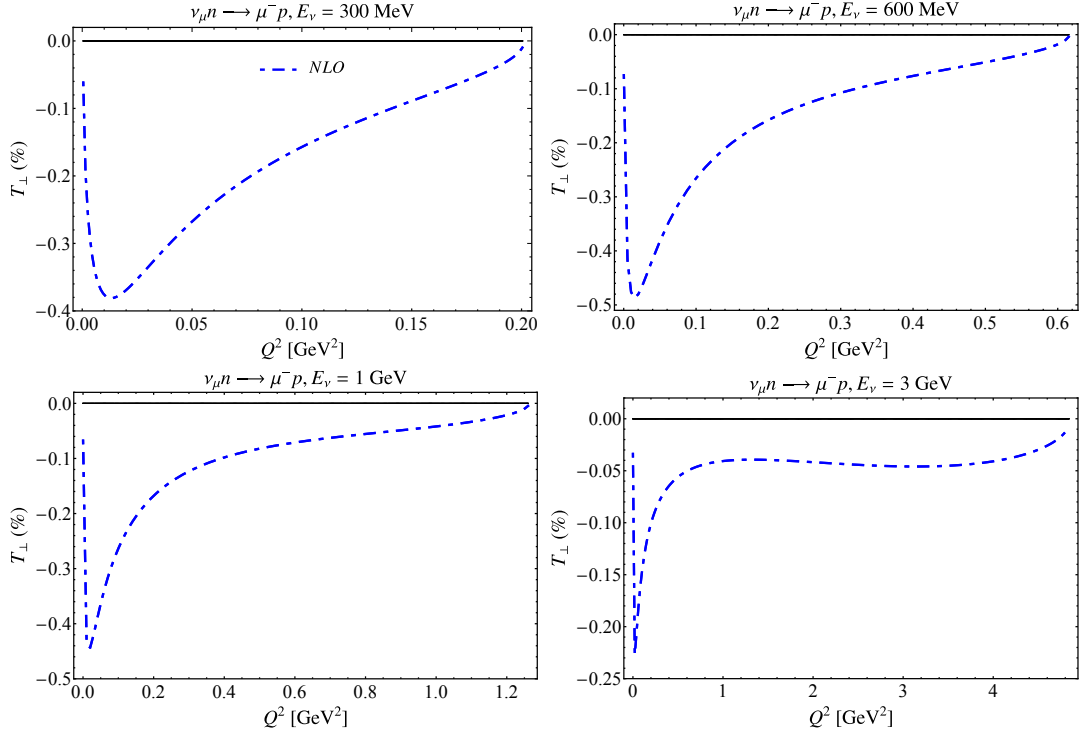


Figure 58: Same as Fig. 54 but for the transverse polarization observable T_{\perp} .

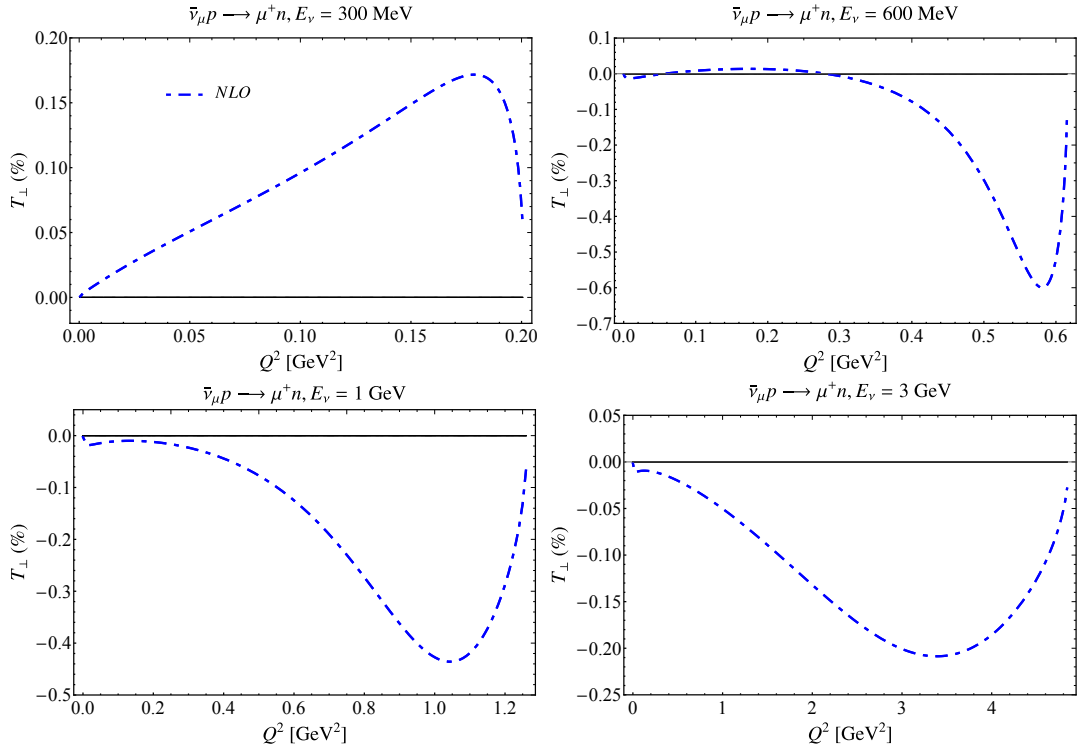


Figure 59: Same as Fig. 55 but for the transverse polarization observable T_{\perp} .

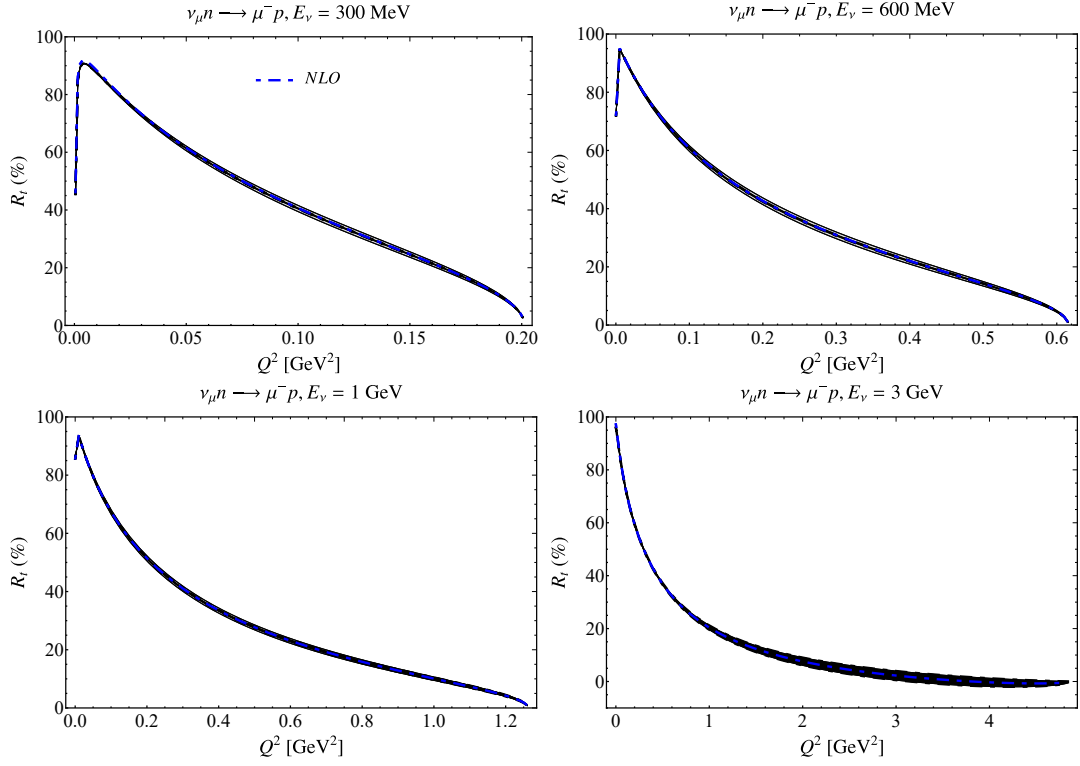


Figure 60: Same as Fig. 54 but for the transverse polarization observable R_t .

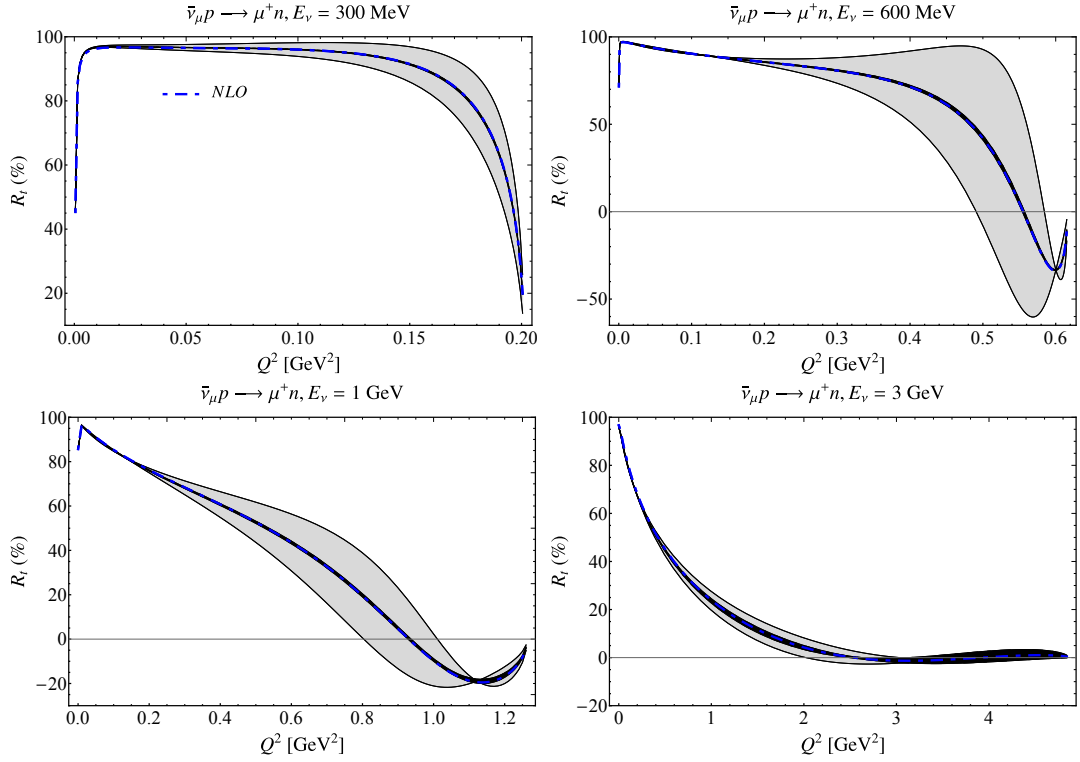


Figure 61: Same as Fig. 55 but for the transverse polarization observable R_t .

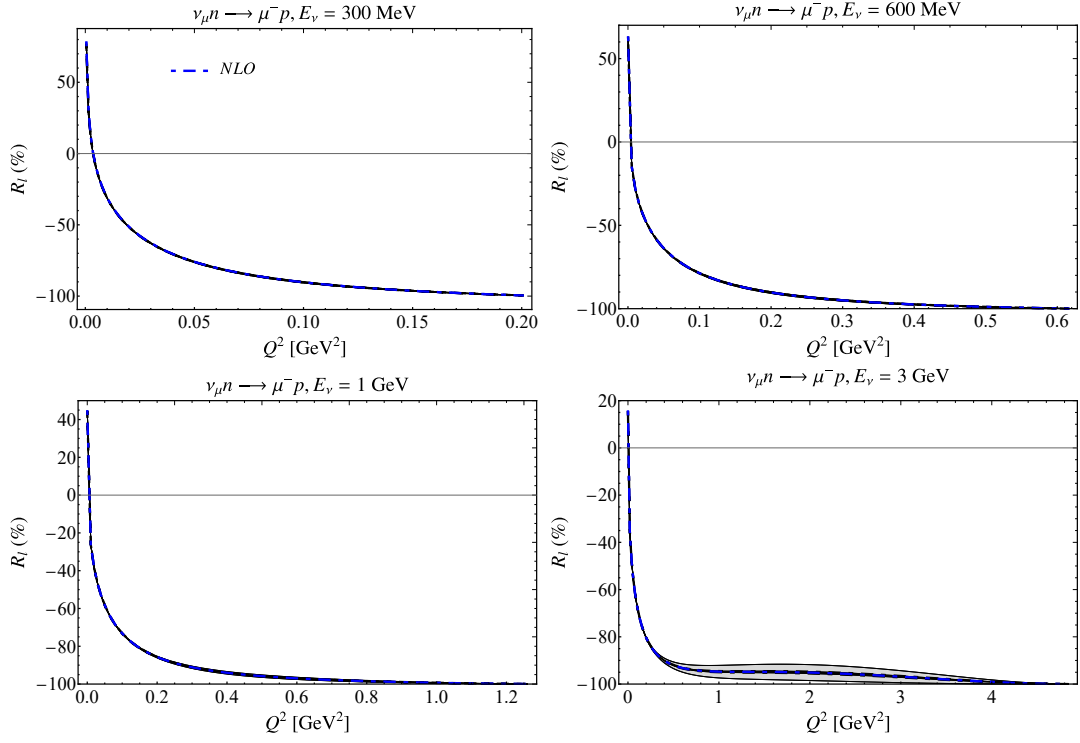


Figure 62: Same as Fig. 54 but for the longitudinal polarization observable R_l .

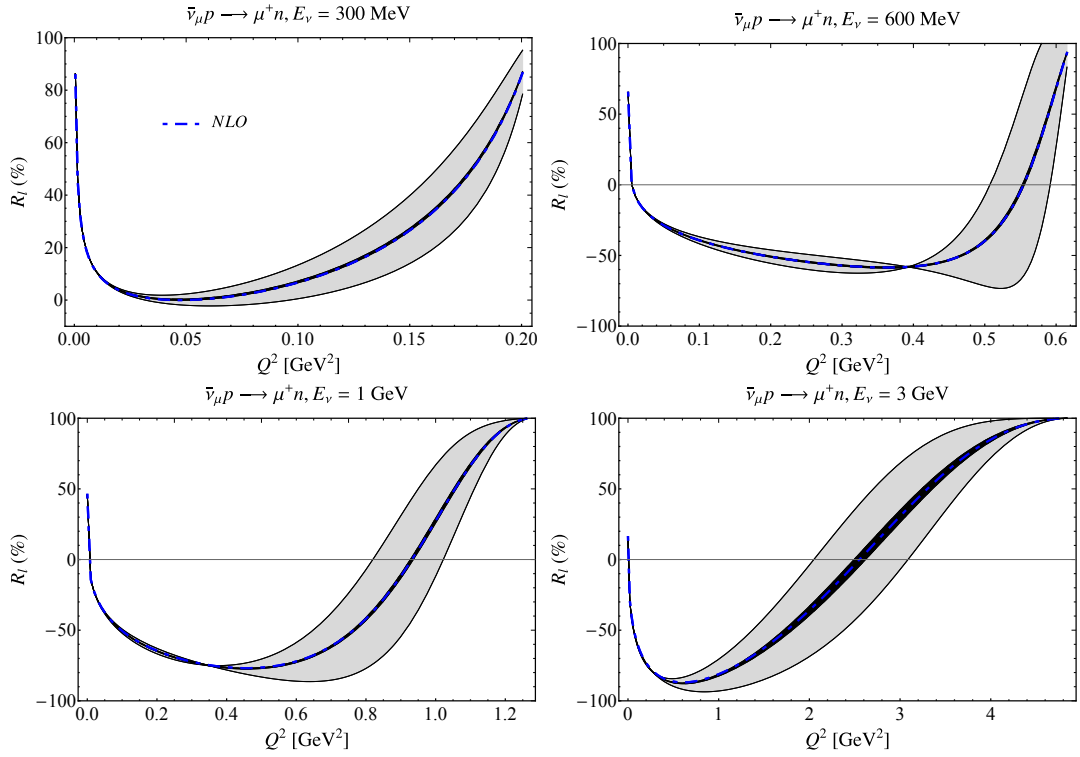


Figure 63: Same as Fig. 55 but for the longitudinal polarization observable R_l .

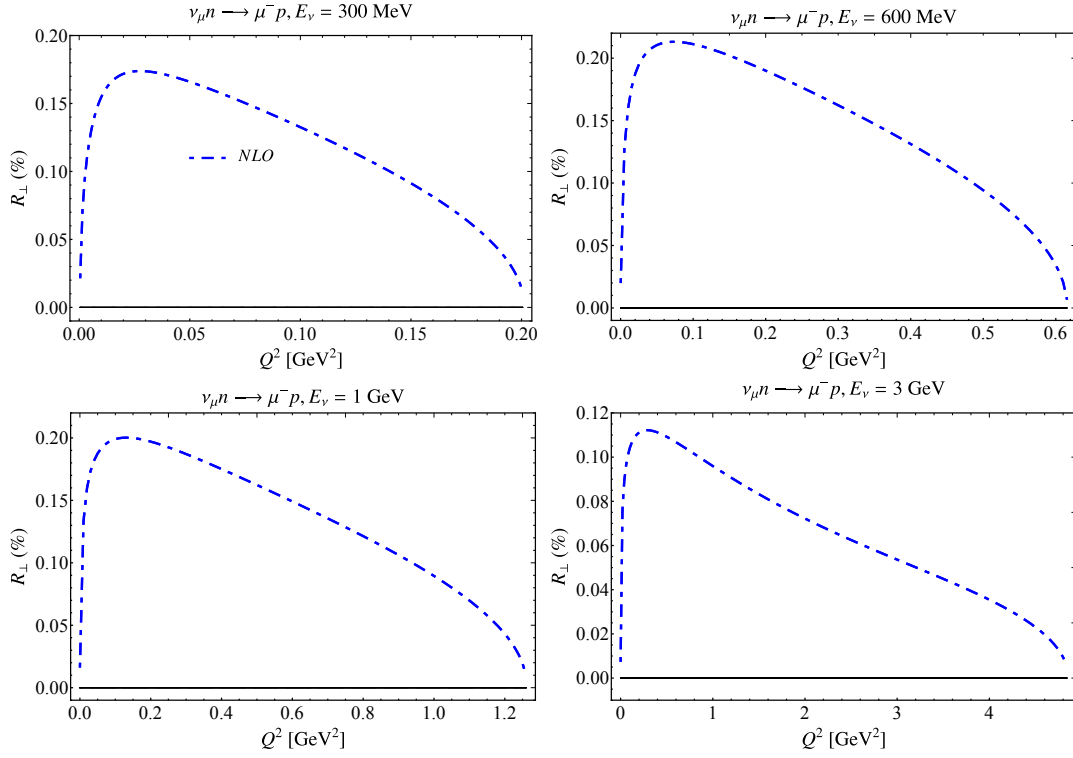


Figure 64: Same as Fig. 54 but for the transverse polarization observable R_{\perp} .

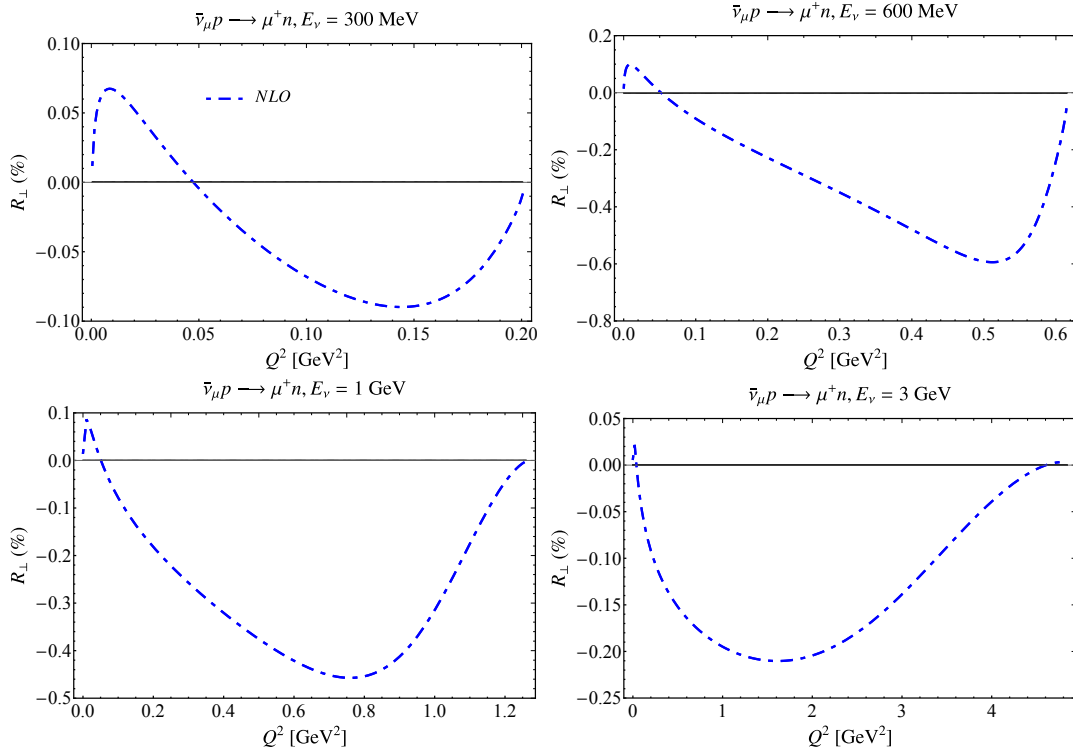


Figure 65: Same as Fig. 55 but for the transverse polarization observable R_{\perp} .

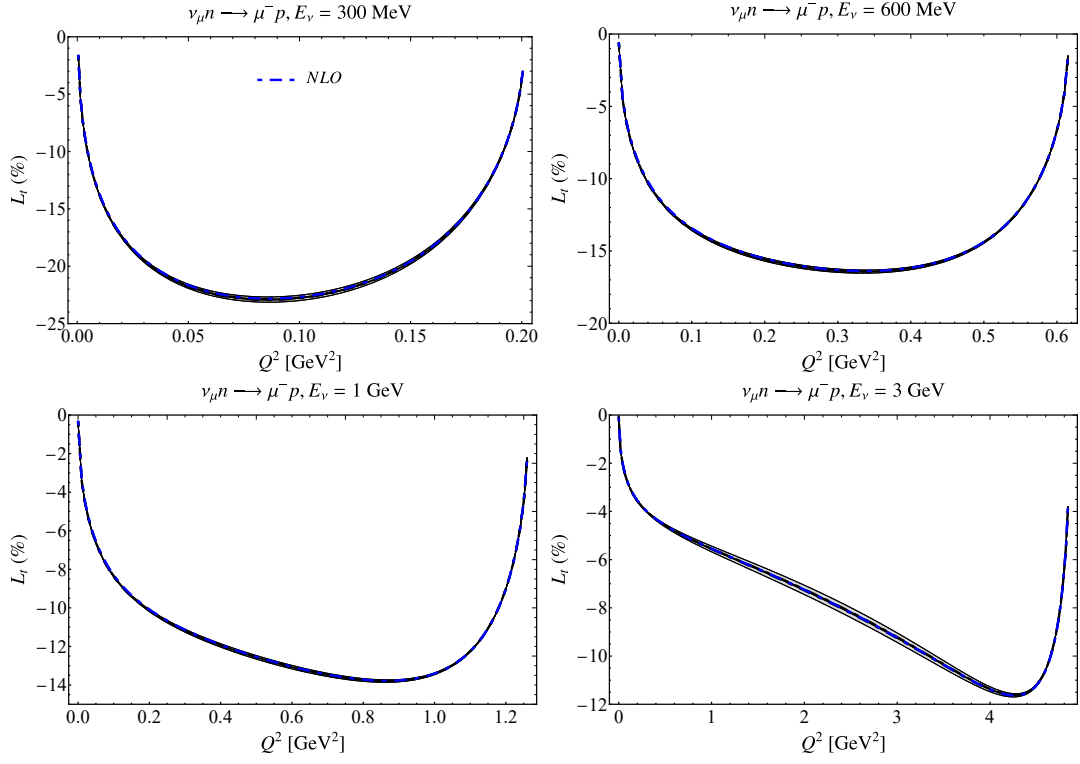


Figure 66: Same as Fig. 54 but for the transverse polarization observable L_t .

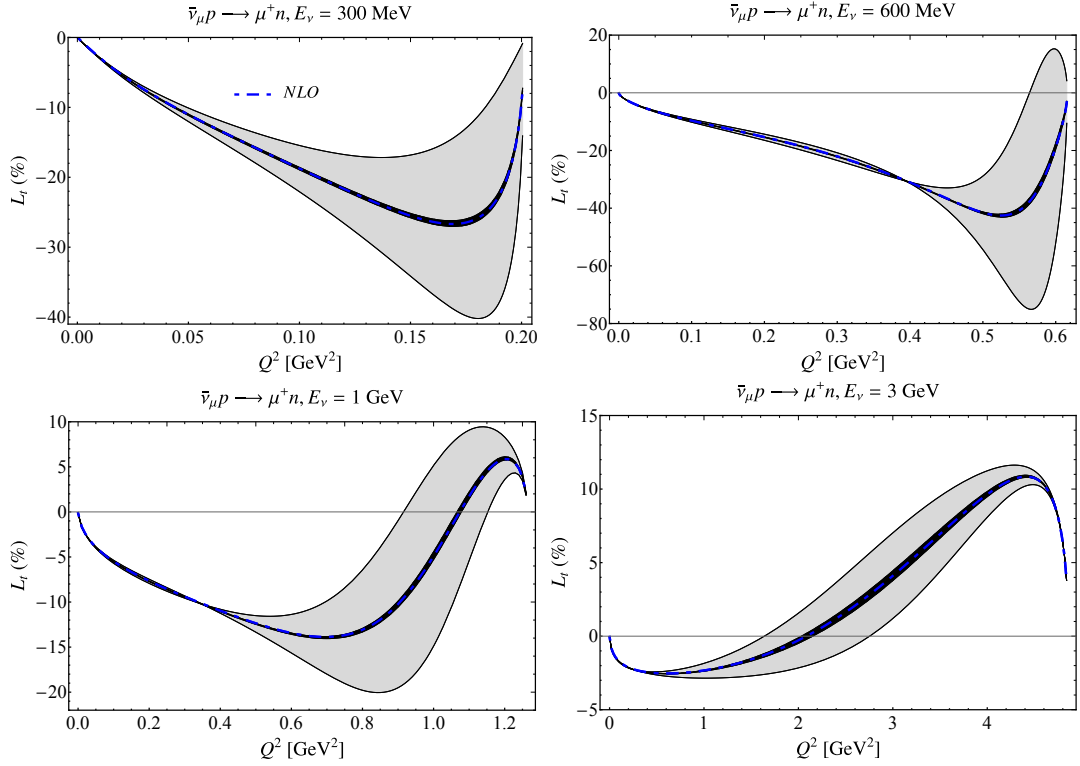


Figure 67: Same as Fig. 55 but for the transverse polarization observable L_t .

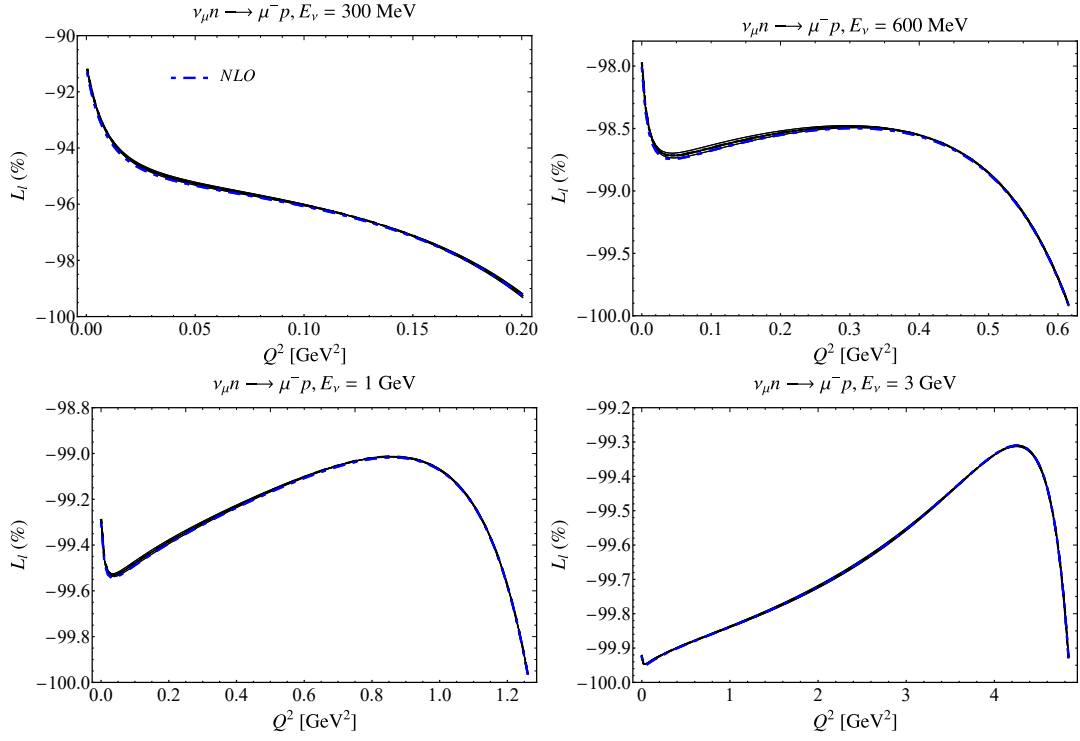


Figure 68: Same as Fig. 54 but for the longitudinal polarization observable L_L .

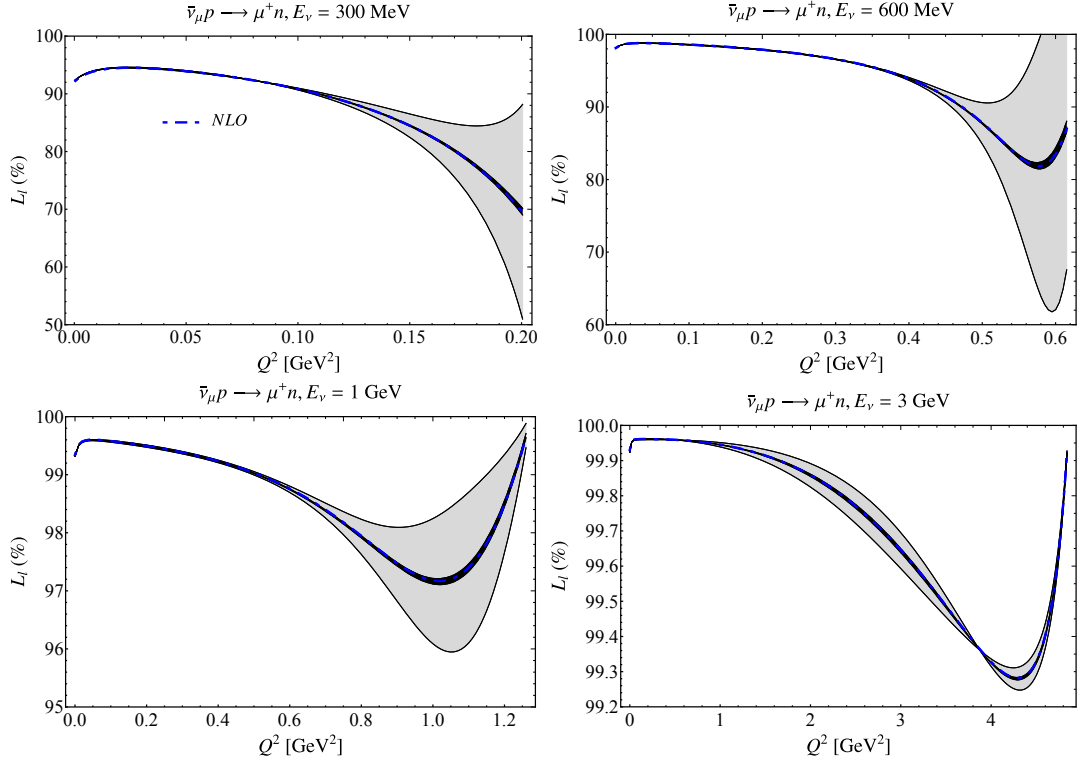


Figure 69: Same as Fig. 55 but for the longitudinal polarization observable L_L .

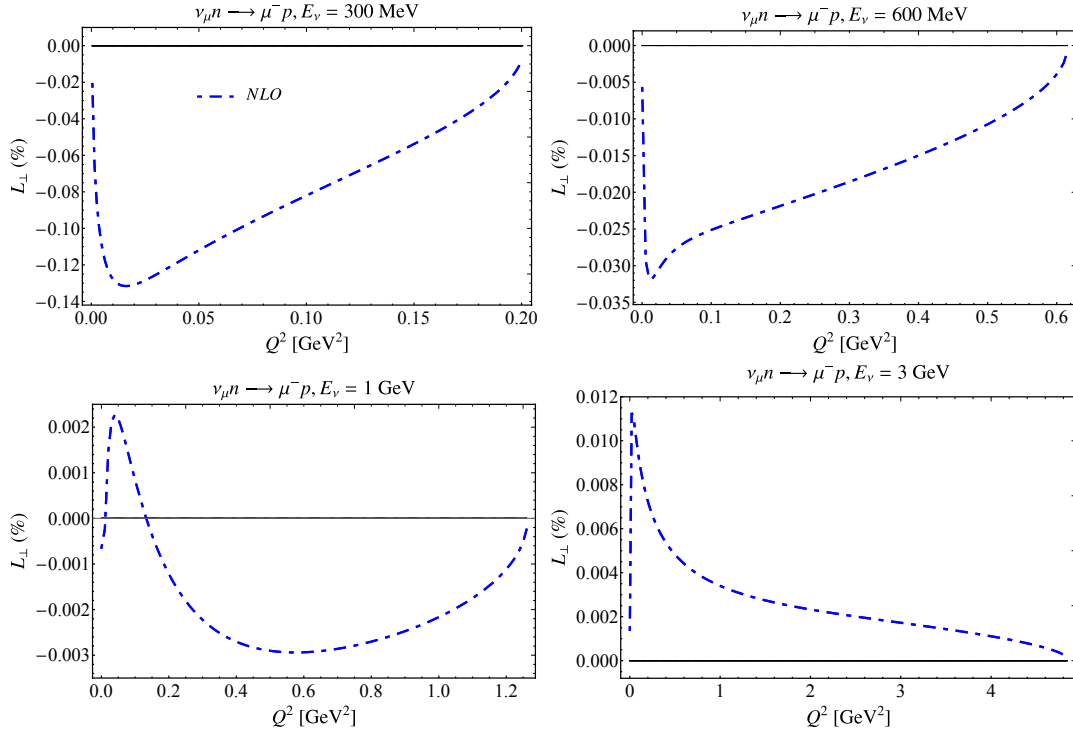


Figure 70: Same as Fig. 54 but for the transverse polarization observable L_{\perp} .

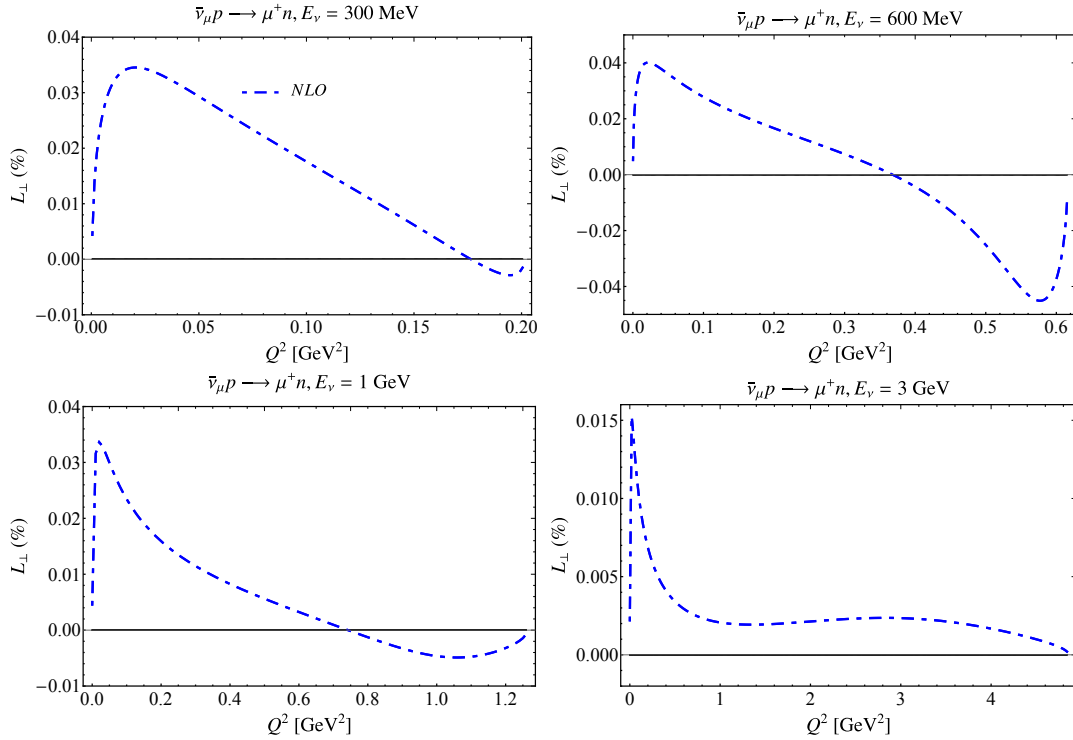


Figure 71: Same as Fig. 55 but for the transverse polarization observable L_{\perp} .

A.4.3 Radiative corrections to polarization asymmetries, tau (anti)neutrino

In this Section, we present single-spin asymmetries for tau neutrinos and antineutrinos, including radiative corrections as described in Sec. 5. We consider neutrino energies $E_\nu = 5$ GeV, 7 GeV, 10 GeV, and 15 GeV, and compare to the uncertainty from vector and axial-vector form factors from Sec. 4.

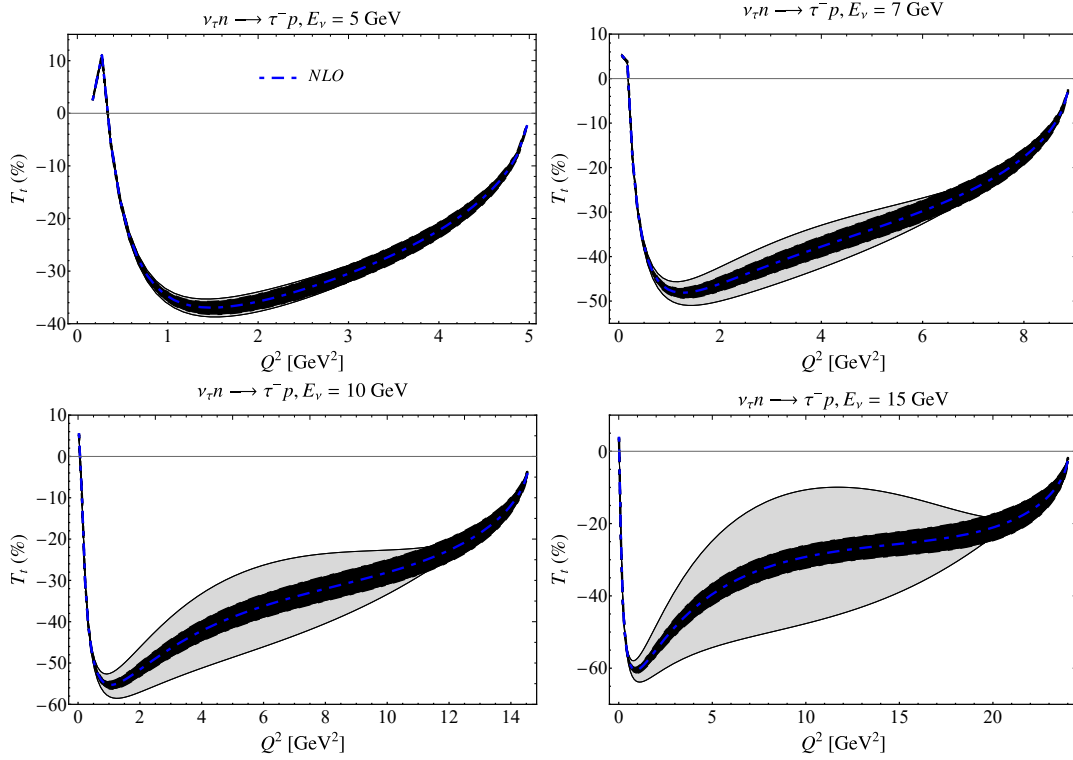


Figure 72: Radiative correction to the transverse polarization observable T_t , at fixed tau neutrino energies $E_\nu = 5$ GeV, 7 GeV, 10 GeV, and 15 GeV is illustrated. Radiatively-corrected observable, which includes virtual contributions and one real photon of energy below 10 MeV, is shown by the blue dashed-dotted line. The dark black and light gray bands correspond to vector and axial-vector form factor uncertainty.

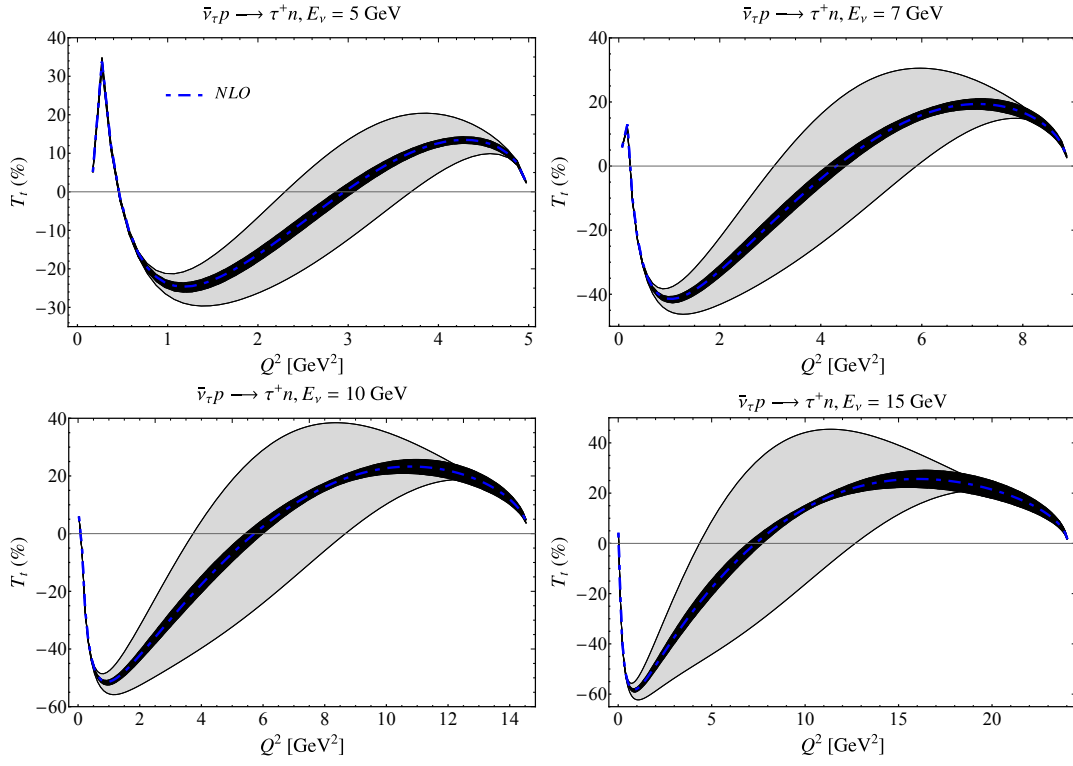


Figure 73: Same as Fig. 72 but for tau antineutrinos.

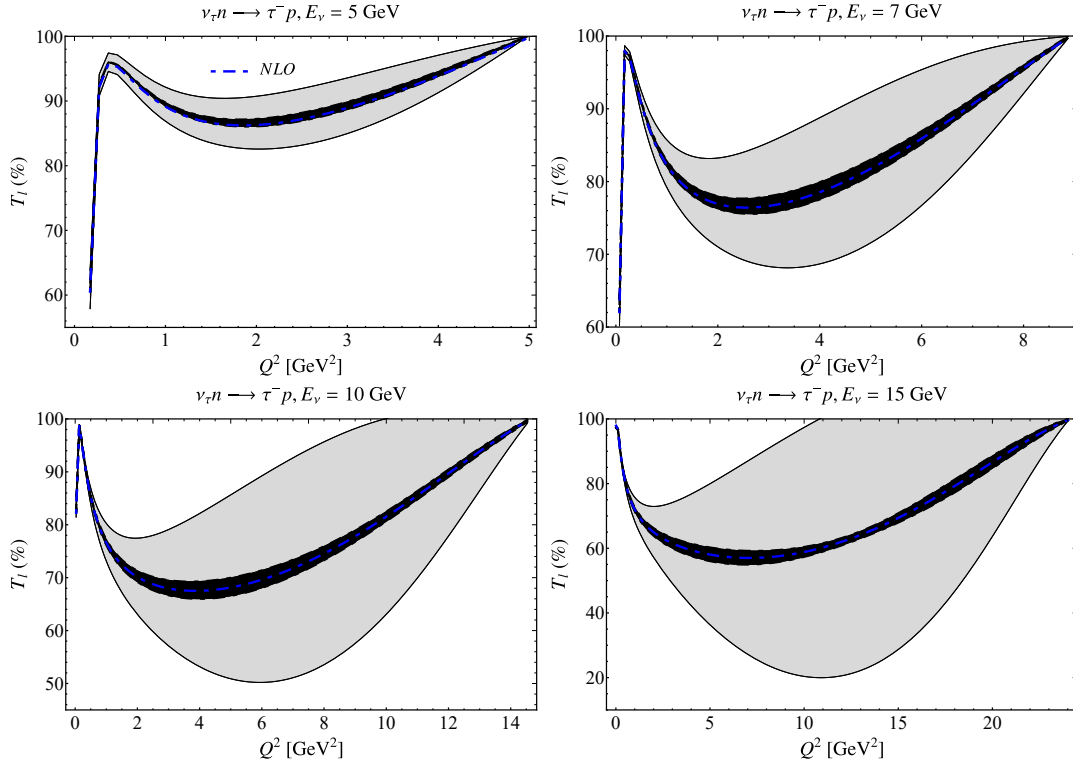


Figure 74: Same as Fig. 72 but for the longitudinal polarization observable T_l .

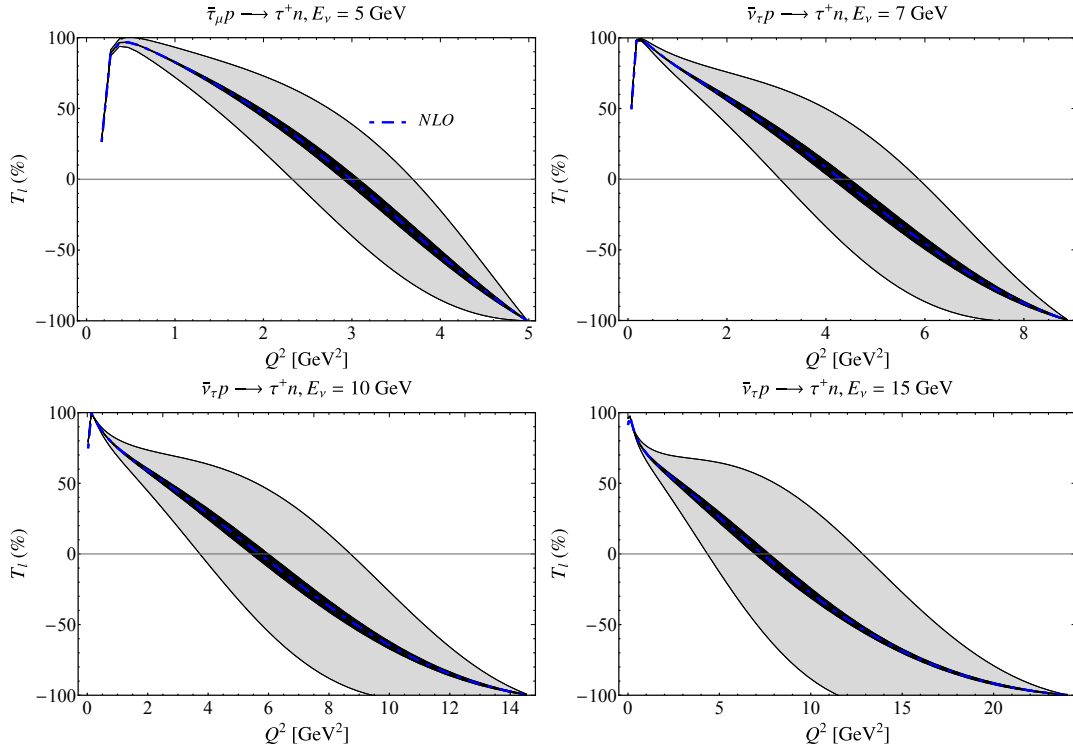


Figure 75: Same as Fig. 73 but for the longitudinal polarization observable T_L .

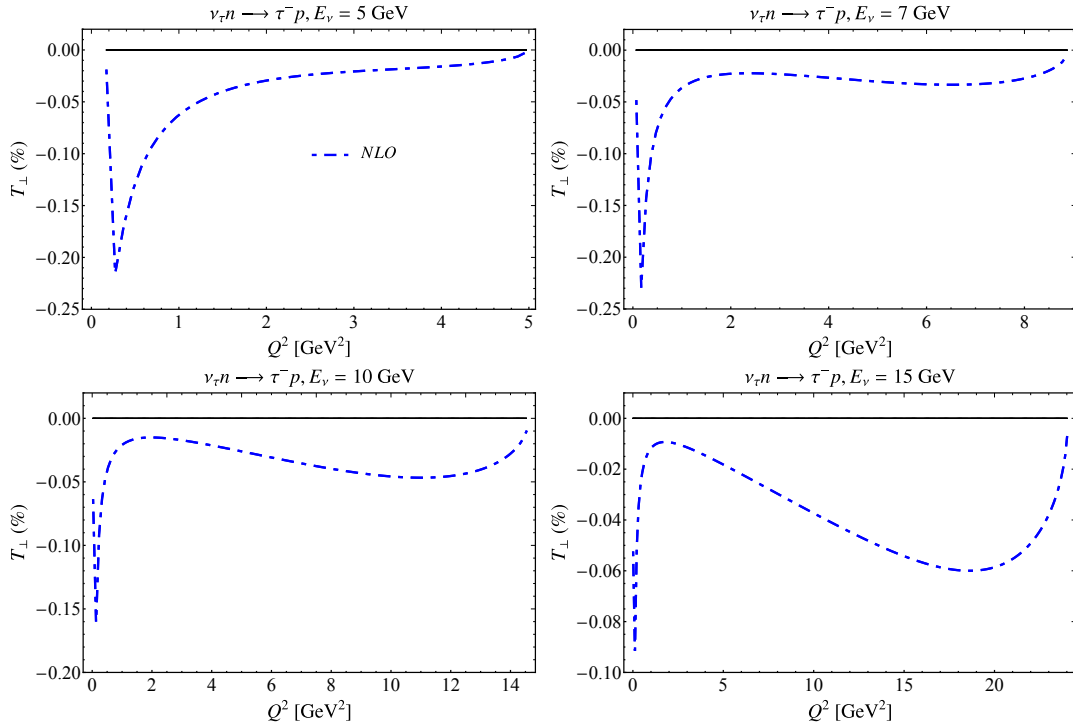


Figure 76: Same as Fig. 72 but for the transverse polarization observable T_\perp .

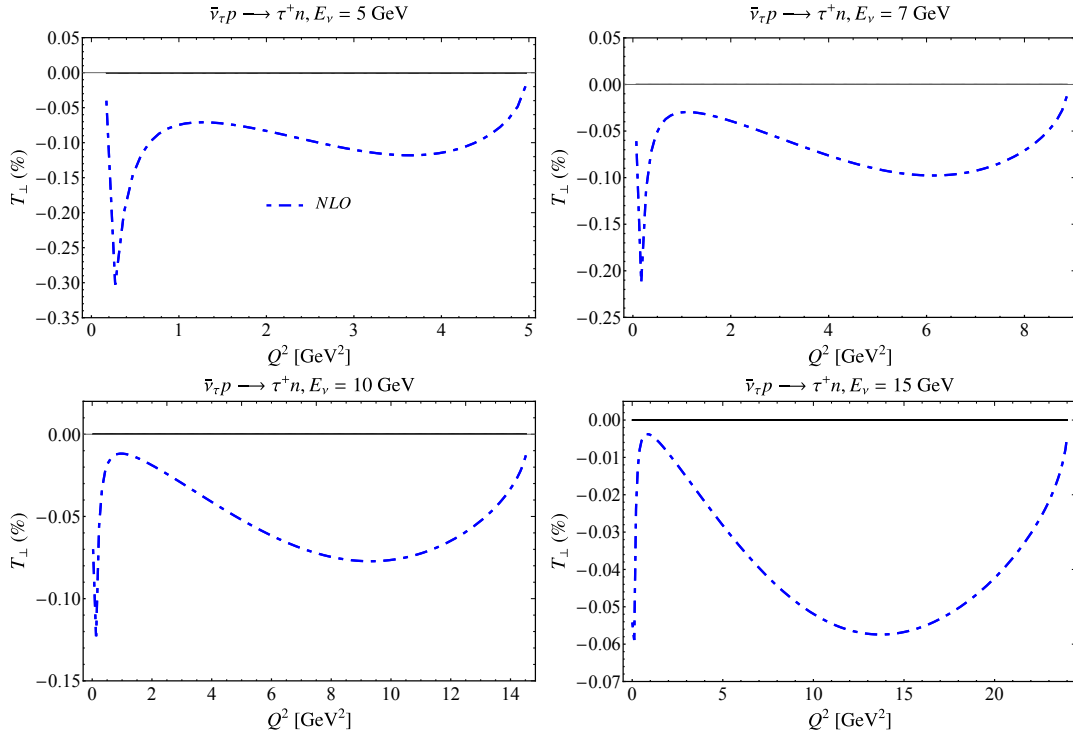


Figure 77: Same as Fig. 73 but for the transverse polarization observable T_{\perp} .

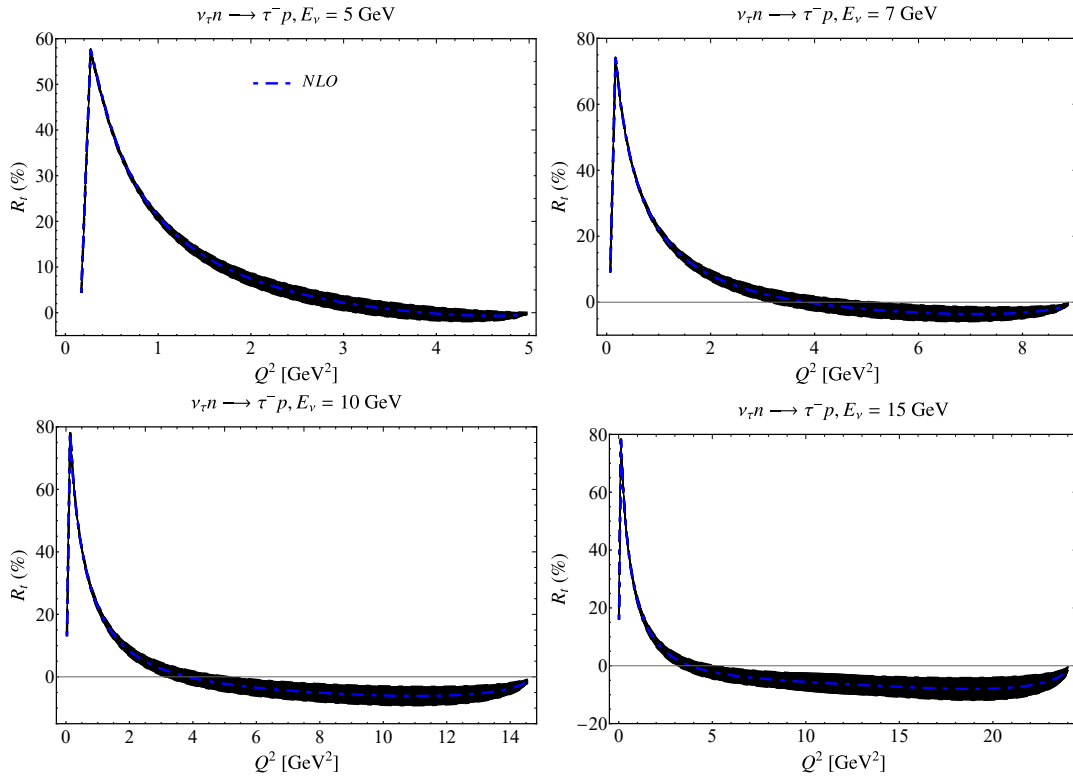


Figure 78: Same as Fig. 72 but for the transverse polarization observable R_t .

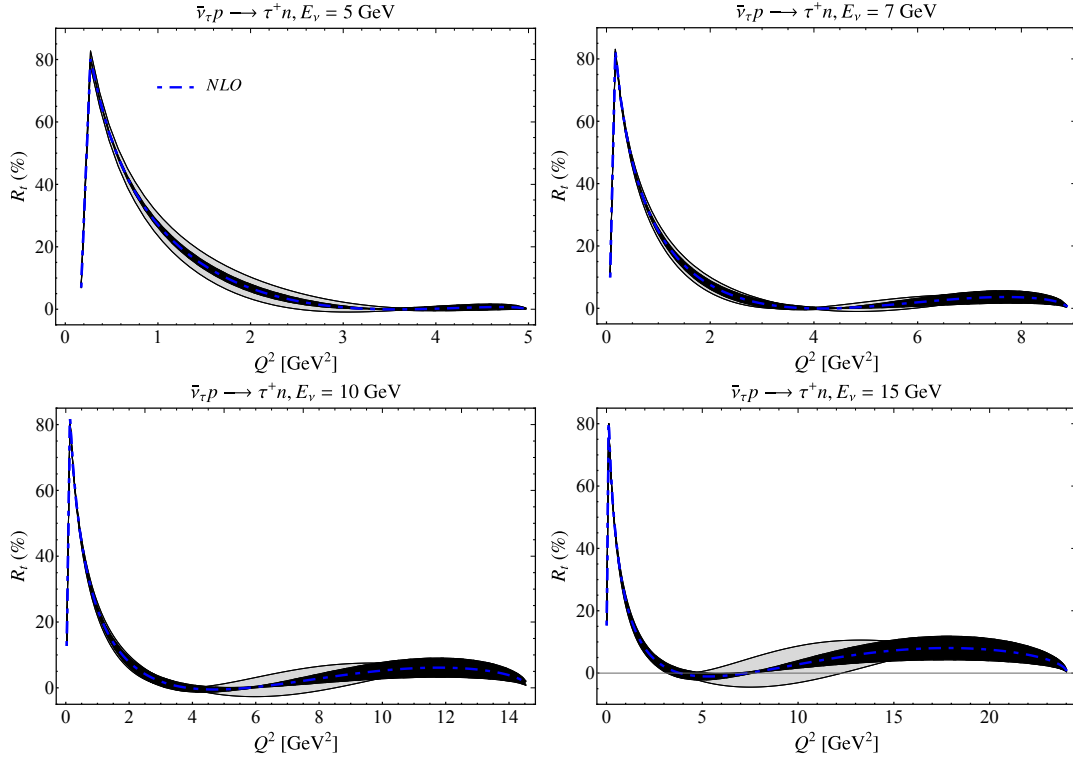


Figure 79: Same as Fig. 73 but for the transverse polarization observable R_t .

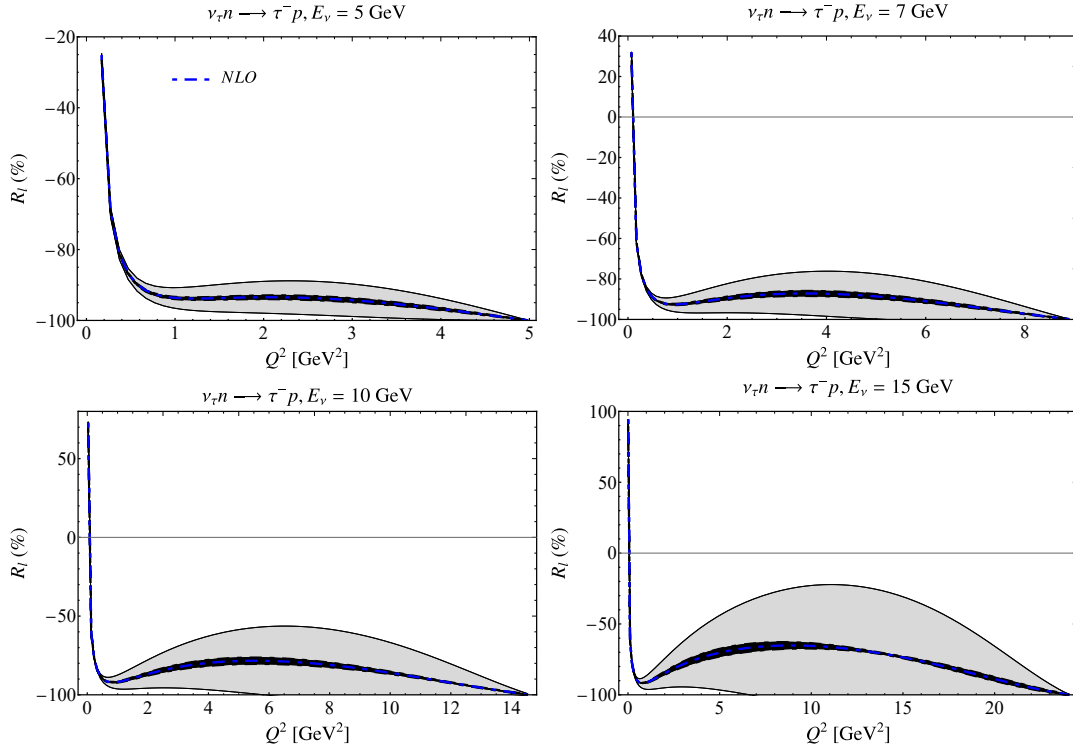


Figure 80: Same as Fig. 72 but for the longitudinal polarization observable R_l .

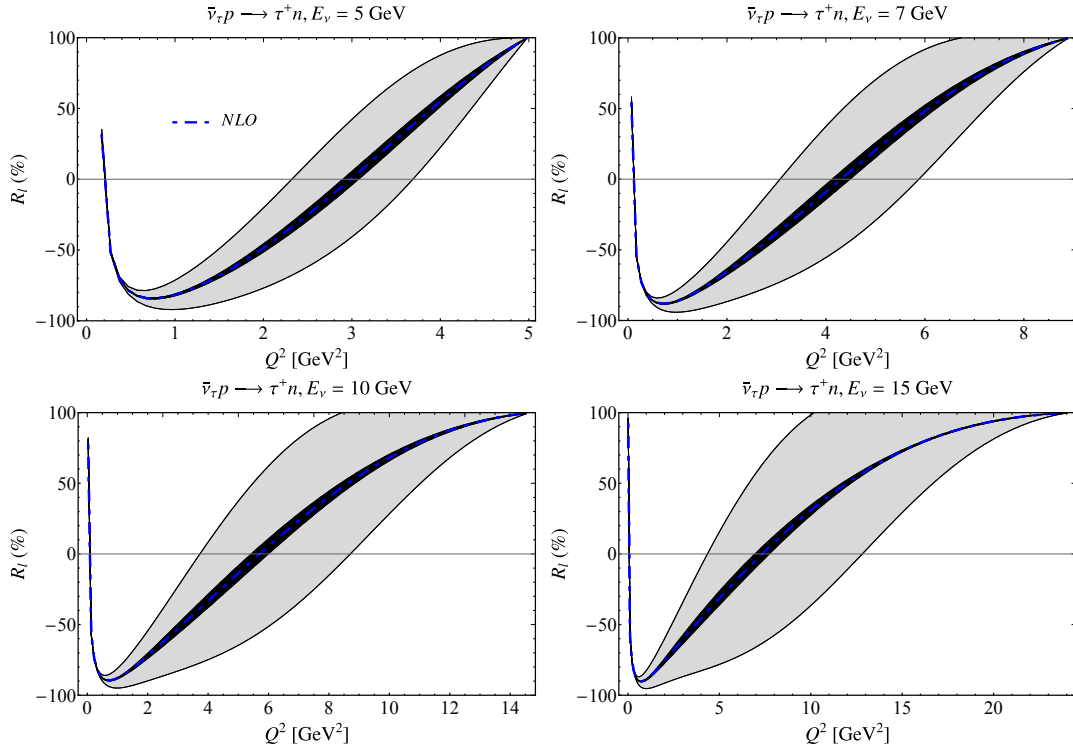


Figure 81: Same as Fig. 73 but for the longitudinal polarization observable R_l .

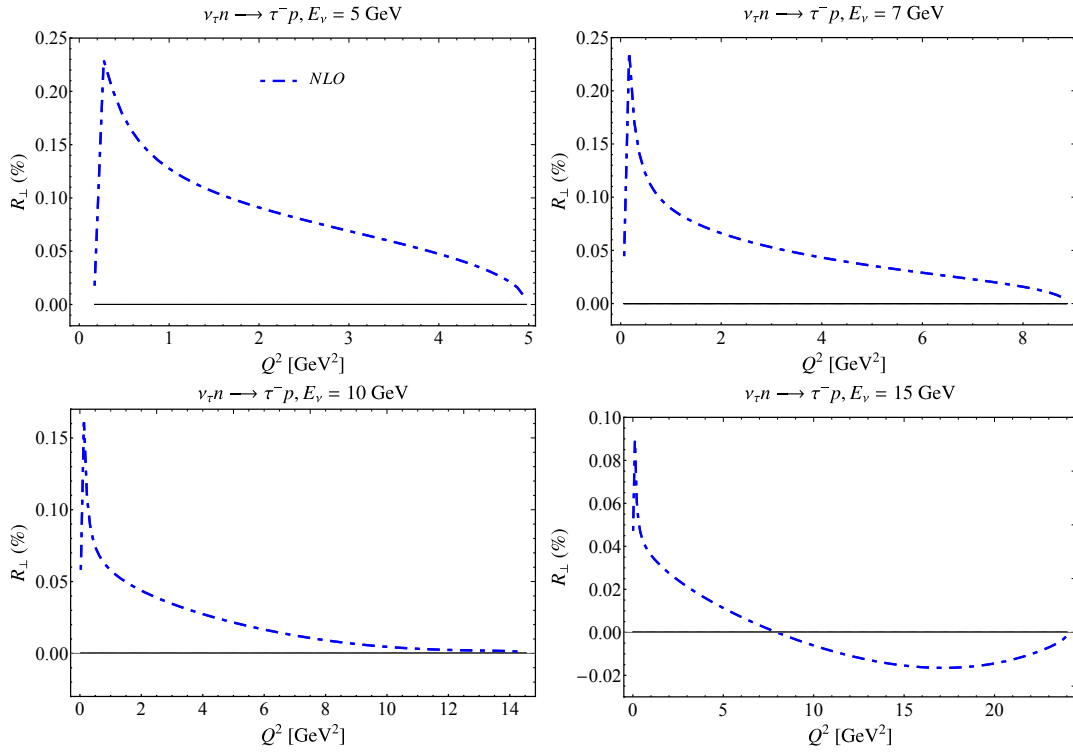


Figure 82: Same as Fig. 72 but for the transverse polarization observable R_\perp .

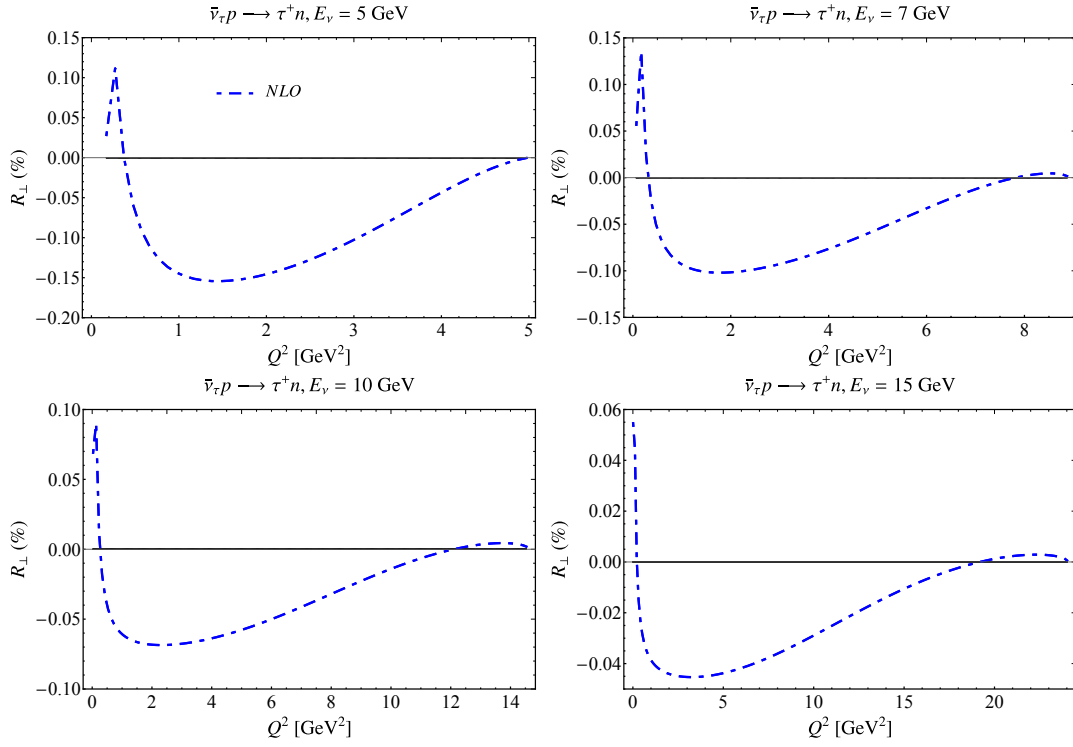


Figure 83: Same as Fig. 73 but for the transverse polarization observable R_{\perp} .

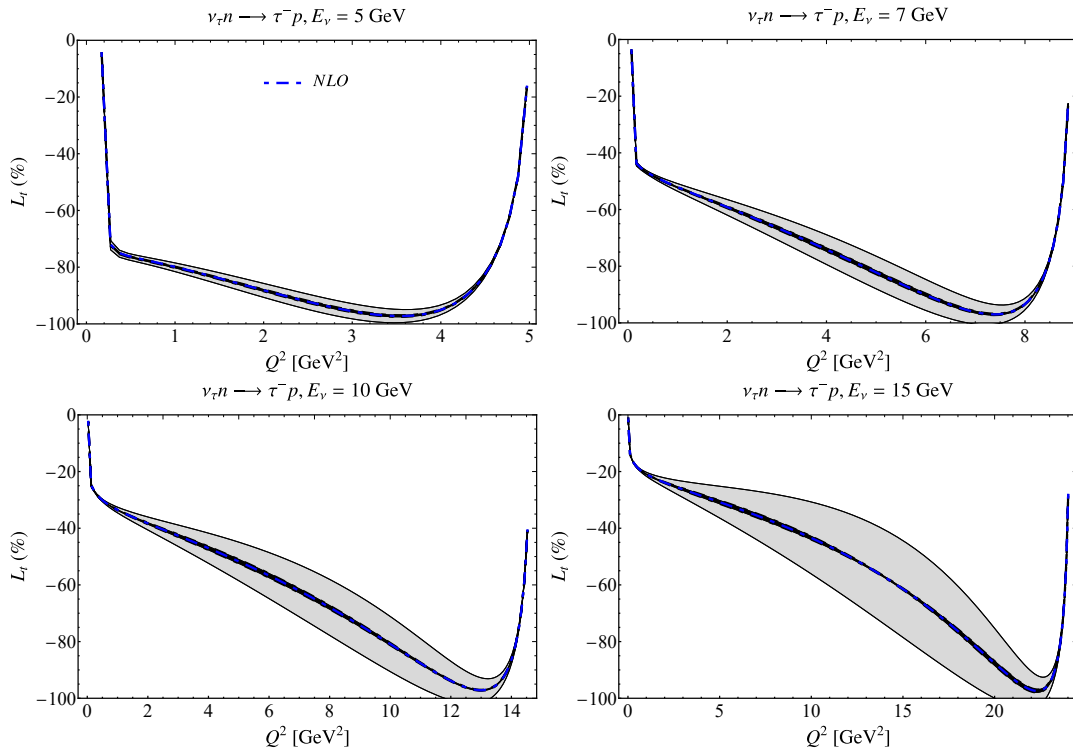


Figure 84: Same as Fig. 72 but for the transverse polarization observable L_t .

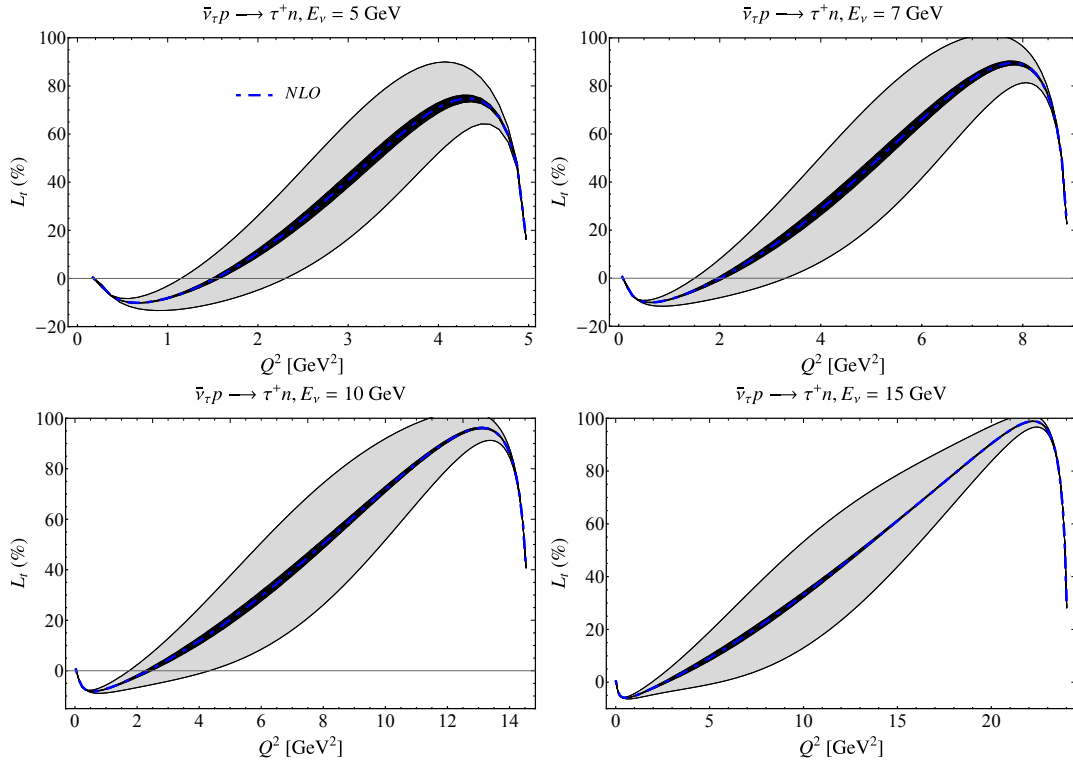


Figure 85: Same as Fig. 73 but for the transverse polarization observable L_t .

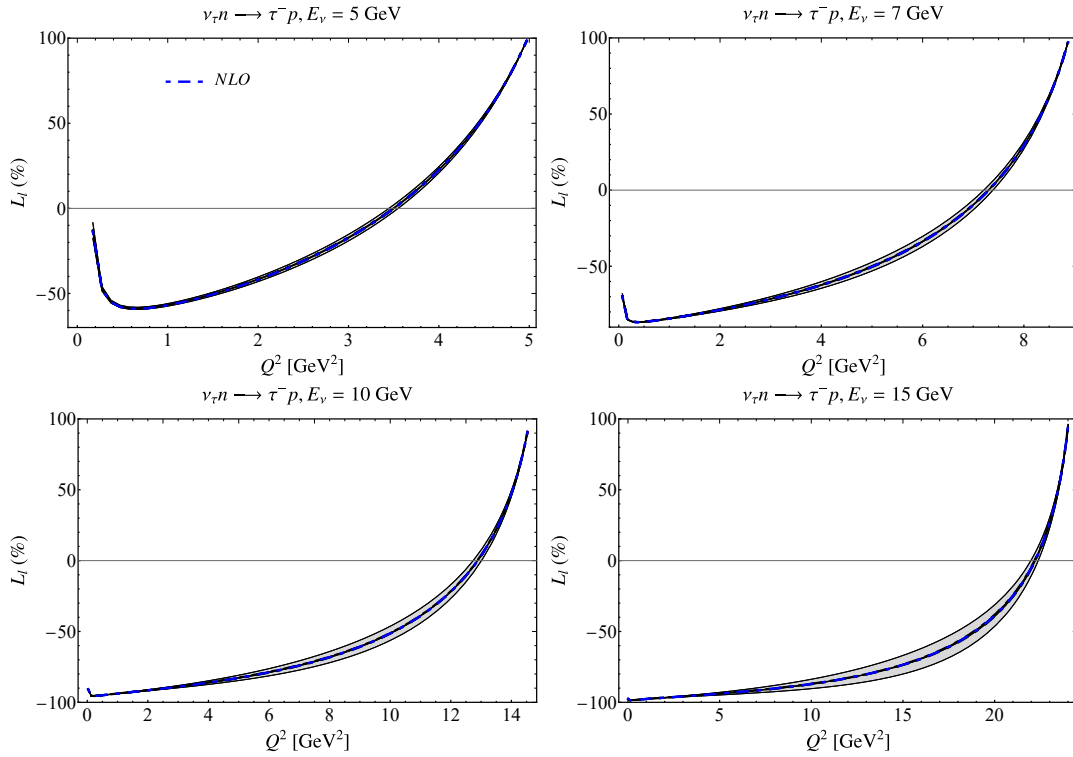


Figure 86: Same as Fig. 72 but for the longitudinal polarization observable L_l .

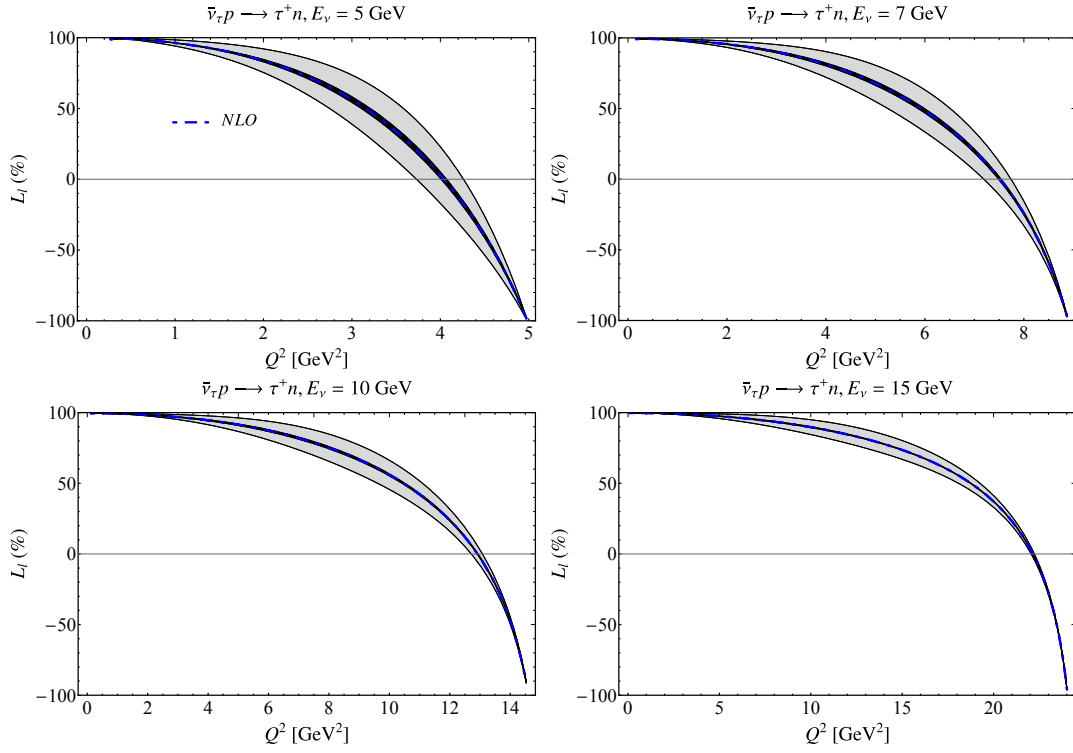


Figure 87: Same as Fig. 73 but for the longitudinal polarization observable L_l .

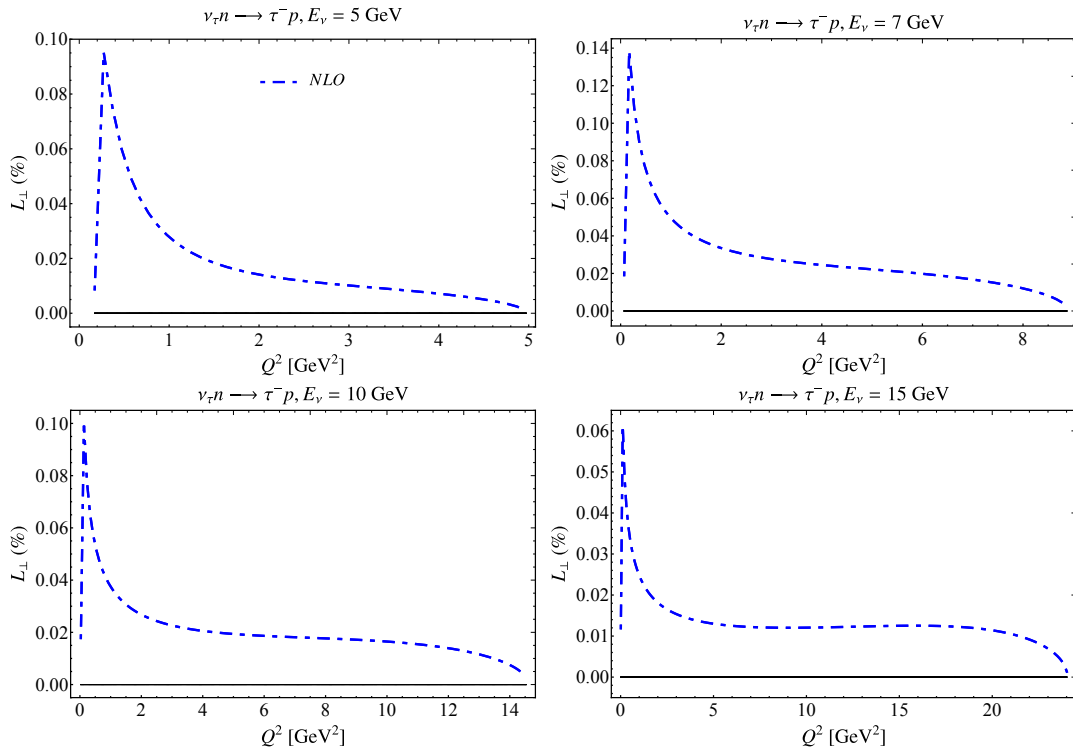


Figure 88: Same as Fig. 72 but for the transverse polarization observable L_{\perp} .

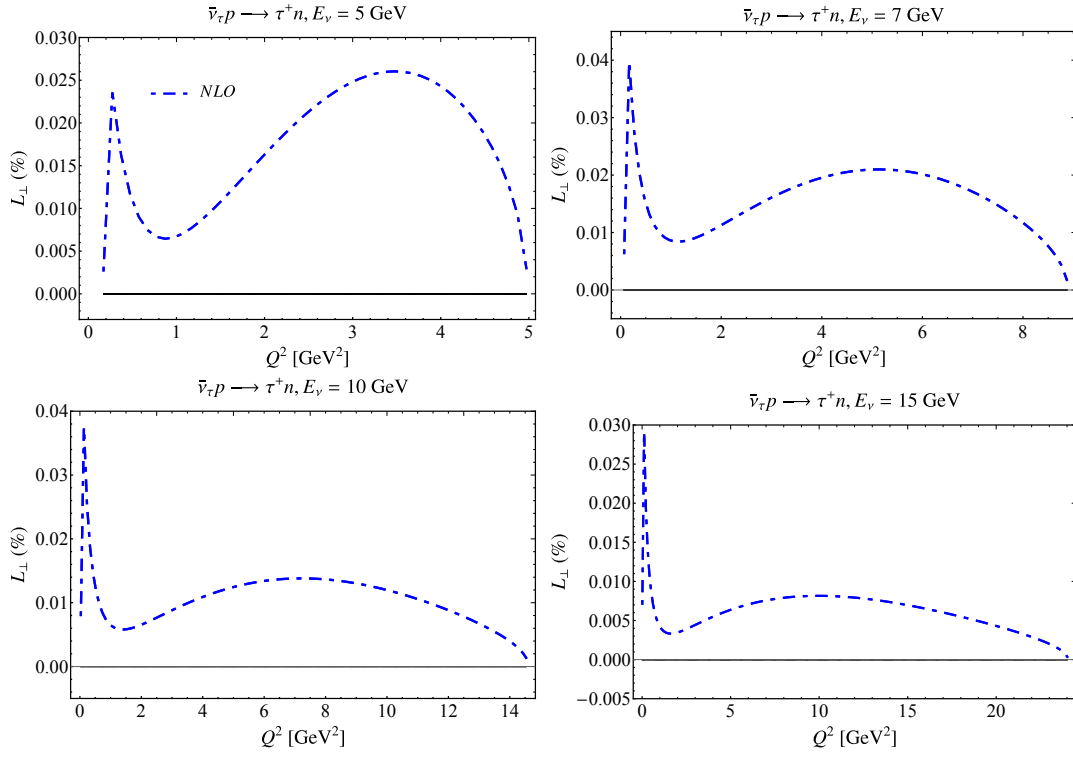


Figure 89: Same as Fig. 73 but for the transverse polarization observable L_{\perp} .

References

- [1] T. Alion et al. (DUNE), (2016), [arXiv:1606.09550 \[physics.ins-det\]](#).
- [2] B. Abi et al. (DUNE), (2020), [arXiv:2002.03005 \[hep-ex\]](#).
- [3] K. Abe et al. (Hyper-Kamiokande), “Hyper-Kamiokande Design Report,” (2016), KEK-PREPRINT-2016-21, ICRR-REPORT-701-2016-1.
- [4] J. A. Formaggio and G. P. Zeller, *Rev. Mod. Phys.* **84**, 1307 (2012), [arXiv:1305.7513 \[hep-ex\]](#).
- [5] U. Mosel, *Ann. Rev. Nucl. Part. Sci.* **66**, 171 (2016), [arXiv:1602.00696 \[nucl-th\]](#).
- [6] L. Alvarez-Ruso et al. (NuSTEC), *Prog. Part. Nucl. Phys.* **100**, 1 (2018), [arXiv:1706.03621 \[hep-ph\]](#).
- [7] J. C. Bernauer et al. (A1), *Phys. Rev. Lett.* **105**, 242001 (2010), [arXiv:1007.5076 \[nucl-ex\]](#).
- [8] J. C. Bernauer et al. (A1), *Phys. Rev. C* **90**, 015206 (2014), [arXiv:1307.6227 \[nucl-ex\]](#).
- [9] W. Xiong et al., *Nature* **575**, 147 (2019).
- [10] V. Punjabi, C. F. Perdrisat, M. K. Jones, E. J. Brash, and C. E. Carlson, *Eur. Phys. J. A* **51**, 79 (2015), [arXiv:1503.01452 \[nucl-ex\]](#).
- [11] D. Ganichot, B. Grossetete, and D. B. Isabelle, *Nucl. Phys. A* **178**, 545 (1972).
- [12] P. E. Bosted et al., *Phys. Rev. C* **42**, 38 (1990).
- [13] T. Cai et al. (MINERvA), *Nature* **614**, 48 (2023).
- [14] M. Gockeler, T. R. Hemmert, R. Horsley, D. Pleiter, P. E. L. Rakow, A. Schafer, and G. Schierholz (QCDSF), *Phys. Rev. D* **71**, 034508 (2005), [arXiv:hep-lat/0303019](#).
- [15] C. Alexandrou, S. Bacchio, M. Constantinou, J. Finkenrath, K. Hadjiyiannakou, K. Jansen, G. Koutsou, and A. Vaquero Aviles-Casco, *Phys. Rev. D* **100**, 014509 (2019), [arXiv:1812.10311 \[hep-lat\]](#).
- [16] T. Yamazaki, Y. Aoki, T. Blum, H.-W. Lin, S. Ohta, S. Sasaki, R. Tweedie, and J. Zanotti, *Phys. Rev. D* **79**, 114505 (2009), [arXiv:0904.2039 \[hep-lat\]](#).
- [17] A. J. Chambers et al. (QCDSF, UKQCD, CSSM), *Phys. Rev. D* **96**, 114509 (2017), [arXiv:1702.01513 \[hep-lat\]](#).
- [18] S. Capitani, M. Della Morte, D. Djukanovic, G. von Hippel, J. Hua, B. Jäger, B. Knippschild, H. B. Meyer, T. D. Rae, and H. Wittig, *Phys. Rev. D* **92**, 054511 (2015), [arXiv:1504.04628 \[hep-lat\]](#).
- [19] M. Bruno et al., *JHEP* **02**, 043 (2015), [arXiv:1411.3982 \[hep-lat\]](#).
- [20] J. D. Bratt et al. (LHPC), *Phys. Rev. D* **82**, 094502 (2010), [arXiv:1001.3620 \[hep-lat\]](#).
- [21] A. S. Kronfeld, D. G. Richards, W. Detmold, R. Gupta, H.-W. Lin, K.-F. Liu, A. S. Meyer, R. Sufian, and S. Syritsyn (USQCD), *Eur. Phys. J. A* **55**, 196 (2019), [arXiv:1904.09931 \[hep-lat\]](#).
- [22] K.-I. Ishikawa, Y. Kuramashi, S. Sasaki, N. Tsukamoto, A. Ukawa, and T. Yamazaki (PACS), *Phys. Rev. D* **98**, 074510 (2018), [arXiv:1807.03974 \[hep-lat\]](#).
- [23] N. Hasan, J. Green, S. Meinel, M. Engelhardt, S. Krieg, J. Negele, A. Pochinsky, and S. Syritsyn, *Phys. Rev. D* **99**, 114505 (2019), [arXiv:1903.06487 \[hep-lat\]](#).
- [24] G. S. Bali, L. Barca, S. Collins, M. Gruber, M. Löffler, A. Schäfer, W. Söldner, P. Wein, S. Weishäupl, and T. Wurm (RQCD), *JHEP* **05**, 126 (2020), [arXiv:1911.13150 \[hep-lat\]](#).
- [25] Y.-C. Jang, R. Gupta, B. Yoon, and T. Bhattacharya, *Phys. Rev. Lett.* **124**, 072002 (2020), [arXiv:1905.06470 \[hep-lat\]](#).
- [26] G. S. Bali, L. Barca, S. Collins, M. Gruber, M. Löffler, A. Schäfer, W. Söldner, P. Wein, S. Weishäupl, and T. Wurm (RQCD), *JHEP* **05**, 126 (2020), [arXiv:1911.13150 \[hep-lat\]](#).

- [27] C. Alexandrou *et al.*, *Phys. Rev. D* **103**, 034509 (2021), arXiv:2011.13342 [hep-lat].
- [28] S. Park, R. Gupta, B. Yoon, S. Mondal, T. Bhattacharya, Y.-C. Jang, B. Joó, and F. Winter (Nucleon Matrix Elements (NME)), *Phys. Rev. D* **105**, 054505 (2022), arXiv:2103.05599 [hep-lat].
- [29] D. Djukanovic, G. von Hippel, J. Koponen, H. B. Meyer, K. Ottnad, T. Schulz, and H. Wittig, *Phys. Rev. D* **106**, 074503 (2022), arXiv:2207.03440 [hep-lat].
- [30] Y.-C. Jang, R. Gupta, T. Bhattacharya, B. Yoon, and H.-W. Lin (Precision Neutron Decay Matrix Elements (PNDME)), *Phys. Rev. D* **109**, 014503 (2024), arXiv:2305.11330 [hep-lat].
- [31] W. A. Mann *et al.*, *Phys. Rev. Lett.* **31**, 844 (1973).
- [32] S. J. Barish *et al.*, *Phys. Rev. D* **16**, 3103 (1977).
- [33] K. L. Miller *et al.*, *Phys. Rev. D* **26**, 537 (1982).
- [34] N. J. Baker, A. M. Cnops, P. L. Connolly, S. A. Kahn, H. G. Kirk, M. J. Murtagh, R. B. Palmer, N. P. Samios, and M. Tanaka, *Phys. Rev. D* **23**, 2499 (1981).
- [35] T. Kitagaki *et al.*, *Phys. Rev. D* **28**, 436 (1983).
- [36] A. S. Meyer, M. Betancourt, R. Gran, and R. J. Hill, *Phys. Rev. D* **93**, 113015 (2016), arXiv:1603.03048 [hep-ph].
- [37] A. S. Meyer, A. Walker-Loud, and C. Wilkinson, *Ann. Rev. Nucl. Part. Sci.* **72**, 205 (2022), arXiv:2201.01839 [hep-lat].
- [38] O. Tomalak, R. Gupta, and T. Bhattacharya, *Phys. Rev. D* **108**, 074514 (2023), arXiv:2307.14920 [hep-lat].
- [39] S. Choi *et al.*, *Phys. Rev. Lett.* **71**, 3927 (1993).
- [40] V. Bernard, U. G. Meissner, and N. Kaiser, *Phys. Rev. Lett.* **72**, 2810 (1994).
- [41] K. I. Blomqvist *et al.*, *Z. Phys. A* **353**, 415 (1996).
- [42] A. Liesenfeld *et al.* (A1), *Phys. Lett. B* **468**, 20 (1999), arXiv:nucl-ex/9911003.
- [43] S. S. Kamalov, G.-Y. Chen, S.-N. Yang, D. Drechsel, and L. Tiator, *Phys. Lett. B* **522**, 27 (2001), arXiv:nucl-th/0107017.
- [44] R. Gran *et al.* (K2K), *Phys. Rev. D* **74**, 052002 (2006), arXiv:hep-ex/0603034.
- [45] I. Frišćić, Measurement of the $p(e, e'\pi^+)n$ reaction with the short-orbit spectrometer at $Q^2 = 0.078$ (GeV/c) 2 , Ph.D. thesis, Zagreb U., Phys. Dept. (2015).
- [46] R. Petti, R. J. Hill, and O. Tomalak, *Phys. Rev. D* **109**, L051301 (2024), arXiv:2309.02509 [hep-ph].
- [47] T. D. Lee and C.-N. Yang, *Phys. Rev.* **126**, 2239 (1962).
- [48] V. Florescu and P. Minnaert, *Phys. Rev.* **168**, 1662 (1968).
- [49] N. Dombey, *Rev. Mod. Phys.* **41**, 236 (1969).
- [50] A. Pais, *Annals Phys.* **63**, 361 (1971).
- [51] T. P. Cheng and W.-K. Tung, *Phys. Rev. D* **3**, 733 (1971), [Erratum: *Phys. Rev. D* **3**, 2923–2923 (1971)].
- [52] R. Tarrach, *Nucl. Phys. B* **70**, 70 (1974).
- [53] L. Oliver and T. N. Pham, *Phys. Rev. D* **10**, 993 (1974).
- [54] A. I. Akhiezer and M. P. Rekalov, *Fiz. Elem. Chast. Atom. Yadra* **4**, 662 (1973).
- [55] J. E. Kim, P. Langacker, and S. Sarkar, *Phys. Rev. D* **18**, 123 (1978).
- [56] F. L. Ridener and R. H. Good, *Phys. Rev. D* **28**, 2875 (1983).

- [57] F. L. Ridener, H. S. Song, and R. H. Good, *Phys. Rev. D* **32**, 2921 (1985).
- [58] K. Hagiwara, K. Mawatari, and H. Yokoya, *Nucl. Phys. B* **668**, 364 (2003), [Erratum: *Nucl.Phys.B* 701, 405–406 (2004)], [arXiv:hep-ph/0305324](#).
- [59] K. Hagiwara, K. Mawatari, and H. Yokoya, *Nucl. Phys. B Proc. Suppl.* **139**, 140 (2005), [arXiv:hep-ph/0408212](#).
- [60] K. M. Graczyk, *Nucl. Phys. B Proc. Suppl.* **139**, 150 (2005), [arXiv:hep-ph/0407283](#).
- [61] K. M. Graczyk, *Nucl. Phys. A* **748**, 313 (2005), [arXiv:hep-ph/0407275](#).
- [62] C. Bourrely, J. Soffer, and O. V. Teryaev, *Phys. Rev. D* **69**, 114019 (2004), [arXiv:hep-ph/0403176](#).
- [63] K. S. Kuzmin, V. V. Lyubushkin, and V. A. Naumov, *Mod. Phys. Lett. A* **19**, 2919 (2004), [arXiv:hep-ph/0403110](#).
- [64] K. S. Kuzmin, V. V. Lyubushkin, and V. A. Naumov, *Nucl. Phys. B Proc. Suppl.* **139**, 154 (2005), [arXiv:hep-ph/0408107](#).
- [65] N. Jachowicz, K. Vantournhout, J. Ryckebusch, and K. Heyde, *Phys. Rev. Lett.* **93**, 082501 (2004), [arXiv:nucl-th/0406078](#).
- [66] N. Jachowicz, K. Vantournhout, J. Ryckebusch, and K. Heyde, *Phys. Rev. C* **71**, 034604 (2005), [arXiv:nucl-th/0502061](#).
- [67] M. Aoki, K. Hagiwara, K. Mawatari, and H. Yokoya, *Nucl. Phys. B* **727**, 163 (2005), [arXiv:hep-ph/0503050](#).
- [68] M. Aoki, K. Hagiwara, K. Mawatari, and H. Yokoya, *Nucl. Phys. B Proc. Suppl.* **144**, 297 (2005).
- [69] P. Lava, N. Jachowicz, M. C. Martinez, and J. Ryckebusch, *Phys. Rev. C* **73**, 064605 (2006), [arXiv:nucl-th/0509103](#).
- [70] A. Meucci, C. Giusti, and F. D. Pacati, *Phys. Rev. C* **77**, 034606 (2008).
- [71] S. M. Bilenky and E. Christova, *J. Phys. G* **40**, 075004 (2013), [arXiv:1303.3710 \[hep-ph\]](#).
- [72] S. M. Bilenky and E. Christova, *Phys. Part. Nucl. Lett.* **10**, 651 (2013), [arXiv:1307.7275 \[hep-ph\]](#).
- [73] A. Fatima, M. Sajjad Athar, and S. K. Singh, *Phys. Rev. D* **98**, 033005 (2018), [arXiv:1806.08597 \[hep-ph\]](#).
- [74] A. Fatima, M. Sajjad Athar, and S. K. Singh, *Eur. Phys. J. A* **54**, 95 (2018), [arXiv:1802.04469 \[hep-ph\]](#).
- [75] A. Fatima, M. S. Athar, and S. K. Singh, *Front. in Phys.* **7**, 13 (2019), [arXiv:1807.08314 \[hep-ph\]](#).
- [76] J. E. Sobczyk, N. Rocco, and J. Nieves, *Phys. Rev. C* **100**, 035501 (2019), [arXiv:1906.05656 \[nucl-th\]](#).
- [77] K. M. Graczyk and B. E. Kowal, *Phys. Rev. D* **101**, 073002 (2020), [arXiv:1912.00064 \[hep-ph\]](#).
- [78] K. M. Graczyk and B. E. Kowal, *Acta Phys. Polon. B* **50**, 1771 (2019).
- [79] O. Tomalak, *Phys. Rev. D* **103**, 013006 (2021), [arXiv:2008.03527 \[hep-ph\]](#).
- [80] A. Fatima, M. Sajjad Athar, and S. K. Singh, *Phys. Rev. D* **102**, 113009 (2020), [arXiv:2010.10311 \[hep-ph\]](#).
- [81] A. Fatima, M. S. Athar, and S. K. Singh, *Eur. Phys. J. ST* **230**, 4391 (2021), [arXiv:2106.14590 \[hep-ph\]](#).
- [82] M. Sajjad Athar, A. Fatima, and S. K. Singh, *Prog. Part. Nucl. Phys.* **129**, 104019 (2023), [arXiv:2206.13792 \[hep-ph\]](#).
- [83] L. Alvarez-Ruso *et al.*, (2022), [arXiv:2203.11298 \[hep-ex\]](#).
- [84] C. Llewellyn Smith, *Phys. Rept.* **3**, 261 (1972).
- [85] V. Bernard, H. W. Fearing, T. R. Hemmert, and U. G. Meissner, *Nucl. Phys. A* **635**, 121 (1998), [Erratum: *Nucl.Phys.A* 642, 563–563 (1998)], [arXiv:hep-ph/9801297](#).

- [86] T. Fuchs, Formfaktoren des Nukleons in relativistischer chiraler Störungstheorie, Other thesis (2002).
- [87] N. Kaiser, *Phys. Rev. C* **67**, 027002 (2003), [arXiv:nucl-th/0301034](#).
- [88] M. R. Schindler, T. Fuchs, J. Gegelia, and S. Scherer, *Phys. Rev. C* **75**, 025202 (2007), [arXiv:nucl-th/0611083](#).
- [89] M. F. M. Lutz, U. Sauerwein, and R. G. E. Timmermans, *Eur. Phys. J. C* **80**, 844 (2020), [arXiv:2003.10158 \[hep-lat\]](#).
- [90] C. Chen, C. S. Fischer, C. D. Roberts, and J. Segovia, *Phys. Lett. B* **815**, 136150 (2021), [arXiv:2011.14026 \[hep-ph\]](#).
- [91] Y.-C. Jang, T. Bhattacharya, R. Gupta, B. Yoon, and H.-W. Lin (PNDME), *PoS LATTICE2016*, 178 (2016).
- [92] R. Gupta, Y.-C. Jang, H.-W. Lin, B. Yoon, and T. Bhattacharya, *Phys. Rev. D* **96**, 114503 (2017), [arXiv:1705.06834 \[hep-lat\]](#).
- [93] D. H. Wright et al., *Phys. Rev. C* **57**, 373 (1998).
- [94] P. Winter, *AIP Conf. Proc.* **1441**, 537 (2012), [arXiv:1110.5090 \[nucl-ex\]](#).
- [95] V. A. Andreev et al. (MuCap), *Phys. Rev. C* **91**, 055502 (2015), [arXiv:1502.00913 \[nucl-ex\]](#).
- [96] V. A. Andreev et al. (MuCap), *Phys. Rev. Lett.* **110**, 012504 (2013), [arXiv:1210.6545 \[nucl-ex\]](#).
- [97] T. Gorringer and H. W. Fearing, *Rev. Mod. Phys.* **76**, 31 (2004), [arXiv:nucl-th/0206039](#).
- [98] R. J. Hill, P. Kammel, W. J. Marciano, and A. Sirlin, *Rept. Prog. Phys.* **81**, 096301 (2018), [arXiv:1708.08462 \[hep-ph\]](#).
- [99] M. González-Alonso, O. Naviliat-Cuncic, and N. Severijns, *Prog. Part. Nucl. Phys.* **104**, 165 (2019), [arXiv:1803.08732 \[hep-ph\]](#).
- [100] O. Tomalak, Q. Chen, R. J. Hill, and K. S. McFarland, *Nature Commun.* **13**, 5286 (2022), [arXiv:2105.07939 \[hep-ph\]](#).
- [101] O. Tomalak, Q. Chen, R. J. Hill, K. S. McFarland, and C. Wret, *Phys. Rev. D* **106**, 093006 (2022), [arXiv:2204.11379 \[hep-ph\]](#).
- [102] M. J. Ramsey-Musolf and S. Su, *Phys. Rept.* **456**, 1 (2008), [arXiv:hep-ph/0612057](#).
- [103] J. C. Hardy and I. S. Towner, *Phys. Rev. C* **79**, 055502 (2009), [arXiv:0812.1202 \[nucl-ex\]](#).
- [104] N. Yamanaka, T. Sato, and T. Kubota, *J. Phys. G* **37**, 055104 (2010), [arXiv:0908.1007 \[hep-ph\]](#).
- [105] A. Kozela et al., *Phys. Rev. C* **85**, 045501 (2012), [arXiv:1111.4695 \[nucl-ex\]](#).
- [106] K. S. Kuzmin, V. V. Lyubushkin, and V. A. Naumov, *Eur. Phys. J. C* **54**, 517 (2008), [arXiv:0712.4384 \[hep-ph\]](#).
- [107] F. Akbar, M. Rafi Alam, M. Sajjad Athar, S. Chauhan, S. K. Singh, and F. Zaidi, *Int. J. Mod. Phys. E* **24**, 1550079 (2015), [arXiv:1506.02355 \[nucl-th\]](#).
- [108] S. Weinberg, *Phys. Rev.* **112**, 1375 (1958).
- [109] M. Day and K. S. McFarland, *Phys. Rev. D* **86**, 053003 (2012), [arXiv:1206.6745 \[hep-ph\]](#).
- [110] V. Cirigliano, B. Grinstein, G. Isidori, and M. B. Wise, *Nucl. Phys. B* **728**, 121 (2005), [arXiv:hep-ph/0507001](#).
- [111] O. Tomalak, M. Betancourt, K. Borah, R. J. Hill, and T. Junk, (2024), [arXiv:2402.14115 \[hep-ph\]](#).
- [112] K. Borah, R. J. Hill, G. Lee, and O. Tomalak, *Phys. Rev. D* **102**, 074012 (2020), [arXiv:2003.13640 \[hep-ph\]](#).
- [113] J. C. Hardy and I. S. Towner, *Phys. Rev. C* **102**, 045501 (2020).
- [114] B. R. Holstein, *Phys. Rev. C* **29**, 623 (1984).

- [115] L. Ahrens, S. H. Aronson, et al., *Physics Letters B* **202**, 284 (1988).
- [116] S. L. Adler, E. W. Colglazier, Jr., J. B. Healy, I. Karliner, J. Lieberman, Y. J. Ng, and H.-S. Tsao, *Phys. Rev. D* **11**, 3309 (1975).
- [117] E. H. Monsay, *Phys. Rev. D* **16**, 609 (1977).
- [118] Y. Masuda, T. Minamisono, Y. Nojiri, and K. Sugimoto, *Phys. Rev. Lett.* **43**, 1083 (1979).
- [119] M. Oka and K. Kubodera, *Phys. Lett. B* **90**, 45 (1980).
- [120] C. A. Dominguez, *Phys. Rev. D* **20**, 802 (1979).
- [121] G. Bardin, J. Duclos, A. Magnon, J. Martino, A. Richter, E. Zavattini, A. Bertin, M. Piccinini, and A. Vitale, *Phys. Lett. B* **104**, 320 (1981).
- [122] L. Grenacs, *Ann. Rev. Nucl. Part. Sci.* **35**, 455 (1985).
- [123] H. Shiomi, *Nucl. Phys. A* **603**, 281 (1996), [arXiv:hep-ph/9601329](#).
- [124] J. Govaerts and J.-L. Lucio-Martinez, *Nucl. Phys. A* **678**, 110 (2000), [arXiv:nucl-th/0004056](#).
- [125] D. H. Wilkinson, *Eur. Phys. J. A* **7**, 307 (2000).
- [126] K. Minamisono et al., *Phys. Rev. C* **65**, 015501 (2002).
- [127] J. C. Hardy and I. S. Towner, *Phys. Rev. C* **71**, 055501 (2005), [arXiv:nucl-th/0412056](#).
- [128] N. Severijns, M. Beck, and O. Naviliat-Cuncic, *Rev. Mod. Phys.* **78**, 991 (2006), [arXiv:nucl-ex/0605029](#).
- [129] T. Sumikama et al., *Phys. Lett. B* **664**, 235 (2008).
- [130] K. Minamisono et al., *Phys. Rev. C* **84**, 055501 (2011).
- [131] J. C. Hardy and I. S. Towner, *Phys. Rev. C* **91**, 025501 (2015), [arXiv:1411.5987 \[nucl-ex\]](#).
- [132] B. R. Holstein, *J. Phys. G* **41**, 114001 (2014).
- [133] A. Falkowski, M. González-Alonso, and O. Naviliat-Cuncic, *JHEP* **04**, 126 (2021), [arXiv:2010.13797 \[hep-ph\]](#).
- [134] A. Falkowski, M. González-Alonso, A. Palavrić, and A. Rodríguez-Sánchez, *JHEP* **02**, 091 (2024), [arXiv:2112.07688 \[hep-ph\]](#).
- [135] T. D. Lee and C.-N. Yang, *Phys. Rev.* **104**, 254 (1956).
- [136] J. D. Jackson, S. B. Treiman, and H. W. Wyld, *Phys. Rev.* **106**, 517 (1957).
- [137] V. Cirigliano, J. Jenkins, and M. González-Alonso, *Nucl. Phys. B* **830**, 95 (2010), [arXiv:0908.1754 \[hep-ph\]](#).
- [138] T. Bhattacharya, V. Cirigliano, S. D. Cohen, A. Filipuzzi, M. González-Alonso, M. L. Graesser, R. Gupta, and H.-W. Lin, *Phys. Rev. D* **85**, 054512 (2012), [arXiv:1110.6448 \[hep-ph\]](#).
- [139] V. Cirigliano, M. González-Alonso, and M. L. Graesser, *JHEP* **02**, 046 (2013), [arXiv:1210.4553 \[hep-ph\]](#).
- [140] O. Naviliat-Cuncic and M. González-Alonso, *Annalen Phys.* **525**, 600 (2013), [arXiv:1304.1759 \[hep-ph\]](#).
- [141] M. González-Alonso and J. Martin Camalich, *JHEP* **12**, 052 (2016), [arXiv:1605.07114 \[hep-ph\]](#).
- [142] A. Falkowski, M. González-Alonso, and K. Mimouni, *JHEP* **08**, 123 (2017), [arXiv:1706.03783 \[hep-ph\]](#).
- [143] S. Alioli, W. Dekens, M. Girard, and E. Mereghetti, *JHEP* **08**, 205 (2018), [arXiv:1804.07407 \[hep-ph\]](#).
- [144] A. Falkowski, M. González-Alonso, and Z. Tabrizi, *JHEP* **05**, 173 (2019), [arXiv:1901.04553 \[hep-ph\]](#).
- [145] A. Falkowski, M. González-Alonso, J. Kopp, Y. Soreq, and Z. Tabrizi, *JHEP* **10**, 086 (2021), [arXiv:2105.12136 \[hep-ph\]](#).
- [146] V. Cirigliano, W. Dekens, J. de Vries, E. Mereghetti, and T. Tong, (2023), [arXiv:2311.00021 \[hep-ph\]](#).

- [147] M. Dawid, V. Cirigliano, and W. Dekens, (2024), [arXiv:2402.06723 \[hep-ph\]](#).
- [148] K. Kodama et al. (DONuT), *Phys. Rev. D* **78**, 052002 (2008), [arXiv:0711.0728 \[hep-ex\]](#).
- [149] N. Agafonova et al. (OPERA), *Phys. Rev. Lett.* **115**, 121802 (2015), [arXiv:1507.01417 \[hep-ex\]](#).
- [150] M. G. Aartsen et al. (IceCube), *Phys. Rev. D* **99**, 032007 (2019), [arXiv:1901.05366 \[hep-ex\]](#).
- [151] S. Aoki et al. (DsTau), *JHEP* **01**, 033 (2020), [arXiv:1906.03487 \[hep-ex\]](#).
- [152] R. Mertig, M. Bohm, and A. Denner, *Comput. Phys. Commun.* **64**, 345 (1991).
- [153] V. Shtabovenko, R. Mertig, and F. Orellana, *Comput. Phys. Commun.* **207**, 432 (2016).
- [154] T. Hahn and M. Perez-Victoria, *Comput. Phys. Commun.* **118**, 153 (1999).
- [155] Wolfram Research, Inc., “Mathematica, Version 12.2.0.0,” (2022), Champaign, IL.